GKSS
FORSCHUNGSZENTRUM
in der HELMHOLTZ-GEMEINSCHAFT

The Role of Northern Hemispheric Cryospheric Albedo Changes: A Model Study of the Arctic's Impact on the Global Climate

(Vom Department Geowissenschaften der Universität Hamburg als Dissertation angenommene Arbeit)

Author:

A. Benkel

ISSN 0344-9629

HELMHOLTZ
| GEMEINSCHAFT

wissen
schafft
nutzen

GKSS 2007/13

GKSS 2007/13

The Role of Northern Hemispheric Cryospheric Albedo Changes: A Model Study of the Arctic's Impact on the Global Climate

(Vom Department Geowissenschaften der Universität Hamburg als Dissertation angenommene Arbeit)

Author:

A. Benkel

(Institute for Coastal Research)

GKSS-Forschungszentrum Geesthacht GmbH • Geesthacht • 2007

Die Berichte der GKSS werden kostenlos abgegeben.
The delivery of the GKSS reports is free of charge.

Anforderungen/Requests:

GKSS-Forschungszentrum Geesthacht GmbH
Bibliothek/Library
Postfach 11 60
D-21494 Geesthacht
Germany

Fax.: (49) 04152/871717

Als Manuskript vervielfältigt.

ISSN 0344-9629

GKSS-Forschungszentrum Geesthacht GmbH · Telefon (04152)87-0
Max-Planck-Straße 1 · D-21502 Geesthacht / Postfach 11 60 · D-21494 Geesthacht

GKSS 2007/13

The Role of Northern Hemispheric Cryospheric Albedo Changes: A Model Study of the Arctic's Impact on the Global Climate

(Vom Department Geowissenschaften der Universität Hamburg als Dissertation angenommene Arbeit)

Andreas Benkel

107 pages with 56 figures and 7 tables

Abstract

In this study, simulations were performed with the coupled global climate model ECHO-G in order to investigate the influence of different cryospheric albedo conditions in the Northern Hemisphere (NH) on the Arctic climate. In particular, this study is concerned with influences of different surface-temperature-depending albedo parameterisations on the Arctic sea ice and the impact of a changed Arctic climate on the global scale atmospheric circulation.

The changed description of the NH cryophere's albedo enhanced the radiative energy deficit in the Arctic. In particular, it led to an increased sea ice thickness over the Arctic Ocean, increased NH snow cover, a decreased seasonal cycle of NH sea ice cover, and a decrease in Arctic, NH, and global near surface air temperature. The generally increased surface and planetary albedo of the NH was accompanied by a warmer Arctic stratosphere, especially in March and April. This led to a decreased strength of the polar vortex and a consistent shift of the Arctic Oscillation towards its negative polarity. During these months atmospheric circulation changes were maximum in both hemispheres, including zonally averaged zonal wind speed changes in a pattern that was symmetric to the equator.

In future scenario simulations the changed mean state sea ice cover did not affect the retreat rate of the NH sea ice cover. Moreover, the choice of a more sophisticated albedo scheme for the cryosphere did not affect the strength of the polar amplification of global warming as the regional climate sensitivity of the model was not changed.

Die Bedeutung von Albedoänderungen der Kryosphäre auf der Nordhalbkugel: Eine Modellstudie zum Einfluss der Arktis auf das globale Klima

Zusammenfassung

In der vorliegenden Arbeit wurden mit Hilfe des gekoppelten Klimamodells ECHO-G die Auswirkungen einer geänderten Oberflächenalbedo der Kryosphäre auf der Nordhalbkugel auf das Klima der Arktis untersucht. Das Hauptaugenmerk lag hierbei auf dem Verhalten der nordhemisphärischen

Meereisbedeckung und dem Einfluss veränderter Klimabedingungen in der Arktis auf die großräumige atmosphärische Zirkulation auf der gesamten Erde.

Als Folge einer veränderten Beschreibung der Albedo der nordhemisphärischen Kryosphäre wurde das bereits bestehende Strahlungsenergiebilanzdefizit der Arktis weiter vergrößert. Dies führte in der Folge insbesondere zu einer Zunahme der Meereisdicke über dem Arktischen Ozean und einer Zunahme der Schneebedeckung der Nordhemisphäre. Ferner kam es zu einer Abnahme des Jahresganges der nordhemisphärischen Meereisbedeckung sowie zu einem Rückgang der bodennahen Lufttemperatur in der Arktis, über der Nordhalbkugel und auch im globalen Mittel. Überwiegend war die Bodenalbedo und damit auch die planetare Albedo vergrößert. Damit einher ging – besonders im März und April – eine wärmere Stratosphäre in der Arktis, was zu einer Abschwächung des stratosphärischen Polarwirbels und damit auch zu einer Verschiebung der Phase der Arktischen Oszillation in Richtung negativer Polarität führte. In den Monaten März und April traten die atmosphärischen Zirkulationsänderungen sowohl auf der Süd- als auch auf der Nordhalbkugel am kräftigsten hervor, wobei die Änderungen in der meridional gemittelten Zonalwindgeschwindigkeit in einem Muster auftraten, welches auffallend symmetrisch zum Äquator ausfiel.

In Simulationen von Zukunftsszenarien stellte sich heraus, dass ein veränderter mittlerer Zustand der Meereisbedeckung keinen Einfluss auf die Rate hat, mit welcher sich die vom Meereis bedeckte Fläche der Nordhalbkugel verringert. Darüber hinaus zeigte sich kein Einfluss des anspruchsvolleren Albedoschemas auf das Maß der sich zu den Polen hin verstärkenden Erwärmung der Erde, weil auch die regionale Klimasensitivität des Modells unverändert geblieben war.

Manuscript received / Manuskripteingang in TKP: 21. Juni 2007

Contents

Chapter 1

Introduction

Large areas of the Northern Hemisphere (hereafter: NH) are at least seasonally covered with snow and ice. In low altitudes snow and ice occur as a result of less solar insolation towards the earth's poles – especially in winter – leading to low surface temperatures. Snow, glaciers and sea ice have a much higher albedo than other surfaces on land or than the ocean water. Accordingly, the cryosphere plays an important role within the global climate system, as over areas covered with snow and ice less solar radiation is absorbed compared to areas not covered with snow and ice.

The Arctic consists of the land and ocean areas around the North Pole and is more influenced by the cryosphere than other regions of the NH. A more detailed definition is given in the following chapter 2.1. For astronomical reasons the insolation during NH winter (hereafter: boreal winter) is very low for the Arctic. As a consequence the Arctic's annual mean insolation is also much lower than for lower latitudes. The high-reflective surface conditions of the Arctic (also in summer due to glaciers and multi-year sea ice) lead to the absorption of only a small fraction of the few incoming solar radiation. Thus the Arctic acts as a sink of energy in the global climate system.

Owing to the Arctic's remoteness, few and only short instrumental records of its meteorological parameters are available. Over the Arctic Ocean the situation is even worse. Here only data from field experiment campaigns, Soviet ice drift stations, submarine cruises and satellite observations exist. These data are either too sparse to represent large parts of the Arctic Ocean or do not cover longer periods (e.g. satellite data).

Modelling with atmosphere-ocean general circulation models (hereafter AOGCM) gives an insight into Arctic processes by providing physically consistent fields of all relevant meteorological parameters and also accounting for interaction between the Arctic climate and the climate system outside the Arctic. As only AOGCMs can provide this insight on a time scale covering centuries it is obvious that it is one aim in quasi-realistic modelling to simulate the relevant processes and quantities as accurately as possible.

Due to various feedback loops and especially the positive surface albedo temperature feedback mechanism over sea ice and snow covered areas, a most accurate description of processes involved in this feedback becomes a crucial factor in climate modelling.

Climate change under increasing greenhouse gas (GHG) concentrations is expected to have greatest effects in the Arctic (e.g. ACIA 2005). The Third Assessment Report (TAR) of the Intergovernmental Panel on Climate Change (IPCC) projected a model mean increase of the global annual near surface temperature (T_{2m}) by 3.5 K (A2) and 2.5 K (B2) for the end of the 21st century (IPCC 2001). A2 and B2 are identifiers of greenhouse gas (GHG) emission scenarios stemming from the Special Report on Emissions Scenarios (SRES) (IPCC 2000). The increase for the region north of 60° N is twice the global increase with up to 9 K in the moderate B2 scenario over the central Arctic Ocean in autumn. This is also accompanied by a substantial decrease in snow and sea ice cover (ACIA 2005). The decrease in Arctic sea ice cover also includes abrupt reductions, reaching near ice-free conditions in September by 2040 (Holland et al. 2006).

Arctic climate feedbacks and processes are insufficiently understood (ACIA 2005) leading to differences between scenario runs that are largest in the Arctic (Figure 1.1). In order to examine the meridional dependancy of maximum changes in T_{2m}, the zonally averaged T_{2m} change is divided (i.e. normalised) by the respective global average T_{2m} change. Therefore the polar amplification of global warming is comparable between different models, regardless the sensitivity of a specific model to – for example – increasing GHG concentrations. Bony et al. (2006) demonstrated that current AOGCMs generally show a polar amplification of global warming (especially in the NH) but also differ in their particular amount of polar amplification (Figure 1.1). Polar amplification of global warming is caused to a large extent by the surface albedo temperature feedback in the Arctic. Higher temperatures lead to less snow and ice, causing more absorbed solar radiation which increases the temperature.

Besides the predicted changes in the Arctic in the climate scenario simulations several studies describe actual changes using observational data. Serreze et al. (2000) summarised some observational trends e.g. the decrease of NH snow cover by 10 % from 1972 to 2000 which is a rare event in a 1000-year climate model simulation (Vinnikov and Robock 1998). Recent observations document a thinning of Arctic sea ice (Rothrock et al. 1999) and a rapidly decreasing Arctic sea ice extent, especially in late summer (e.g. Cavalieri et al. 2003, Vinje 2001a, Stroeve et al. 2005, Vinnikov et al. 2002). Thinning and retreat of sea ice decrease the local albedo and additionally enlarge the heat release (latent and sensible) from the ocean to the atmosphere.

Under climate warming conditions an increase in the positive precipitation minus evaporation (P-E) balance over the Arctic is expected (e.g. ACIA 2005, IPCC 2001) leading to a freshening of the Arctic Ocean and thus a reduction of the Thermohaline

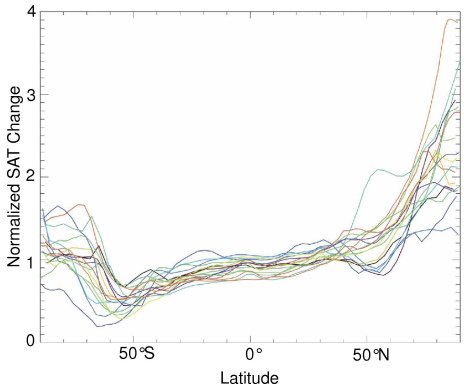

Figure 1.1: Normalised zonally averaged surface air temperature (SAT) changes from 17 models participating in the forth assessment report (AR4) of the IPCC (from Bony et al. 2006). The temperature change is computed as the 2080–2099 average from the so-called SRES A1B scenario minus the 1980–1999 average from climate of the 20^{th} century simulations. The zonally averaged change is normalised by the global average SAT changes.

Circulation (THC) in the North Atlantic up to a theoretically possible shut-down of the THC (e.g. Rahmstorf et al. 2005, Manabe and Stouffer 1994). The shut-down of the THC is discussed in the literature as a low probability – high impact risk (e.g. IPCC 2001). The P-E balance over the polar cap oceans contributes approx. 1/3, the river runoff the remaining 2/3 of the freshwater input into the polar cap oceans. Wu et al. (2005) attributed the observed increase of Arctic river discharge (Peterson et al. 2002) to human influence. Rennermalm et al. (2006) demonstrated that changes in Arctic river runoff can be translated very effective into the THC strength. Bryden et al. (2005) published an observed decrease of the Atlantic meridional overturning circulation (AMOC) since 1957. Results of the Bryden et al. (2005) study are, however, only based upon 5 measurement campaigns, which means, that a trend can hardly be distinguished from fluctuations.

Numerical experiments also underline the effect of the sea ice extent in the North Atlantic on the stability of the meridional overturning circulation (MOC) (Saenko et al. 2004). The summer sea ice extent is closely connected to the sea ice thickness. Performing sensitivity experiments with a sea ice model, Lemke et al. (2000) found a sea ice thickness and export change of about 2 % if the net radiative forcing increased by 1 $\mathrm{W\,m^{-2}}$. The response function remained linear for the range of ± 10 $\mathrm{W\,m^{-2}}$ and still smooth for the range of ± 80 $\mathrm{W\,m^{-2}}$. Due to the land-encircled Arctic Ocean the sensitivity of the ice extent was much smaller (0.3 % per 1 $\mathrm{W\,m^{-2}}$). Tuenter et al. (2005) also stressed from findings in orbitally induced sea ice feedbacks that the boreal summer insolation plays the dominating role for the summer as well as for the winter sea ice extent.

Knutti et al. (2006) found that AOGCMs with high climate sensitivity overestimate the seasonal cycle in regional temperature compared to observations. Hall and Qu (2006) showed that the surface albedo feedback (SAF) strength in the seasonal cycle is closely correlated to that in climate change and argued that an improvement in simulating the

seasonal cycle would decrease the models' spread in climate change scenarios. They predicted that a sea ice albedo feedback constrained to the current seasonal cycle would also decrease the spread in those simulations. Additionally Qu and Hall (2006) stated from simulation and ISCCP (International Satellite Cloud Climatology Project) results that surface albedo anomalies are transformed into planetary albedo anomalies without being much influenced by clouds. A changed snow and sea ice albedo should lead to a changed planetary albedo with the same sign of change as the cryospheric albedo change. Snow albedo has a high impact on large scale climate phenomena. Hansen and Nazarenko (2004) pointed out that soot on snow and sea ice is an unusually effective forcing in global warming. Therefore Hansen et al. (2005) suggested that Black Carbon (BC) snow albedo contribute substantially to rapid warming and sea ice loss in the Arctic. Krinner et al. (2006) demonstrated that surface albedo reduction by mineral dust deposition on seasonal snow cover prevented Asia from being covered with large ice sheets during the Last Glacial Maximum (21 kyr BP).

Testing the Milankovitch hypothesis of climate changes as a local thermodynamic response to insolation changes Hall et al. (2005) found that these insolation changes do not only change temperatures as a local thermodynamic response. Instead, in NH winter climate variations stem from circulation perturbations similar to the pattern of the Arctic Oscillation (AO) (cf. section 2.3).

To draw a conclusion from the above, changes in the absorbed solar radiation over the NH cryosphere play a very important role in global temperature distribution and circulation. The albedo has a direct impact on the absorbed solar radiation and is highly variable within cryospheric regions, e.g. within the Arctic, especially due to surface albedo temperature feedback processes.

Changes in absorbed solar radiation caused either by surface albedo changes or by orbital changes lead to changes in the meridional temperature gradient. The polar amplification of global warming under increasing GHG concentrations also leads to a changed pole to equator temperature contrast. Under future global warming conditions Fischer-Bruns et al. (2005) found a poleward shift of storm activity which is consistent with the findings of Yin (2005), who analysed an ensemble of scenario runs (Figure 1.2). Under increasing GHG concentrations a large majority of AOGCMs predict a shift towards the positive phase of the North Atlantic Oscillation (NAO) index (NAO: cf. section 2.3) (Stephenson et al. 2006).

This thesis aims to study the global scale influence of changes in the surface radiation budget in the NH energy sink region, the Arctic. The study focuses on long-term mean effects caused by the redistribution of energy fluxes between the Arctic and other parts of the earth. Besides examining global climate responses within climate conditions with fixed external forcing, also the impact of surface radiation changes within transient

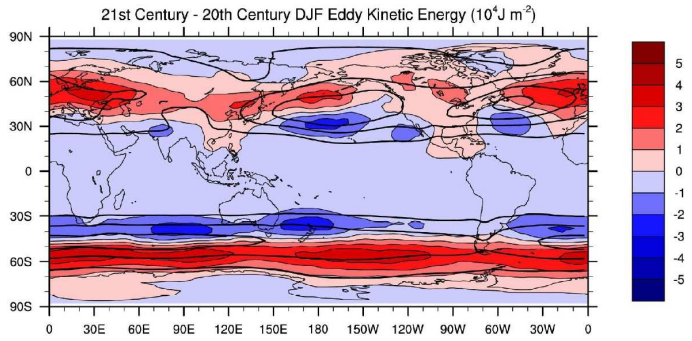

Figure 1.2: DJF 2–8 day eddy kinetic energy, vertically integrated from surface to 200 hPa. Ensemble mean from 15 models participating in the AR4 of the IPCC. Contour lines show 1981–2000 mean with a contour line interval of $10^5 \mathrm{J\,m^{-2}}$, shaded areas show the difference 2081–2100 minus 1981–2000 in $10^4 \mathrm{J\,m^{-2}}$. (From Yin 2005).

climate conditions is analysed. This allows an insight into the stability of the effect of changes in the energy sink region under changed global scale climate conditions. For practical reasons – the impact of an explicitly changed snow and sea ice albedo on the global scale circulation cannot be studied in an experiment performed in the real world – the global scale effect of cryospheric albedo changes is studied within the surrogate reality of an AOGCM with complex physics and parameterisations.

The albedo scheme for the cryosphere applied in the AOGCM ECHO-G (see section 3.1 for a detailed model description) consists of a quite simple surface temperature depending description of the broadband shortwave albedo of the cryosphere's surface. As it was not in the scope of the present thesis, a detailed description of the dependence of the ice and snow albedo from the snow age, incident angle, wavelength, grain size etc. is not given here. For a detailed description of the optical properties of snow and ice refer to Warren (1984) and Kokhanovsky and Zege (2004), for example.

As described above, feedback mechanisms have great impacts under changing climate conditions as they lead to non-linear responses of the climate system to perturbations. The surface albedo temperature feedback is a prominent example. Therefore in the scope of this study, experiments with improved albedo schemes in an equilibrium state were performed. By using the AOGCM ECHO-G to analyse the global scale effects of changes of the NH cryosphere and energy sink region on a global scale this study raises in particular the following questions:

- How does an improved sea ice and snow albedo scheme affect the Arctic sea ice cover?

- Are changes in the Arctic sea ice cover a direct locally thermodynamic response to a changed cryospheric albedo?

- Do changed surface conditions of the cryosphere lead to patterns of atmospheric changes that resemble those stemming from GHG changes?
- How much do changing surface conditions contribute to circulation changes?
- Under global climate change conditions (e.g. global warming) polar amplification of global temperature changes occurs as well as sea ice cover and circulation changes. Does a slightly different snow and sea ice albedo scheme strengthen or weaken the SAF so much that under changing climate conditions the above-mentioned changes differ in character and strength?
- How do circulation changes arising from long-term mean differences in meridional near surface air temperature gradients project on modes of natural atmospheric variability (NAO, AO and also the Antarctic Oscillation (AAO))?
- How large are the impacts of slight changes in physical parameterisations that include non-linear feedbacks in the light of changes in the debate on global warming?

Long-term control integrations as well as transient integrations were carried out to address the questions above.

The thesis is structured as follows:

- Relevant physical processes for the Arctic climate system playing a role within the scope of this thesis are discussed in chapter 2.
- Chapter 3 gives an overview of the AOGCM ECHO-G, its original and changed physical parameterisations, the different experimental set-ups, and selected statistical methods used to address the questions in the thesis.
- Chapter 4 shows the short-term response to perturbations in the surface albedo, focussing on the fast response of the sea ice, snow cover, and temperature.
- Chapter 5 discusses the long-term mean responses of the global climate system to changes in the Arctic's surface energy budget.
- The robustness of these changes under varying external forcing conditions which include future scenarios as well as paleoclimate forcing conditions are tested and discussed in chapter 6.
- Chapter 7 summarises the main findings of this study and gives suggestions for further analysis.

Chapter 2

The Arctic climate and related key processes

2.1 The Arctic climate

Several characterisations may be used to define the border of the Arctic region. Besides the astronomical definition of the Arctic as the region north of the Arctic Circle (66° 33′ N) (e.g. Figure 2.1) commonly used definitions are the northern tree line, the 10 °C July isotherm, and the permafrost ground. Each of the climatological definitions refers to a different size and region, which also varies under changed climate conditions. Therefore in this study the astronomically motivated definition will be used. The name "Arctic" stems from the ancient Greek word $\alpha\rho\kappa\tau o\varsigma$, meaning "bear" and therefore the land under the constellation of the Great Bear.

The Arctic climate is predominantly characterised by its negative radiation budget caused by low absorption of solar radiation. Firstly, for astronomical reasons less solar radiation reaches the top of the atmosphere around the poles than it does in lower latitudes, especially in winter of the respective hemisphere (Figure 2.2). Secondly, a large amount of the incoming radiation reaching the surface is reflected due to the high albedo of sea ice, snow, glaciers, tundra, and also the ocean water under a shallow incident angle. The Arctic emits more radiation than it receives. Thus the Arctic acts as a sink in the global energy budget. Energy (sensible and latent heat) is transported from the equator to the poles. The energy transport occurs in the atmosphere as well as in the ocean. The THC transports warm and salty water into the Arctic, where the ocean current cools, freshens, and sinks. Formation of dense water masses preferentially occurs in the Greenland-Iceland-Norwegian Seas and the Labrador Sea (e.g. Marshall and Schott 1999). The cooler and fresher dense water flows in a deep current southward. Model studies indicate an intensification of the hydrological cycle leading to an increase in freshwater input into the Arctic Ocean (by P-E and runoff) and also a decrease in meridional overturning under global warming climate conditions accompanied by

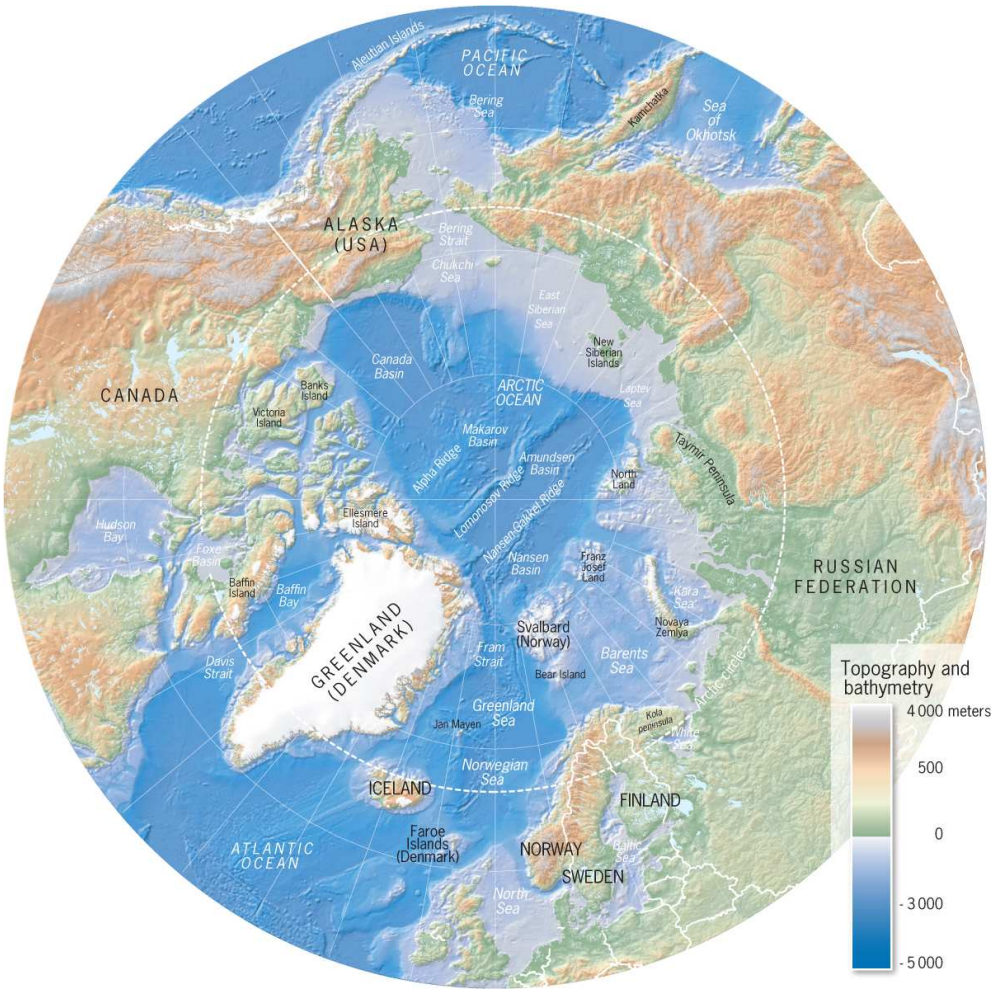

Figure 2.1: Topography and bathymetry of the Arctic (from UNEP/GRID-Arendal 2006).

increased freshwater input into the Arctic (IPCC 2001). Excessive freshwater input into the sub-polar North Atlantic could suppress the THC with implications for the European near surface air temperature (T_{2m}) by dropping the T_{2m} several K (e.g. Vellinga and Wood 2002). The THC is probably the most prominent example of the Arctic's influence on the climate far behind the borders of the Arctic.

The Arctic climate is strongly influenced by positive feedback processes caused by sea ice and snow coverage. The surface albedo feedback (SAF) is a very simple feedback mechanism. Sea ice or snow becomes warmer or even melts, thus becoming less reflective for shortwave radiation, leading to a further warming that increases the absorption of shortwave radiation again. Once sea ice or snow has disappeared the much less reflective ocean water or soil absorbs more shortwave radiation and warms even more. Therefore both snow and sea ice play an important role in the polar amplification of global warming. Holland and Bitz (2003) stressed the importance of the mean state sea ice cover in a control climate for the magnitude and spatial distribution of high-latitude warming. In particular, they found a tendency of models with thin Arctic sea ice cover to produce a

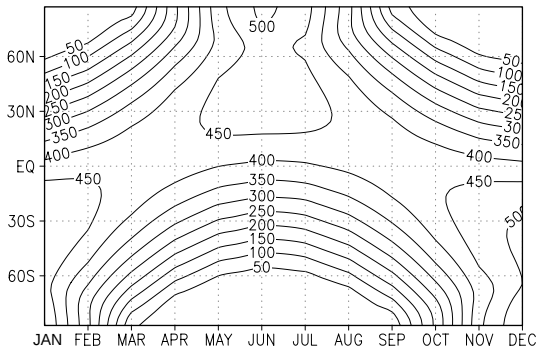

Figure 2.2: Monthly mean values of solar radiation incident on a horizontal surface at the top of the atmosphere as a function of latitude and date in $\mathrm{W\,m^{-2}}$, from ECHO-G, using a solar constant of 1365 $\mathrm{Wm^{-2}}$.

more pronounced polar amplification of global warming. Nevertheless, snow and sea ice temperature feedbacks are not necessary for a polar amplification of global warming, as demonstrated by Hall (2004), when he turned off the SAF in a model study. Also Winton (2006) found SAF a contributing, but not dominating factor for polar amplification. Cai (2006) presented how dynamical reasons account for the polar amplification without a SAF.

The climate of the Arctic is also characterised by great internal variability thus complicating the detection of a robust trend, despite the polar amplification of global warming. This is because the signal-to-noise-ratio is reduced by the very large internal variability including decadal scale climate variability. Two major warming events in the Arctic occurred in the 20$^{\mathrm{th}}$ century: From 1925 to 1944 and from 1978 to present (e.g. Delworth and Knutson 2000). The early 20$^{\mathrm{th}}$ century warming can be attributed at least partially to internal variability (Delworth and Knutson 2000) or most likely to internal variability (Bengtsson et al. 2004). The recent warming can be clearly distinguished from the early 20$^{\mathrm{th}}$ century warming (Johannessen et al. 2004). The early 20$^{\mathrm{th}}$ century warming was among other things limited to the Arctic only, whereas the current warming is not limited to the Arctic.

Furthermore, climate changes within the Arctic domain do not necessarily point towards the same direction. Often changes occur in a seesaw-like pattern. An example for an intra-annual temperature variability of a seesaw-like pattern is the well-known temperature seesaw between Greenland and northern Europe in winter that is caused by the NAO (c.f. section 2.3). Documents describing this temperature seesaw reach back to the 18$^{\mathrm{th}}$ century (Wanner et al. 2001). Climate change projects onto patterns of natural variability (e.g. Corti et al. 1999). A well-known pattern of natural variability is the NAO (cf. subsection 2.3). Within a changing climate the phase of the NAO and AO are also changing.

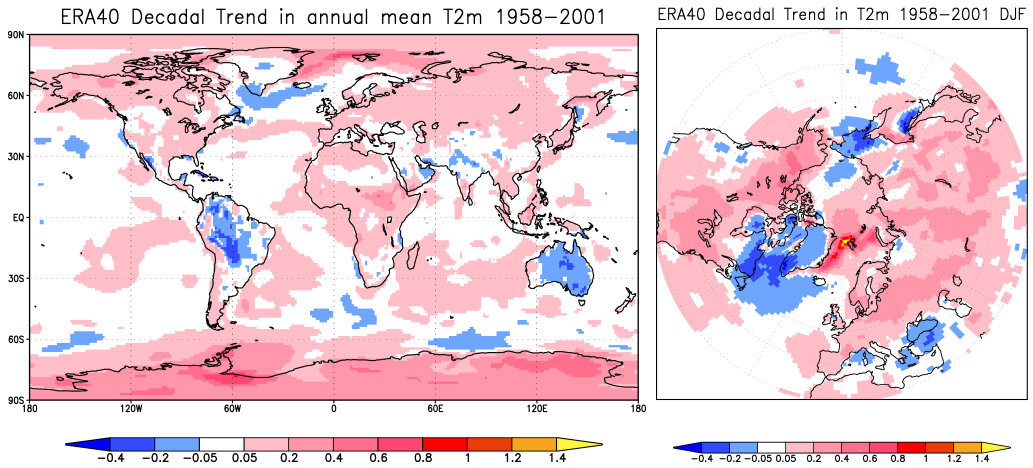

Figure 2.3: Observational T_{2m} trends in K per decade from ERA40 reanalysis data under global warming conditions and a shift towards NAO+ phase. Left: annual mean, right: winter (DJF) mean.

Long-term observations indicate a trend of the NAO towards its positive phase (e.g. Hurrell 1995 and updates). Circulation changes alter advection of air masses, leading to a regional cooling trend in a globally warming climate. Figure 2.3 gives an example of the AO / NAO influenced temperature trends over the last 40 years. Figure 2.3 ist based upon the ERA40 data set (ECMWF/DWD/DKRZ 2006), (Uppala et al. 2005). Due to the more positive NAO phase in winter, an increased advection of cold air masses from the central Arctic to the Labrador Sea region occurs, leading to more sea ice coverage, thus increasing the cooling effect in winter in this region. Additionally, an increased sea ice cover reduces the flux of sensible and latent heat from the ocean to the atmosphere contributing to a negative T_{2m} anomaly. On the other hand, more warm Atlantic air masses are transported towards Europe and the Svalbard region, leading to a milder winter. A similar pattern for the period from 1650 to 1850 was found by Shindell et al. (2001). They regressed reconstructed annual mean T_{2m} (Mann et al. 1998) on solar irradiance (Lean et al. 1995). In the Shindell et al. (2001) analysis the data were filtered on a time scale longer than 40 years and a time lag of $10 - 30$ years between irradiance and T_{2m} was considered.

The NH land area albedo has a pronounced annual cycle, stemming from the annual cycle of sea ice cover (section 2.2) and, to a greater extent, from the annual cycle of snow cover. Both snow and ice extent are strongly influenced by the SAF. The Northern Hemisphere (NH) snow cover ranges from a summer minimum of $4.0 \cdot 10^6$ km^2 to $4.6 \cdot 10^7$ km^2 in winter, as derived from satellite data (Serreze et al. 2000).

2.2 Arctic sea ice

Arctic sea ice plays a prominent role within the Arctic climate system. It has a much higher albedo (especially when covered with snow) than the open ocean. Therefore over

sea ice much less solar radiation is absorbed throughout the Arctic summer. Furthermore, the sea ice functions as an insulation layer between the ocean and the atmosphere. Fluxes of sensible heat and humidity over sea ice are much smaller compared to open water areas. Due to its very low heat conductivity, snow on sea ice increases the insulation effect of sea ice. The heat conductivity of snow is approximately one order of magnitude smaller than that of sea ice (Maykut and Untersteiner 1971). The heat conductivity of sea ice is in the order of 2.2 $\mathrm{W\,m^{-1}\,K^{-1}}$ (e.g. Peixoto and Oort 1992). As a consequence of the insulation effect of sea ice, the T_{2m} over sea ice may reach values as low as $-60\,^{\circ}\mathrm{C}$ (e.g. Peixoto and Oort 1992), whereas the ocean water temperature cannot drop below $-1.9\,^{\circ}\mathrm{C}$ (freezing point of ocean water) at a certain salinity concentration (approx. 35 psu). In summer the presence of melting sea ice keeps the uppermost layer of the Arctic Ocean water at $-1.9\,^{\circ}\mathrm{C}$.

Sea ice occurs in two primary forms: First-year ice and multi-year ice. The thickness of first-year ice ranges from a few cm at the southern sea ice edge up to 2.5 m in the central Arctic (ACIA 2005). Some first-year ice does not melt in summer and becomes multi-year ice. Multi-year sea ice covers approx. $5 \cdot 10^6\,\mathrm{km^2}$ (Johannessen et al. 1999). The Arctic sea ice circulates clockwise within the the Beaufort Gyre (Figure 2.4). The Transpolar Drift carries sea ice from the Siberian shelves to the Barents Sea and Fram Strait. On average, 10 % of Arctic sea ice is exported through the Fram Strait each year (ACIA 2005).

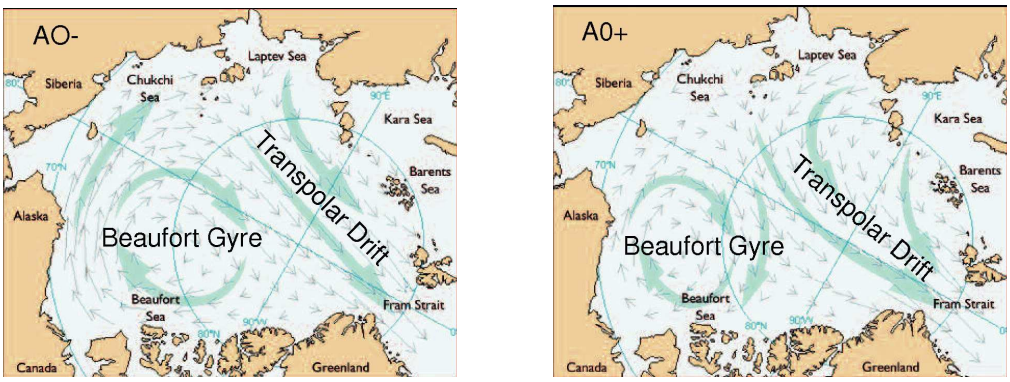

Figure 2.4: Sea ice drift patterns in the Beaufort Gyre and Transpolar Drift during years with AO- (left) and AO+ (right) phases (modified from ACIA 2005).

The Fram Strait ice export varies in cycles of about 9 years as demonstrated by Koenigk et al. (2006). This is in accordance to findings of Mysak and Venegas (1998), who suggested a 10-year cycle of Arctic climate variability including a clockwise propagation of sea ice anomalies in the Arctic with a corresponding oscillation of mean sea level pressure (SLP) anomalies. Venegas and Mysak (2000) isolated four dominant signals with periods of 6–7, 9–10, 16–20, and 30–50 years for the natural climate variability in the Arctic. They proposed three different causes for the Greenland Sea ice anomalies that are a result of the Fram Strait ice export anomalies: on a 6–7 year time scale a wind-driven export of anomalous ice volume from the East Siberian Sea, on a 9–10 year

time scale enhanced ice motion and export via the transpolar drift, and on a 16–20 year time scale the wind-driven motion of thick, old, and low-salinity sea ice from the offshore northern Canada into the outflow region. Fram Strait sea ice export anomalies also accounts for T_{2m} anomalies in the Labrador Sea. The resulting surface salt anomaly in the Labrador Sea explains more than 60 % of the air temperature variability (Koenigk et al. 2006). The advection of cold air masses from the Arctic during a high index phase of the NAO obviously also effects the T_{2m} in the Labrador Sea region. Koenigk et al. (2006) stated that whereas the NAOI (North Atlantic Oscillation Index) and the T_{2m} over the Labrador Sea are correlated with $r = -0.48$ there is no correlation between the Labrador Sea surface salinity and the NAO index. Therefore they supposed the two processes to be independent and suggest constructing an index built upon both salinity and NAOI. They showed that this index is correlated with 0.9 to the Labrador Sea T_{2m} anomalies.

Due to the large differences in surface heat flux between cases of sea ice cover and open water, sea ice anomalies also produce atmospheric responses. An example is given by Alexander et al. (2004), who showed in simulations with prescribed sea ice anomalies that positive sea ice anomalies west of Greenland and negative sea ice anomalies east of Greenland resemble the negative phase of the AO and NAO. The AO and NAO and also the opposite influence of the AO/NAO on Arctic sea ice cover and thickness will be discussed in section 2.3.

Nevertheless, even without strong trends in surface winds the observed thinning of the sea ice over large parts of the Arctic Ocean (Rothrock et al. 1999) can be reproduced by global climate models (Bitz and Roe 2004). Bitz and Roe (2004) also explained why under changing climate conditions the rates of change of the thickness of sea ice are largest over those areas that are initially covered with the thickest ice. They argued that thinner ice – when perturbed – does not need to thicken or thin as much as thicker ice to reach a new equilibrium state.

One has to distinguish between "sea ice area" (the sum of all areas covered with sea ice) and the "sea ice extent" (the area enclosed within the sea ice edge). The sea ice edge is commonly defined as where the sea ice concentration is above 15 % (e.g. Parkinson and Cavalieri (2002)). Between 1979 and 1999 the mean annual cycle of NH sea ice extent had a minimum extent of $6.9 \cdot 10^6$ km^2 and a maximum extent of $15.3 \cdot 10^6$ km^2 (Cavalieri et al. 2003).

Figure 2.5 demonstrates exemplarily the interactions within the sea ice albedo temperature feedback, including e.g. melt ponds and clouds.

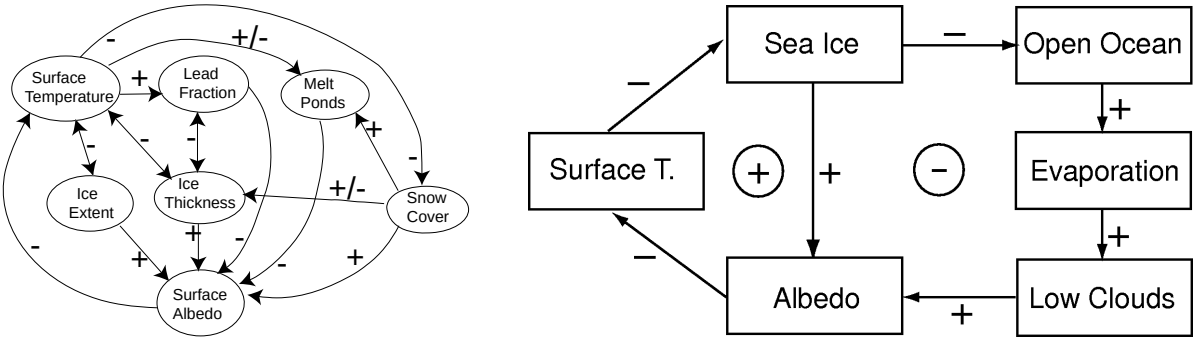

Figure 2.5: Sea ice albedo feedback (left) (after Curry et al. 1995) and sea ice albedo feedback including water vapour and clouds (right) (after (IPCC 2001)). A "+" indicates an increase of the first quantity leading to an increase of the second quantity, a "-" indicates the vice versa interaction. A "+/-" indicates either an unknown sign of the interaction or an interaction that changes its sign over the annual cycle. A circled "+" or "-" indicates whether a process is self-reinforced ("+") or damped ("-").

2.3 Arctic Oscillation (AO) and North-Atlantic Oscillation (NAO)

The AO (Arctic Oscillation) or NAM (Northern Annular Mode) was first introduced by Thompson and Wallace (1998) as the leading EOF of the anomaly of the mean sea level pressure (SLP) north of 20° N. A classical description of the NAO (North Atlantic Oscillation) is based on the standardised SLP difference between the Azores and Iceland, where the SLP gradient is a measure of the strength of the westerly flow over the North Atlantic. A detailed description of the concept of the NAO and its evolutionary history is given by Wanner et al. (2001). To include earlier observations than available from the Azores, the NAO index of Hurrell (1995) is based on the stations Lisbon, Portugal and Stykkisholmur, Iceland. The NAO index used in this thesis is based on the leading EOF of the anomaly of the SLP over the North Atlantic region (90° W – 30° E; 30° N – 90° N). The NAO index and the AO index are highly correlated. The NAO reflects the correlation between the SLP variability and its centres of action, whereas this it not the case for the AO (Ambaum et al. 2001). The AO is much more zonally symmetric than the NAO. It is also much less zonally symmetric than the AAO (Antarctic Oscillation), as the AO is much more influenced by the zonally non-symmetric land-sea distribution and also by the orography of the extratropical NH.

As an explanation for the observed increase of the AO phase until the last decade of the 20$^{\text{th}}$ century and in model simulations with increased GHG concentrations, Shindell et al. (1999) suggested that a warming in the tropical and midlatitude higher troposphere and a cooling in the stratosphere (both caused by increased GHG concentrations) enhance the meridional temperature gradient along a constant pressure level intersecting the tropopause. This leads to stronger zonal winds in the lower stratosphere that strengthen the polar vortex and lead to a shift towards the AO+ phase. In Figure 2.6 Overland and Wang (2005) illustrated dominant feedbacks and forcings of the

mechanism assumed to underlie a systematic shift towards a stronger and colder polar vortex in combination with an increase in the polarity of the AO.

Baldwin and Dunkerton (1999) showed that the AO signal propagates from the stratosphere to the troposphere. Furthermore, they proposed that the equatorial quasi-biennial oscillation (QBO) may act to modulate the AO in early winter. However, the QBO's influence on the AO as well as on the zonal wind speed in the NH is greatly diminished by February (Baldwin and Dunkerton 1999), (Baldwin and Dunkerton 1998). In a recent study, Camp and Tung (2007) used NCEP stratospheric temperatures from 1959 to 2005 and found a statistically significant influence of the ENSO on the Arctic stratosphere in boreal winter. In warm ENSO years the Arctic stratosphere was warmer than in cold ENSO years. The ENSO induced temperature differences were in the same order of magnitude as the QBO induced differences.

Besides the tropospheric warming and stratospheric cooling due to an increase of GHG concentrations, stratospheric ozone depletion also plays a major role in the cooling of the high-latitude lower stratosphere (cf. Figure 2.6). Absorption of solar radiation in the stratospheric ozone layer is the major source for the radiative heating of the stratosphere and therefore for the temperature inversion at the troposause. During the winter on each hemisphere catalytic ozone depletion occurs. With the onset of insolation in late winter less stratospheric ozone is present. Thus less solar radiation can be absorbed. As a consequence, the radiative heating of the stratosphere in spring is reduced, compared to a situation, where stratospheric ozone concentrations are higher.

The U.S. Climate Change Science Program (2006) report summarised the temperature trends in the lower atmosphere from the late 1950s on. The observations showed trends pointing towards different directions for the troposphere (warming) and the lower stratosphere (cooling). The cooling trend in the lower stratosphere was discontinued, when explosive volcano eruptions occurred. Three explosive volcano eruptions were identified in the time series of the global annual average temperatures in the stratosphere: Mt. Agung (1963), El Chichón (1982), and Mt. Pinatubo (1991). Derived from theoretical expectations the U.S. Climate Change Science Program (2006) predicted a warming of the surface and the low to mid troposphere and a cooling of the stratosphere as response to increased concentrations of well-mixed greenhouse gases. The same report assumed a negligible effect of land use and land cover changes on global annual average temperatures in the stratosphere.

Shindell et al. (1999) performed experiments with different versions of the GISS atmospheric general circulation model, including a 9 vertical level (up to 10 hPa) as well as a 23 vertical vertical level (up to 0.002 hPa) set-up. As in GHG concentration change simulations with the 9 vertical level version no trend in the AO occurred, the authors argued that only models with a realistic representation of the stratosphere are able to

produce a trend in the AO index when forced with increasing GHG concentrations. Nevertheless, Zorita and González-Rouco (2000) found that also the model ECHAM4, which lacks a realistic representation of the stratosphere, shows a trend towards a positive AO index under increasing GHG concentrations. ECHAM4 has admittedly only 7 levels above 200 hPa, the highest level at 10 hPa, and no representation of ozone and volcanic aerosols in the stratosphere. However, in ECHAM4 upper tropospheric temperatures (especially in the tropics) increase and stratospheric temperatures decrease, when GHG concentrations increase (e.g. Figures 5.17 and 5.18 in the current study). This leads to the changed meridional temperature gradient along a pressure level intersecting the tropopause as described by Shindell et al. (1999). Also the majority of models participating in the AR4 of the IPCC show an increase in NAO+ phase with increasing GHG concentrations (Stephenson et al. 2006).

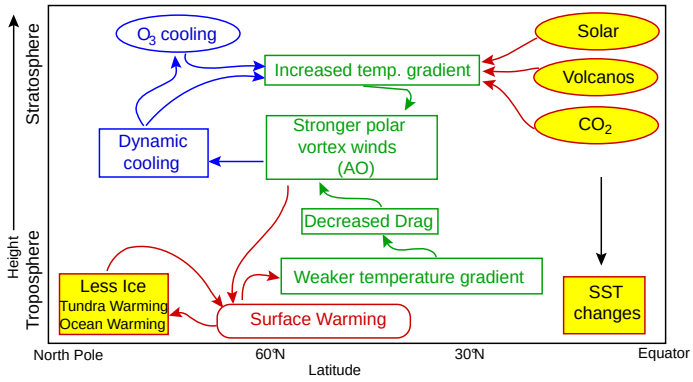

Figure 2.6: A conceptual model of forcings and feedbacks of the polar vortex (after Overland and Wang 2005).

Recent observations indicated a decrease of the NAO, after the NAO especially increased in the last decade of the 20th century (Overland and Wang 2005). Analysing NCEP reanalysis data of zonal mean wind speed and zonal mean temperatures for the NH troposphere and stratosphere, Hu et al. (2005) pointed out that they found trends with opposite signs between early winter (November–December (ND)) and late winter (February–March (FM)). Their results indicate a trend towards a colder and stronger polar vortex in FM while the trends they found in ND resemble a trend towards a low-index polarity of the AO.

AO and Sea ice

The impact of the AO on the Northern Hemispheric sea ice cover is still under debate. Some studies indicate that a positive AO or NAO phase lead to an increasing Fram Strait sea ice export, reducing the Arctic sea ice (e.g. Kwok and Rothrock 1999). Others (e.g. Koenigk et al. 2006) stated that there is neither a direct influence of the AO on the Fram Strait sea ice export nor even on the SLP gradient across the Fram Strait. Liu et al. (2004) demonstrated that neither the ENSO nor the AO can explain the amount of

regional sea ice decreasing (or increasing) trends between 1978 and 2002. Nevertheless, on intra-seasonal (only AO) and inter-annual time scales the sea ice concentration is highly influenced by the ENSO and AO (Figure 2.7). Rigor et al. (2002) also argued that the trend towards a high index polarity of the AO should at least partially lead to a thinning of the Arctic Ocean's sea ice cover.

Maslanik et al. (2007) raised the question as to whether the recent decrease of AO and the nevertheless continuously shrinking NH sea ice cover mean that the atmospheric circulation no longer plays a dominant role in the reduction of the NH sea ice cover. As a result, they claimed that even in a neutral phase of the AO "regional atmospheric circulation remains a significant factor in recent reductions in ice cover".

The ENSO signal influences NH sea ice cover by changing the pole-to-equator meridional temperature gradient. According to e.g. Liu et al. (2004) this change is of opposite sign in the Atlantic basin to that in the Pacific basin. During El Niño events an intensification in the pole-to-equator meridional temperature gradient in the (eastern) Pacific basin leads to an intensification of the Hadley Cell in the eastern tropical Pacific, an equatorward shift of the subtropical jet, an equatorward shift of the storm track in the northeast Pacific / northwest America sector and also a changed Ferrel Cell (Liu et al. 2004). A more detailed description is given by Liu et al. (2004), for example.

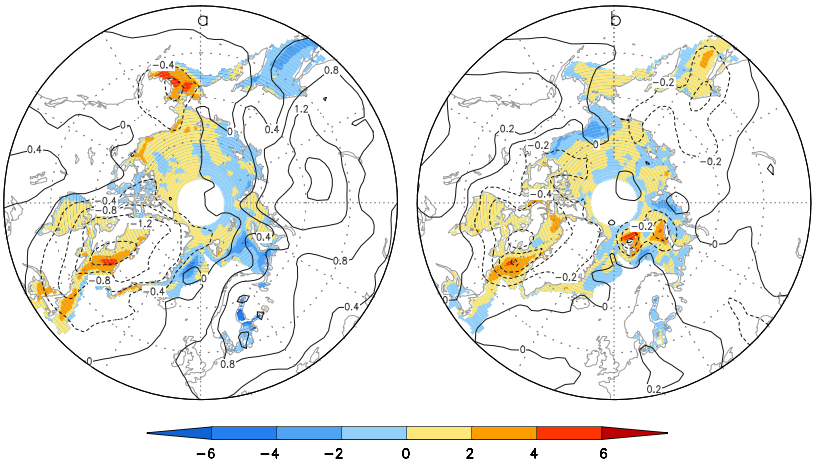

Figure 2.7: Regression maps of satellite-derived Arctic sea ice concentrations (%, shaded) and NCEP T_{2m} (K, contour) on the standardised AO (a) and ENSO (b) indices (from Liu et al. 2004).

The impact of changed temperature gradients between the equator and the poles in respect to the importance of sea ice cover changes was analysed by Rind et al. (2001). The authors demonstrated that changes in the temperature gradient alone do not profoundly affect the SLP over the Arctic, whereas a combination of an increased (decreased) gradient and increased (decreased) Arctic sea ice cover lead to an increase (decrease) of SLP over the Arctic, inducing circulation changes similar to the NAO pattern.

Chapter 3

Set-up of the experiment

The simulations were carried out with the coupled atmosphere ocean general circulation model (AOGCM) ECHO-G. The experiment used different parameterisations and the model was forced with different external forcings. These forcings, parameterisations, and the model are described below.

3.1 Model description: ECHO-G

ECHO-G (Legutke and Voss 1999) consists of the spectral atmospheric GCM ECHAM4 (Roeckner et al. 1996) and the ocean model HOPE-G (Wolff et al. 1997). The latter includes a thermodynamic / dynamic sea ice module with a viscous-plastic rheology according to Hibler (1979) and snow cover. In this study ECHAM4 was run in a horizontal resolution of T30 (approx. 3.75°) while HOPE-G was run in a horizontal resolution of T42 (approx. 2.8°). ECHAM4 and HOPE-G are coupled via the OASIS software (Terray et al. 1998). Figure 3.1 gives an overview of the horizontal resolution and the land-sea-masks of ECHAM4 and HOPE-G.

ECHAM4

ECHAM4 is the fourth generation of the ECHAM model series developed at the Max Planck Institute for Meteorology (MPIM) in Hamburg. The ECHAM model series originally stems from the spectral numerical weather prediction model of the European Centre for Medium-Range Weather Forecasts (ECMWF). At MPI some physical parameterisations were adapted to climate simulation requirements. ECHAM4 is based on primitive equations. Prognostic variables are vorticity, divergence, temperature, log surface pressure, water vapour, and cloud water. The model has a 19-level hybrid sigma-pressure coordinate system with highest vertical resolution in the boundary layer and extends to a pressure level of 10 hPa (approx. 30 km). The lowest layer in ECHAM4 lies about 30 m above the surface. For use within ECHO-G, ECHAM4 was modified

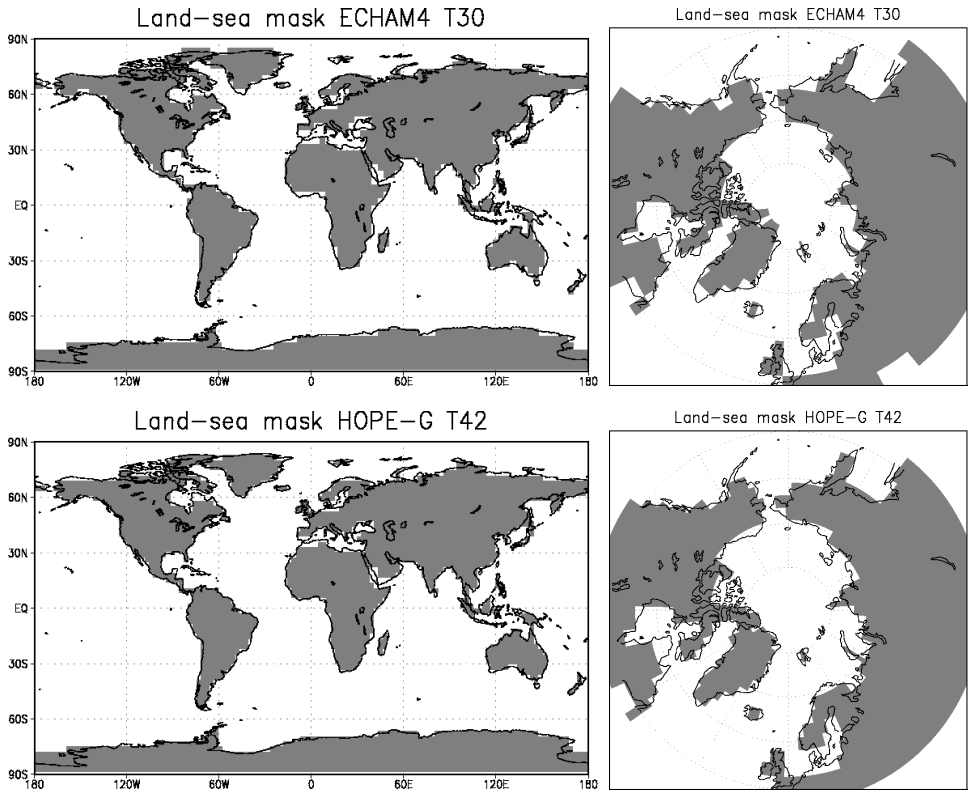

Figure 3.1: Land-sea masks of ECHO-G. Upper pictures: ECHAM4, lower pictures: HOPE-G.

slightly in order to properly account for a sub-gridscale partial sea ice cover as described in Grötzner et al. (1996). Heat, freshwater, and momentum fluxes are calculated separately for the ice-covered and the ice-free part of each grid cell. The resulting fluxes for each part (ice-covered / ice-free) are passed separately to the ocean-sea-ice-model. Other modifications for use as part of the coupled AOGCM concern the treatment of the net atmospheric freshwater fluxes on continental glaciers (Greenland and Antarctica) and the continental runoff. For continental runoff a routing scheme (Sausen et al. 1994) is implemented. The net freshwater flux to Greenland and Antarctica is instantaneously distributed to the surrounding ocean grid cells of the respective region. The performance of the specified T30/L19 version of ECHAM4 was described by Stendel and Roeckner (1998). Müller (2003) found that the Northern Hemispheric (NH) atmospheric blocking frequency simulated within ECHO-G (with ECHAM4 in T30 resolution) is underestimated by 50 % compared to observations and ECHAM4 T42 stand-alone runs. Surface characteristics (elevation, forest cover, and background surface albedo) that play an important role within the scope of this study are displayed in Figure 3.2.

HOPE-G

The ocean general circulation model (OGCM) HOPE-G (Hamburg Ocean Primitive Equation) used in ECHO-G has a vertical resolution of 20 uneven distributed levels and is formulated on a Gaussian T42 Arakawa-E grid with a horizontal resolution of about 2.8°.

Towards the equator the horizontal resolution of the grid refines up to 0.5° allowing a more realistic representation of ENSO variability (Marsland et al. 2003). A detailed description of the climatology of HOPE-G was given by Legutke and Maier-Reimer (1999).

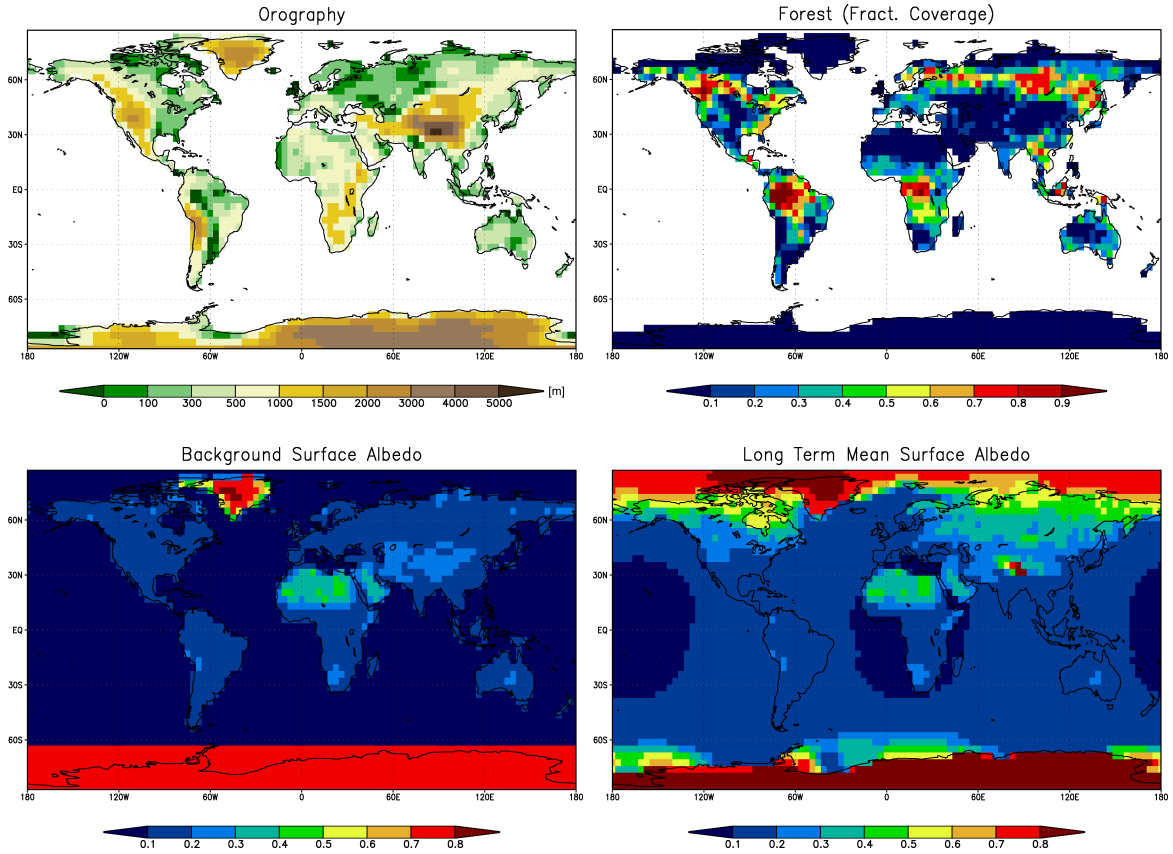

Figure 3.2: Orography, forest cover, and albedo of ECHO-G.

Coupling, flux correction and sensitivity to forcing

The coupling and also interpolation between ECHAM4 and HOPE-G is done by the OASIS (Ocean Atmosphere Sea Ice Soil) software. OASIS transfers information about sea surface conditions to the atmosphere model and passes heat, freshwater, and momentum to the ocean. The interpolation is necessary because of the finer grid size of the ocean model (Figure 3.1).

To avoid climate drift, flux corrections for heat and freshwater flux are applied. The flux correction is adapted to present day climate conditions, held constant in time, and its global average is zero (e.g. Zorita et al. 2004).

In ECHO-G the global annual mean T_{2m} increases by 1.70 K at twice the present day CO_2 concentrations. Therefore ECHO-G lies in the middle of the range of IPCC

TAR simulations with a 1 % annual increase of atmospheric greenhouse gases (Zorita et al. 2004).

Details about internal variability were given by e.g. Min et al. (2005, and references therein).

3.2 Experimental set-up: Forcing and albedo scheme

Several model runs with ECHO-G were performed for use within the study. In combination with already existing simulations with ECHO-G these new runs build the basis for the analysis within this thesis. The runs differ with respect to the forcing and the sea ice and snow albedo parameterisation. Table 3.1 provides an overview of the analysed runs, including their forcing and starting conditions.

All control and forced runs performed by the author of the current study start from a 1000-year historical reconstruction run (HIST) of ECHO-G made by F. González-Rouco (González-Rouco et al. 2003). For information about the forcing (historical reconstructions (hereafter: HR) of GHG concentrations, volcanic aerosols, and solar activity as well as constant external forcing and IPCC SRES emission scenarios) refer to section 3.2.1 and Figure 3.4.

The temporal evolution of the global annual mean T_{2m} of these runs is shown in Figure 3.3 providing an impression of the initial conditions of each run. Figure 3.3 and Table 3.1 include also a 1000-year control run (A05) of ECHO-G which was run with present day forcing conditions by S. Legutke from Max Planck Institute for Meteorology (MPIM), Hamburg (e.g. Min et al. 2005). As the A05 control run showed too little NH sea ice coverage compared to observations and to the HIST run at the end of the 20^{th} century, the calendar year 1990 of the HIST run was chosen to initialise the performed control runs.

The simulation runs were performed as follows:

- Two control runs with present day forcing conditions, each covering 510 years:
  - CTRL_O: Control run with original ECHAM4 albedo scheme.
  - CTRL_NA: Control run with new albedo scheme.
- Forced runs using the new albedo scheme:
  - H_B2_NA: Historical reconstruction run that was forced with the same forcing conditions as the HIST run (González-Rouco et al. 2003) until 1990. This run started in 1451 and was forced from 1991 to 2100 with IPCC SRES B2 forcing conditions.

Table 3.1: Model simulations with ECHO-G. The control run A05 was performed by S. Legutke from MPIM. The forced runs HIST, B2, and A2 were performed by F. González-Rouco. For a description of the forcing data (historical reconstruction: HR, IPCC SRES: A2 and B2) refer to Figure 3.4. The B2_O and the HIST run build the HIST & B2 run.

Run	Alb. Par.	Forcing	Years	Calendar Year	Starting from
A05	old	const. 1990	1083	–	–
CTRL_O	old	const. 1990	510	–	calendar year 1990 of HIST
CTRL_NA	new	const. 1990	510	–	calendar year 1990 of HIST
HIST	old	HR	1200	901–2100	model year 100 of A05
B2_O	old	B2	1200	901–2100	calendar year 1990 of HIST
A2_O	old	A2	110	1991–2100	calendar year 1990 of HIST
H_B2_NA	new	HR & B2	650	1451–2100	calendar year 1450 of HIST
A2_NA	new	A2	110	1991–2100	calendar year 1990 of H_B2_NA

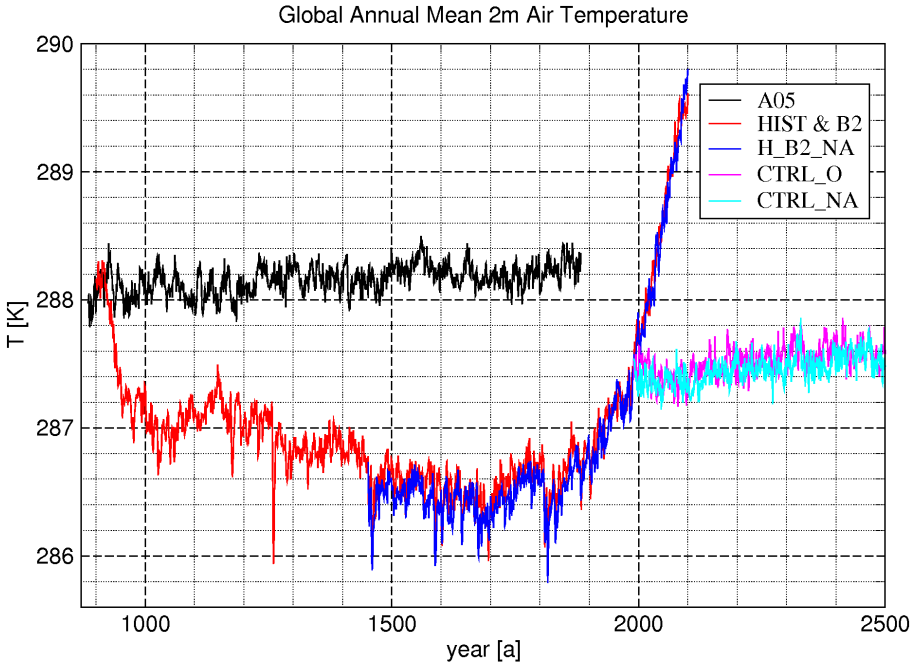

Figure 3.3: Temporal evolution of the global annual mean near surface air temperature (T_{2m}). A05 is the identifier of a control run performed by S. Legutke from MPIM.

– A2_NA: This run started in 1991 and was forced from 1991 to 2100 with IPCC SRES A2 forcing conditions (not shown in Figure 3.3).

3.2.1 Forcings

To provide the model with boundary values, a set of varying (or constant) forcing data was used. The model simulations carried out can be divided into three categories: Paleoclimate simulations, future scenarios, and quasi-equilibrium simulations. Forcing data based on historical reconstructions are necessary to provide paleoclimate simulation runs with a set of boundary values. Forcing data for future scenarios are based on assumptions of the development of GHG emissions, for example. A constant external forcing is used to perform control experiments with specified boundary conditions at fixed levels, such as constant pre-industrial or present day climate conditions.

The forcing for the historical reconstruction runs used the same forcing as described in the works of González-Rouco et al. (2003) and Zorita et al. (2004). A variable activity of the sun, volcanic aerosols, and a variable concentration of greenhouse gases (CO_2, CH_4, and N_2O) were included. The varying sun activity leads to a varying solar constant. The variability of the solar constant and the effect of volcanic aerosols were used in combination to create a so-called "effective solar constant" as done by Crowley (2000). In a simplified way, the volcanic aerosols were assumed to reduce the incoming solar radiation in a manner as there was less incoming solar radiation at the top of the atmosphere. Thus the net radiative forcing of volcanic aerosols was treated as there was a comparable decrease in the solar constant. Crowley (2000) estimated from ice core data the global annual means of optical depth and translated those estimated optical depth data into a shortwave radiative forcing according to the net cooling effect of volcanic eruptions. Crowley (2000) also combined this volcanic forcing with reconstructions of the solar constant. Those reconstructions are based on a method using cosmogenic ^{10}Be isotopes (Bard et al. 2000) and on sun spots counts (Lean et al. 1995). Volcanic and solar forcing together made up the "effective solar constant". A major shortcoming of this particular approach is the lack of reproduction of the increased absorption of shortwave radiation in the stratosphere. Thus the model cannot simulate the observed stratospheric warming after explosive volcanic eruptions as a direct response to an increased aerosol loading in the stratosphere. Moreover, neither the latitudinal difference in volcanically induced changes in aerosol optical depths nor the the timing of the volcanic eruptions within the annual cycle were taken into account. CO_2 and CH_4 concentrations were derived from air bubbles trapped in Antarctic ice cores (Etheridge et al. 1996), (Blunier et al. 1995), respectively. N_2O concentrations were used in the same manner as in Roeckner et al. (1999). Figure 3.4 gives an overview of the temporal evolution of the reconstructed forcing.

The future scenario forcing is based on the IPCC SRES report (IPCC 2001). Forcing conditions for the SRES B2 scenario are found in Figure 3.4.

The forcing of the control runs was done with the following constant present day

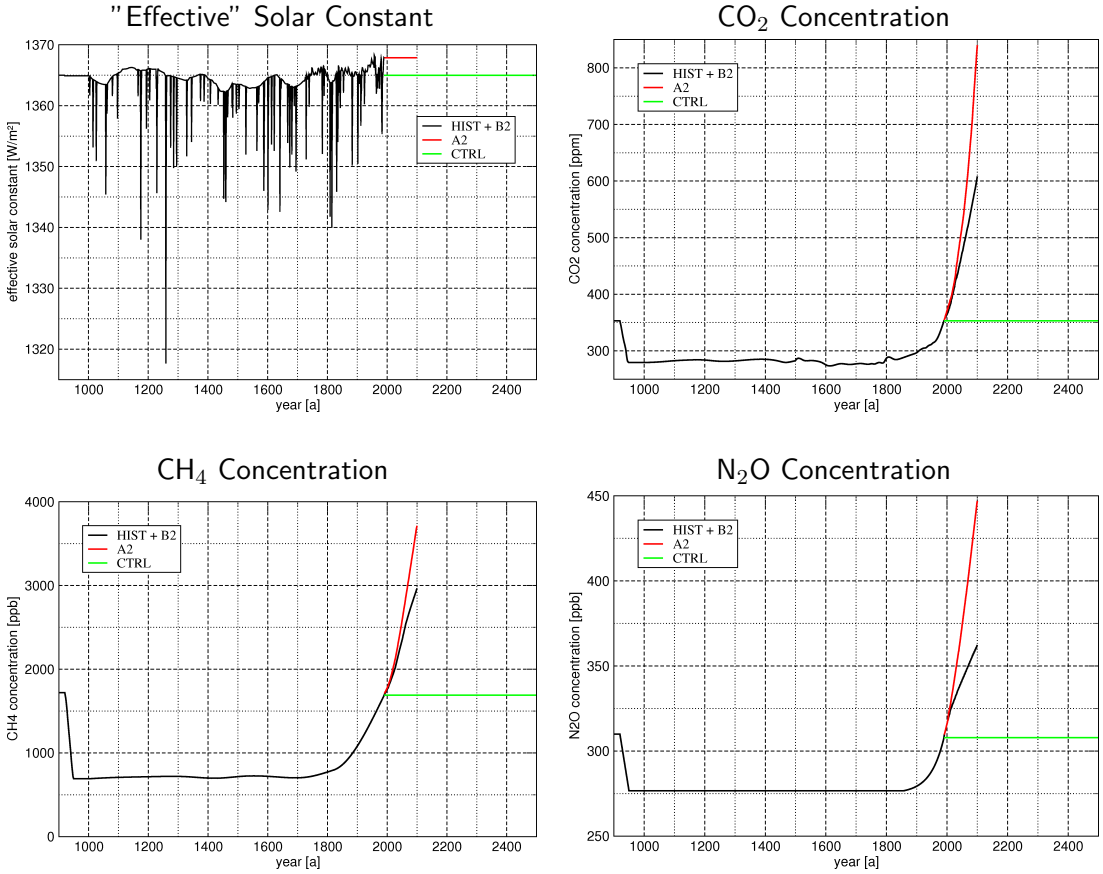

Figure 3.4: External forcings for ECHO-G. The sharply downward pointing peaks in the "effective solar constant" curve arise from volcanic eruptions, whereas the smoother changes in the "effective solar constant" stem from variations of the sun's activity. The A2_O, B2_O, A2_NA, and B2_NA runs were forced with an "effective solar constant" of 1367 Wm^{-2}.

(1990) values: "effective solar constant": 1365 Wm^{-2}, CO_2: 353 ppm, CH_4: 1689 ppb, N_2O: 307.9 ppb (Figure 3.4). The "effective solar constant" was chosen as 1365 Wm^{-2} to be consistent with the long-term mean and also with the mean of the last couple of decades, which is below the solar constant of approx. 1367.8 Wm^{-2} due to volcanic eruptions. For the same reason also Min et al. (2006), for example, choose 1365 Wm^{-2} as the solar constant for their scenario simulations with ECHO-G.

3.2.2 Sea ice and snow albedo parameterisation

Both improved and original schemes for sea ice and snow albedo use surface temperature dependent realisations of the albedo values.

Køltzow et al. (2003) tested different sets of surface temperature dependent snow and sea ice albedo schemes against AVHRR satellite data (Xiong et al. 2002) (Figure 3.5) and data from the SHEBA (Uttal et al. 2002) field experiment, respectively. The SHEBA experiment was performed in the western Arctic Ocean between Alaska and the

North Pole using an icebreaker as a platform. The SHEBA ice station drifted for more than one year with the ice. The measurements (solar radiation, surface temperature) at the SHEBA (Surface Heat Budget of the Arctic Ocean) site were used to compute the absorbed solar radiation for this site during the campaign. Køltzow et al. (2003) combined several estimates of sea ice albedo and melt pond fraction from literature (Curry et al. (2001), Curry et al. (1996), Grenfell and Perovich (1984), Grenfell et al. (1994), Perovich et al. (2002), Lindsay and Rothrock (1994), Tschudi et al. (2001), Langleben (1969)) such that the deviations of the computed absorbed solar radiation from the measurement data are minimal for the particular SHEBA period (Table 3.2).

Table 3.2: Monthly mean differences of simulated absorbed solar radiation to measurements at the SHEBA site in Wm^{-2} (from Køltzow et al. (2003)).

Albedo scheme	month							total period
	FEB	MAR	APR	MAY	JUN	JUL	AUG	(FEB - MAR 1997)
ECHAM4	1.4	6.1	11.9	15.7	22.9	-9.3	-22.3	3.8
New	-0.9	-0.4	-0.7	-2.8	3.6	8.1	-6.7	0.0

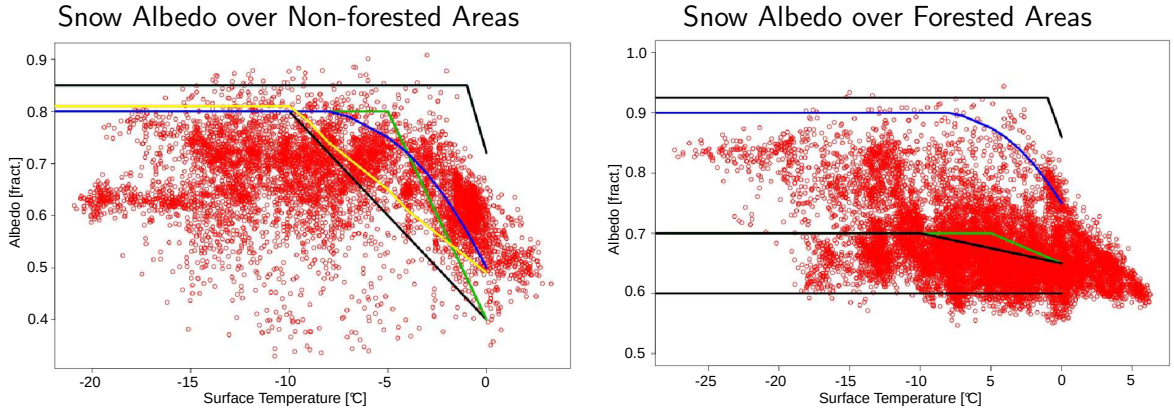

Figure 3.5: Estimated broadband snow albedo from AVHRR observations for non-forested areas (left) and forested areas (right) marked by red dots and respective curves of different surface temperature dependent snow albedo parameterisations (from Køltzow et al. (2003)). Curves: ECHAM4: lower black curve (second lowest black curve for forested areas), new albedo scheme (Roesch 2000): blue curve. Other schemes: ECHAM5: green curve, Roesch et al. (2002): yellow curve, NCAR: upper black curve. Further scheme for forested areas: Viterbo and Betts (1999) (lower black curve).

In contrast to the ECHAM4 scheme, the new scheme for sea ice albedo (suggestion 2 in Køltzow et al. (2003)) considers the effect of melt ponds and – in the case of thin ice (less than 25 cm thickness) – a linear transition of sea ice albedo towards open water albedo. In the case of bare ice the new sea ice albedo scheme gives much lower values throughout

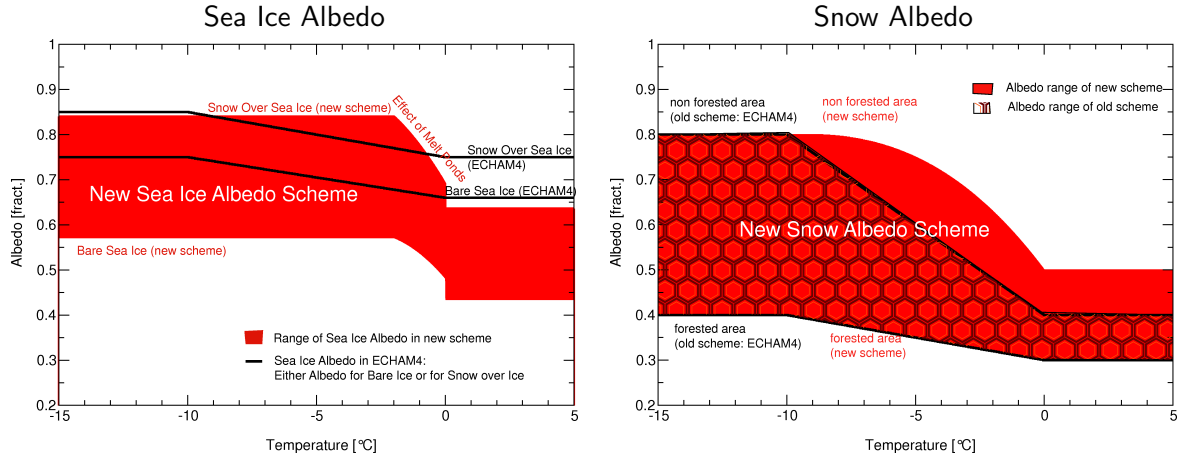

Figure 3.6: Sea ice (left) and snow (right) albedo parameterisation. Black lines and the area denoted by black honeycombs indicate the surface temperature depending snow and ice albedo scheme originally applied within ECHAM4. The red areas denote the range of the surface temperature depending albedo within the new scheme. The actual parameterised albedo value within the range between the upper and lower limit of the albedo for a specific surface temperature depends on the fractional coverage of snow (over sea ice or over land areas, respectively).

the whole temperature range. For snow covered sea ice the new scheme yields a higher albedo between $-9\,°\mathrm{C}$ and $-1\,°\mathrm{C}$. Below $-9\,°\mathrm{C}$ and above $-1\,°\mathrm{C}$ the new sea ice albedo is lower due to a lower maximum albedo (0.84 to 0.85) and the parameterised effect of melt ponds, respectively (Figure 3.6). In general, under the constraint of SHEBA boundary conditions the new scheme absorbs less solar radiation ($-3.8\ \mathrm{W\,m^{-2}}$) averaged from February to August 1998 than the original scheme (Køltzow et al. 2003) (Table 3.2).

In the new snow albedo scheme the original ECHAM4 scheme is replaced by the Roesch (2000) polynomial approach explicitly for unforested areas. The new snow albedo parameterisation generally leads to higher albedo values above $-10\,°\mathrm{C}$ if the land area is not completely forested. Below $-10\,°\mathrm{C}$ or for completely forested areas no difference between the two albedo schemes exists (Figure 3.6).

The new sea ice and snow albedo parameterisation was applied to the Northern Hemisphere (NH) explicitly, while all parameterisations for the Southern Hemisphere remain unchanged.

Original ECHAM4 sea ice and snow albedo scheme

- sea ice

For snow covered sea ice:

$$\begin{aligned} \alpha &= 0.85 && && T_s &< -10\,°\mathrm{C} \\ \alpha &= 0.75 + T_s \cdot (0.75 - 0.85)/10\,°\mathrm{C} && -10\,°\mathrm{C} \leq\ & T_s &\leq\ 0\,°\mathrm{C} \\ \alpha &= 0.75 && && T_s &> 0\,°\mathrm{C} \end{aligned}$$

where α is the sea ice albedo and T_s is the surface temperature of the sea ice in °C.

And for bare sea ice:

$$\begin{array}{lcll} \alpha & = & 0.75 & T_s < -10\,^\circ\mathrm{C} \\ \alpha & = & 0.66 + T_s \cdot (0.66 - 0.75)/10\,^\circ\mathrm{C} & -10\,^\circ\mathrm{C} \leq T_s \leq 0\,^\circ\mathrm{C} \\ \alpha & = & 0.66 & T_s > 0\,^\circ\mathrm{C} \end{array}$$

- snow

Snow albedo over non-forested areas:

$$\begin{array}{lcll} \alpha & = & 0.8 & T_s < -10\,^\circ\mathrm{C} \\ \alpha & = & 0.4 + T_s \cdot (0.4 - 0.8)/10\,^\circ\mathrm{C} & -10\,^\circ\mathrm{C} \leq T_s \leq 0\,^\circ\mathrm{C} \\ \alpha & = & 0.4 & T_s > 0\,^\circ\mathrm{C} \end{array}$$

Snow albedo over forested areas:

$$\begin{array}{lcll} \alpha & = & 0.4 & T_s < -10\,^\circ\mathrm{C} \\ \alpha & = & 0.3 + T_s \cdot (0.3 - 0.4)/10\,^\circ\mathrm{C} & -10\,^\circ\mathrm{C} \leq T_s \leq 0\,^\circ\mathrm{C} \\ \alpha & = & 0.3 & T_s > 0\,^\circ\mathrm{C} \end{array}$$

The new albedo scheme (according to Køltzow et al. (2003))

- sea ice

The new sea ice albedo scheme takes into account the effect of melt ponds. It is assumed that below a surface temperature of $-2\,^\circ\mathrm{C}$ no melt ponds occur. Therefore the fractional coverage of melt ponds on the sea ice is calculated from the surface temperature of the sea ice:

$$\begin{array}{lcll} \Delta_{melt\,ponds} & = & 0.11 \cdot (2 + T_s) & -2\,^\circ\mathrm{C} \leq T_s \leq 0\,^\circ\mathrm{C} \\ \Delta_{melt\,ponds} & = & 0.22 & T_s > 0\,^\circ\mathrm{C} \end{array}$$

The albedo of a melt pond is calculated also from the surface temperature of the sea ice:

$$\begin{array}{lcll} \alpha_{melt\,ponds} & = & 0.36 - 0.1 \cdot (2 + T_s) & -2\,^\circ\mathrm{C} \leq T_s \leq 0\,^\circ\mathrm{C} \\ \alpha_{melt\,ponds} & = & 0.16 & T_s > 0\,^\circ\mathrm{C} \end{array}$$

Snow covered sea ice albedo (α_{scsi}):

$$\begin{array}{lcll} \alpha_{scsi} & = & 0.84 & T_s < 0\,^\circ\mathrm{C} \\ \alpha_{scsi} & = & 0.77 & T_s \geq 0\,^\circ\mathrm{C} \end{array}$$

Bare sea ice albedo (α_{bsi}):

$$\begin{aligned} \alpha_{bsi} &= 0.57 && T_s < 0\,^{\circ}\mathrm{C} \\ \alpha_{bsi} &= 0.51 && T_s \geq 0\,^{\circ}\mathrm{C} \end{aligned}$$

Finally the sea ice albedo is calculated from the required inputs sea ice snow cover and surface temperature:

$$\alpha = (\Delta_{scsi} \cdot \alpha_{scsi} + \Delta_{bsi} \cdot \alpha_{bsi}) \cdot (1 - \Delta_{melt\ ponds}) + \Delta_{melt\ ponds} \cdot \alpha_{melt\ ponds} \tag{3.1}$$

- snow

For non-forested areas the original ECHAM4 snow albedo scheme is replaced by the Roesch (2000) scheme:

$$\alpha = 0.5 + a_1 \cdot T_s + a_2 \cdot T_s^2 + a_3 \cdot T_s^3 + a_4 \cdot T_s^4, \tag{3.2}$$

with $a_1 = -7.582627 \cdot 10^{-2}$, $a_2 = -5.5360168 \cdot 10^{-3}$, $a_3 = -5.2966269 \cdot 10^{-5}$, $a_4 = 4.2372742 \cdot 10^{-6}$ where the temperature T_s is given in °C. The maximum and minimum limits are set to 0.8 ($T_s \leq -10\,^{\circ}\mathrm{C}$) and 0.5 for melting snow, respectively (Figure 3.6).

An implementation of the new albedo scheme into the regional climate model HIRHAM forced with NCEP reanalysis data led to an improvement of Arctic T_{2m} compared to the Willmott and Rawlins (1999) climatology data set (Dethloff et al. 2006).

3.3 Statistical analysis

Many of the responses of the climate system to changed albedo conditions described in the chapters below may be defined as changes in frequency distribution and difference of means. Therefore both the Student's t test and the Kolmogorov-Smirnov test (cf. von Storch and Zwiers 1999) are briefly discussed. Formally, the application of those classical inference methods requires sample data that are independent and identically distributed (iid) (cf. von Storch and Zwiers 1999).

t-test

The Student's t test is a parametric test of equality of means. Thus the null hypothesis that two univariate variables $\mathbf{X}$ and $\mathbf{Y}$ have equal mean is formulated: $\mathrm{H}_0 : \mu_X = \mu_Y$.

The t test can be applied under the following assumptions (e.g. von Storch and Zwiers 1999):

1. Every realisation of $\mathbf{X}$ and $\mathbf{Y}$ occurs independently of all other realisations of $\mathbf{X}$ and $\mathbf{Y}$,
2. the distribution generating the realisations of $\mathbf{X}$ and $\mathbf{Y}$, respectively, is the same for each in the $\mathbf{X}$ ($\mathbf{Y}$) sample,
3. the distributions are normal and have the same variance.

Then the test statistic is given by

$$t = \frac{\hat{\mu}_X - \hat{\mu}_Y}{S_p \sqrt{\frac{1}{n_X} + \frac{1}{n_Y}}}, \tag{3.3}$$

with n_X and n_Y being the size of X and Y, respectively, $\hat{\mu}_X$ and $\hat{\mu}_Y$ being the means of $\mathbf{X}$ and $\mathbf{Y}$, respectively. S_p is the pooled estimate of the common standard deviation which reads as follows:

$$S_P^2 = \frac{\sum_{i=1}^{n_X} (\mathbf{x}_i - \hat{\mu}_X)^2 + \sum_{i=1}^{n_Y} (\mathbf{y}_i - \hat{\mu}_Y)^2}{n_X + n_Y - 2} \tag{3.4}$$

The test of the null hypothesis is carried out against the following alternative hypothesis: $H_1 : \mu_X \neq \mu_Y$.

However, meteorological data often violate the conditional assumptions of the t test: Whereas some simulation data (e.g. the NAO index) are largely iid (independent and identically distributed), others (e.g. sea ice) are highly auto-correlated, therefore contravening the independence assumption. Further they may have different variances according to different parameterisations and different realisations of climate states. The data are also spatially correlated. The spatial covariance has to be considered when using the t test in the sense of a local test approach within a gridded field, for example. Nevertheless the t test is also used in this manner within this study, testing local null

hypothesis at each grid point. The t test used within the present study generally takes into account the effect of serial correlation by reducing the sample size (using the effective sample size (cf. von Storch and Zwiers 1999) instead) and also the effect of inequality of the variances of $\mathbf{X}$ and $\mathbf{Y}$. For a detailed description of the t test and the problems encountered in practical use with climate data, see von Storch and Zwiers (1999). A further note of caution in applying the t test may arise from the fact that a large sample may indicate a statistical significance in difference of mean that is not "physically" significant. With increasing sample size n the detected difference of mean at a given level of reliability goes to zero as $n^{-1/2}$ (von Storch and Zwiers 1988). Taking into account the tendency of the test statistics to obtain significant differences in the mean, shorter sub-samples were also analysed to get an insight of the stability and robustness of the observed differences.

Unless noted otherwise, all tests of equality of means that are performed in this study are done by applying a two-sided t test.

Kolmogorov-Smirnov test

To test the goodness-of-fit of two distributions, the Kolmogorov-Smirnov test is applied. The Kolmogorov-Smirnov test compares an empirical distribution function $\hat{F}_X(x)$ with a specified distribution F_Y by measuring the distance between those two distributions (von Storch and Zwiers 1999):

$$\mathrm{D}_{KS} = \max_x |\hat{F}_X(x) - F_Y(x)|. \tag{3.5}$$

A large D_{KS} indicates an inconsistency between the data and the specified distribution.

Within this thesis the Kolmogorov-Smirnov test is used to compare the distribution of two data sets from experimental results against each other. Therefore a two sample Kolmogorov-Smirnov distribution test is performed. The data consists of two independent samples $\mathbf{X}$ and $\mathbf{Y}$ with size n_x $(x_1, x_2, \ldots, x_{n_x})$ and size n_y $(y_1, y_2, \ldots, y_{n_y})$. $\hat{F}(x)$ and $\hat{G}(x)$ represent the respective, unknown, distribution functions of $\mathbf{X}$ and $\mathbf{Y}$. $S_X(x)$ and $S_Y(x)$ denote the values of the cumulative distributions functions of $\mathbf{X}$ and $\mathbf{Y}$ at point x. The Kolmogorov-Smirnov test then provides a test of the null hypothesis $\mathrm{H}_0 : F(x) = G(x)$ against the following hypotheses:
(i) $\mathrm{H}_1 : \hat{F}(x) \neq \hat{G}(x)$
(ii) $\mathrm{H}_2 : \hat{F}(x) > \hat{G}(x)$. In a practical sense this means that $S_X(x)$ tends to be larger than $S_Y(x)$.
(iii) $\mathrm{H}_3 : \hat{F}(x) < \hat{G}(x)$.

The test returns the test statistic D (or D^+ or D^-) and a corresponding standardised statistic $Z = \sqrt{(n_1 + n_2)/(n_1\, n_2)} \cdot D$ (or D^+ or D^-) depending on the choice of the alternative hypothesis specified. D (Z) measures the (standardised) largest deviation

between the two samples.
For H_1: $D = \max\{S_1(x) - S_2(x)\}$,
for H_2: $D^+ = \max\{S_1(x) - S_2(x), 0\}$,
and for H_3: $D^- = \max\{S_2(x) - S_1(x), 0\}$.
The probability P, under the null hypothesis, of obtaining a value of the test statistic D (or D^+ or D^-) as extreme as that observed is computed using an approximation suggested by Kim and Jennrich (1973).

EOF-Analysis

The mean state of the climate system is a fundamental statistical parameter, but the mean state is not a typical state (von Storch and Zwiers 1999). This becomes clear if multi-annual monthly means of the upper troposphere geopotential height or the T_{2m} are examined, for example. The long-term mean fields of these variables show a more or less polar symmetric pattern (with deviations according to land-sea contrast and orography). Local particularly low or high values do not occur in the long-term mean as they are smoothed out by averaging over time. In addition, the spatial variability of the long-term mean field is much lower than that of the individual month. Thus it is very unlikely to detect the same pattern as the long-term mean pattern within a particular month. Therefore the long-term mean state is a rare event (von Storch and Zwiers 1999). The EOF analysis (Empirical Orthogonal Function analysis) provides an insight – to a limited extent – into the situation of a particular month.

A data field (given by the vector $\vec{\mathbf{X}}(t)$) may be separated into a field consisting of the signal and a field of noise (e.g. von Storch and Frankignoul 1998):

$$\vec{\mathbf{X}}(t) = \vec{\mathbf{X}}^s(t) + \vec{\mathbf{X}}^n(t) \tag{3.6}$$

The signal may be expressed if only a few (K) characteristic patterns $\vec{p}^k$ are used. In the case of an EOF analysis the characteristic patterns $\vec{p}^k$ are orthogonal, called EOFs (empirical orthogonal functions) $\vec{e}^k$:

$$\vec{\mathbf{X}}^s(t) = \sum_{k=1}^{K} \alpha_k(t)\vec{e}^k \tag{3.7}$$

The EOF coefficients (or principal components) are given as the scalar product of $\vec{\mathbf{X}}(t)$ with $\vec{e}^k$:

$$\vec{\alpha}_k(t) = \langle \vec{\mathbf{X}}(t), \vec{e}^k \rangle \tag{3.8}$$

A prominent example for an EOF coefficient is the time series of the Arctic Oscillation (AO) index.

For further information about the EOF analysis refer to von Storch and Zwiers (1999).

Chapter 4

Control integrations: Fast response of the NH cryosphere and circulation

To study the influence of surface cryospheric albedo changes in an early state (within the first 10 years after the application of a changed albedo parameterisation) and therefore the transient response of the climate system, three additional runs were performed (SC1_O, SC1_NA, and SC2_NA). These runs were forced with the same constant external forcing conditions as the CTRL_O and CTRL_NA runs, but were started from different initial conditions. The SC1_NA and SC1_O runs, the SC2_NA run and the respective period from the CTRL_O run, and the first decade from the CTRL_NA and CTRL_O runs build the 6-member ensemble consisting of 3 paired runs.

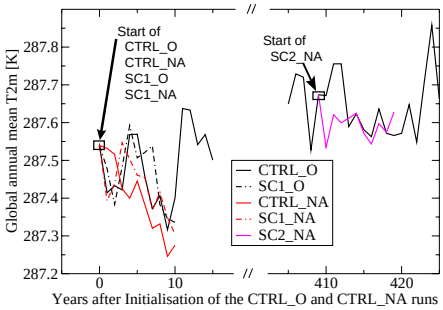

Figure 4.1: Global mean temperature of the initial runs. The CTRL_NA and CTRL_O runs were started in the year 1990 as successors of the HIST & B2 run.

The initial conditions for these short runs were calculated / selected as follows: SC1 (ShortControl1) uses the same initial conditions as the CTRL runs for the ocean but different initial conditons for the atmosphere. SC2_NA started from the middle of the long-term CTRL_O run. Therefore changes within the SC2_NA run were compared to the adjoining period within the CTRL_O run. Unless noted otherwise the differences described in this chapter arise from the mean difference of all 6 ensemble runs (3 runs each with new ("NA") and old albedo ("O") scheme, respectively). Figure 4.1 gives an overview over the start time of the initial response ensemble runs.

4.1 Snow and sea ice

Under identical surface temperature conditions and identical downward solar radiation at the surface, the new snow albedo parameterisation generally leads to a decrease of absorbed solar radiation. Therefore a fast response in terms of a lengthening of the snow cover season and a corresponding decrease in T_{2m} is expected, especially in areas with few forests, because the difference between new and old albedo scheme increases linearly as the forest fraction decreases. A similar impact on the sea ice cover is expected as the new parameterisation scheme leads to less absorbed solar radiation, as was demonstrated for central Arctic SHEBA experiment conditions in 1997 by Køltzow et al. (2003) (table 3.2).

To determine the total area covered by snow a very simple assumption was applied. Each grid cell with a snow water equivalent > 0 cm was assumed to be covered completely with snow which is a common approach (Brown 2000). Based on daily computation of the integrated area of snow cover the monthly means are obtained. The snow cover shows the expected fast reaction to the generally higher albedo by an increase of seasonal mean snow covered area in the NH explicitly for summer. Whereas there is a slight tendency towards more snow in spring and autumn when the snow albedo is changed, no differences in winter snow cover, distinguishable from natural interannual variability, occur (Figure 4.2). The statistically significant differences in summer (at the 1 % significance level), which stem almost exclusively from the great differences in June, can be explained simply by the sunshine duration in summer (leading to a large amount of solar radiation reaching the surface), by the location of the remaining snow (in the high Arctic), and by the temperatures in summer that lie around or above freezing point. If the snow surface temperature is far below freezing point, as mostly occurs in winter over large areas of Eurasia and North America that are covered with snow, a slightly changed albedo would not have any impact on the onset of the snowmelt. The snow would be simply too cold to melt. Therefore the snow albedo feedback mechanism will not play a major part in directly (thermodynamically) inducing local changes in central and north Eurasia and North America snow cover in the cold continental winters. In summer the situation is quite different. The summer snow occurs predominantly in non-forested mountain regions and in the (also non-forested) tundra, where the effect of the new snow albedo scheme can be seen most pronouncedly (cf. Figure 3.6) as for the forest cover fraction of each grid cell the old scheme is used.

The NH sea ice volume increases remarkably fast after the sea ice surface has attained a different albedo, indicating a strong thermodynamic influence on the sea ice growth and melting. This is in accordance with the findings of Lemke et al. (2000), who noticed in a model study a radiative induced increase of the sea ice volume, even without additional effects from surface wind changes. The rapid increase in sea ice volume occurs very similarly in all ensemble realisations, regardless of the initial conditions of sea ice, ocean, and atmosphere (Figure 4.3). The increase is maximum during summer, when the SAF

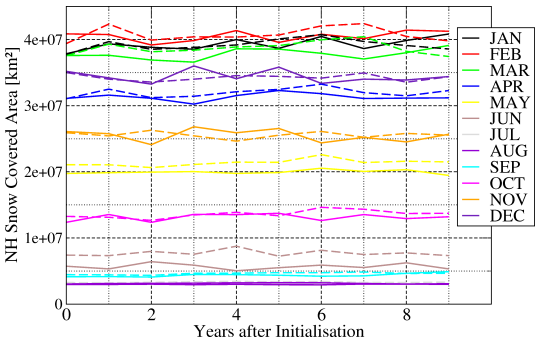

Figure 4.2: Ensemble mean monthly means of initial evolution of NH snow covered area. The solid lines refer to the results of the old albedo scheme runs, the dashed lines to the results of the new albedo scheme runs. Note the large differences in May and especially in June.

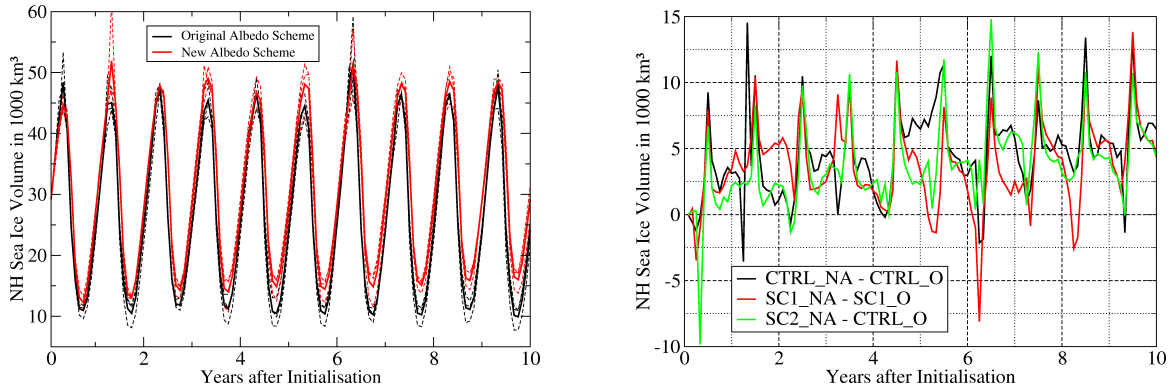

Figure 4.3: Initial evolution of NH sea ice volume. Left: solid lines denote monthly means of the three respective ensemble members, dashed lines denote the monthly mean sea ice volume in each individual experiment. Right: monthly mean differences of the three individual paired runs, new scheme minus old scheme.

plays a dominant role, as then actual solar radiation is available for surface absorption. These findings point to the conclusion that the thermodynamical response on a local scale causes local differences in sea ice cover and thickness, without the influence of the atmospheric circulation, at least for the summer sea ice thickness and concentration. Within just approx. 4 years a new equilibrium state in yearly maximum and minimum NH sea ice volume is reached (Figure 4.3). The ensemble mean annual mean NH sea ice volume also increased by more than twice the standard deviation of long-term annual mean NH sea ice volume ($\sigma = 1.36 \cdot 10^3\,\mathrm{km}^3$) after 2 years of integration (approx. 3 times after 3 years) (not shown). Figure 4.3 also shows that maximum differences in NH sea ice volume take place in summer from the first year on, whereas the differences within all other seasons are much smaller than in summer.

The NH sea ice cover does not show the same uniform behaviour as the NH sea ice volume. Instead, an increase in NH sea ice cover occurs almost exclusively in summer and autumn. Figure 4.4 shows the differences in March, where changes are visible within a dipole pattern (more sea ice in Labrador Sea / less in Barents Sea and more

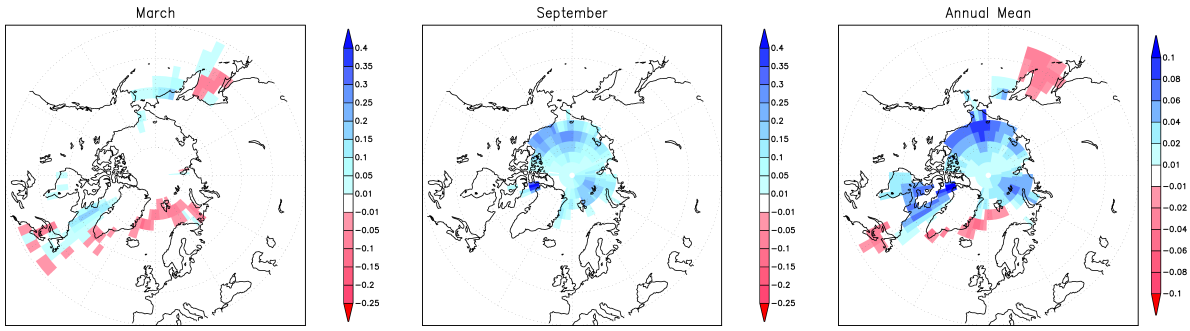

Figure 4.4: Difference in NH fractional sea ice cover (first 10 years) of ensemble mean for March (left), September (middle), and for the annual mean (right). Note the decreased differences between maximum and minimum values for the annual mean compared to the individual months as indicated in the legends.

in Bering Sea / less in Okhotsk Sea), and in September, where within the Pan-Arctic domain the sea ice cover increases. September and March are chosen, as these months stand for minimum and maximum sea ice cover, respectively, at least in ECHO-G. The dipole pattern in the March sea ice differences in Figure 4.4 are strikingly similar to the regression maps pattern, when sea ice concentration anomalies from observations are regressed on the observational AO index as done by Liu et al. (2004) (cf. Figure 2.7). They are also similar to the leading EOF pattern of winter sea ice anomalies, whose corresponding times series is highly correlated with the AO index (Deser et al. 2000). This would lead to the explanation that AO-like circulation differences between the runs with new and old albedo scheme may be responsible for the sea ice concentration differences. As there is more ice in Baffin Bay and the Labrador Sea during high winter AO index phases, it could be hypothesised that also the AO index is increased. However, this is not the case, as will be shown in section 4.2. The increase of summer sea ice concentration is caused directly by less absorbed solar radiation in spring and summer. This leads to an increase in sea ice thickness and volume. The late summer and early autumn ice consists of multi-year ice. A higher albedo during spring and early summer decreases sea ice melting rates, leading to more sea ice in late summer, because more perennial sea ice survives.

4.2 Temperature and circulation

In accordance with the findings of the previous section, less absorbed solar radiation leads to a cooling of the northern part of the NH. Once (within the annual cycle) the snow or the sea ice is gone, much more solar radiation is absorbed by the much darker soil or vegetation or the open ocean water. Furthermore, the open ocean water provides an additional heat source for the atmosphere by releasing latent and sensible heat to the atmosphere. Additionally, large areas of the NH are covered with snow in winter and the changed albedo instantly reduces the absorbed solar radiation over non completely forested areas that are covered with snow. Obviously, this feedback mechanism operates very rapidly. Therefore the temperature in the Arctic drops fairly promptly (in terms

of monthly means) when the albedo is altered. The ensemble mean annual mean Arctic (NH) T_{2m} averaged over the initial 10 years yield a decrease of -0.50 K (-0.05 K) (Figure 4.5) that is statistically significant at the 5 % (5 %) level. Due to the high internal variability of the Arctic climate an ensemble of 3 paired runs is too small to capture the initial temperature drop. A guess from a linear regression analysis based on monthly mean temperature difference yields an initial drop of -0.42 K accompanied by a following gradual decrease of -0.16 K/10 years (-0.01 K and -0.08 K/10 years for the whole NH) (Figure 4.5). Figure 4.5 also shows the initial evolution of the ensemble mean difference in central Arctic (north of 78° N) to equator T_{2m} contrast. In general, the equator to pole temperature gradient increases for all seasons, but not uniformly for all years and all seasons, respectively, due to the very high natural variability of a small domain in the central Arctic (approx. $1.4 \cdot 10^6\,\mathrm{km}^2$ around the North Pole).

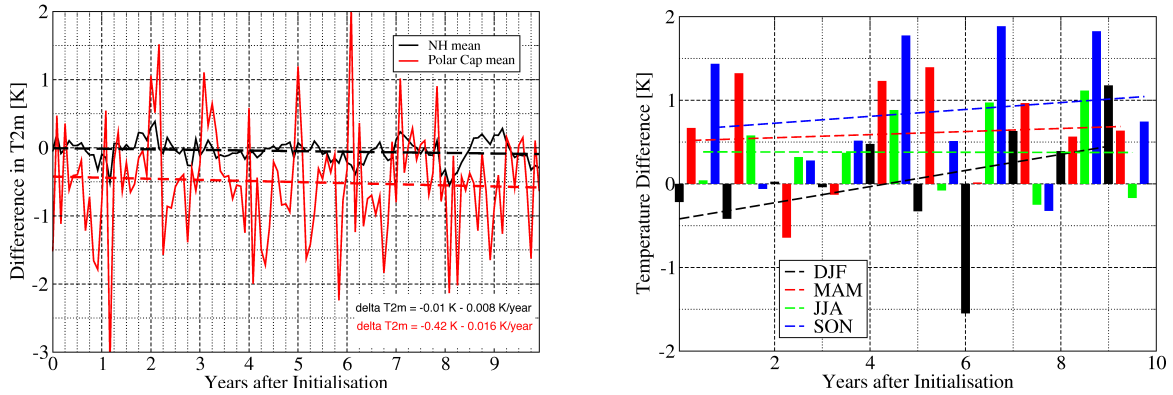

Figure 4.5: Initial evolution of ensemble mean NH and Arctic T_{2m}. Left: black lines denote NH monthly mean T_{2m}, red line denotes Arctic monthly mean T_{2m}, hatched lines denote respective regression lines. Right: differences of seasonal mean T_{2m} difference between the central Arctic (north of 78° N) and the equator, hatched lines denote respective regression lines. Positive values denote an increase in equator to pole temperature gradient.

To identify the change in the AO phase between the paired runs, the annual mean and DJF mean SLP anomalies with respect to the respective means of the long CTRL_O run are projected onto the annual and DJF AO pattern of the CTRL_O run. In the simulations with the new albedo scheme the mean of the standardised AO indices change from $+0.24$ to -0.11 for DJF and from -0.08 to -0.01 for the annual AO index. The finding for the DJF AOI is in contradiction to the sign of the changes in the March sea ice cover displayed in Figure 4.4, assuming that changes of the phase of the NAO and the AO were the only causes of sea ice cover changes in the North Atlantic region.

Figure 4.6 shows the initial evolution of the zonal mean geopotential height in March. This month was chosen because within the long-term response (cf. Figure 5.22) in March maximum differences in zonal wind speed occur. The initial response of the climate system in terms of deflection of the geopotential height is either not physically consistent with the long-term mean deflection or the averaging period and the number

of individual ensemble members is simply too small. No clear impression of the direction of the changed mean state of the NH circulation can be obtained from Figure 4.6. On the other hand, the picture in the Southern Hemisphere (SH) is much more consistent, between each paired realisation of the ensemble runs as well as compared to long-term mean integrations (Figure 5.24). Common features of all paired realisations are the local minimum in geopotential height change at around 50° S and the weakening of the Antarctic polar vortex (indicated by the rise of the geopotential height south of around 60° S throughout all selected levels).

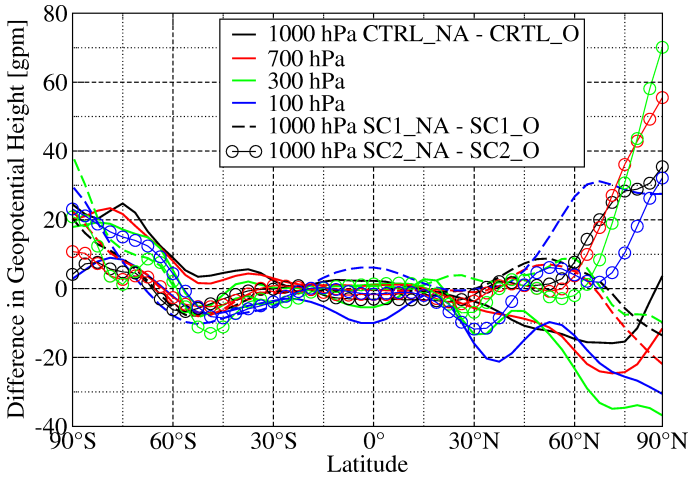

Figure 4.6: Differences in March zonal mean geopotential height, averaged over the first 10 years of the respective control simulations. Colours indicate pressure level, line shape (solid, dashed, thin solid with circles) indicate the respective experiment.

Chapter 5

Control integrations: Long-term response of the NH cryosphere and circulation

The analysis of the long-term mean responses of a changed radiation balance due to changes within the absorbed solar radiation over NH snow and sea ice areas starts with the impact on the snow and sea ice itself. The analysis disregards the first 110 years of the simulation to reduce effects arising from climate conditions that have not reached a new equilibrium state.

In chapter 4 dealing with fast responses to changed radiation conditions it was shown that the cryosphere reacts very fast to changed surface albedo and temperature conditions. The analysis of the long-term response focuses on the changed equilibrium state and is also based on a broader basis of data, as the analysed time span covers 400 years.

5.1 Sea ice and snow

5.1.1 Snow

As in the initial response, the snow covered area in the NH increased when the new albedo scheme was applied. Generally in all seasons the snow cover duration increased (Figure 5.1). Greatest differences in the snow cover duration occur in spring and summer with a particular maximum over the south western edge of the Tibetan plateau and – even more – in the Kashmir region in summer. An explanation for the Kashmir outlier is given by the combination of a low percentage of forest cover, the high amount of solar radiation already in winter, and the large amplitude in the diurnal cycle of T_{2m}. The large diurnal temperature amplitude increases the probability of a snow surface temperature above $-10\,°C$. At snow surface temperatures above $-10\,°C$ the new albedo scheme has

higher values, thus the snow surface absorbs less solar radiation compared to a darker snow surface. As a consequence, the probability of an onset of snow surface melting during a diurnal cycle is reduced, or at least the onset is delayed. The large amount of incoming solar radiation in low latitudes even in boreal winter leads, in combination with a changed albedo, to large differences in absorbed solar radiation at the snow surface. Under the set-up conditions of the experiment concerning the different snow albedo schemes, this combination leads to the described maximum differences. The snow melt in the Arctic is not prolongated as much as in Kashmir for the following reasons: 1. Except for the Tundra the forest cover within the snow covered area minimises the effect of a changed snow albedo. 2. For astronomical reasons, in Kashmir the insolation does not reach as low values in winter as in the Arctic, thus causing changes in absorbed radiation to set in early. This effect is amplified by less cloud cover over Kashmir compared to the Arctic. Because of the strong snow albedo feedback effect, the smaller annual cycle of solar radiation and surface temperature compared to the Arctic, the snow cover duration increased extraordinarily for Kashmir climate conditions in the CTRL_NA simulation.

Snow cover duration changes within the Arctic region are maximum in June in the northeastern Siberian Tundra (not shown). In the Arctic the largest impacts of the snow surface temperature depending albedo scheme occur where only a small fraction of the surface is covered by forest and especially in the northernmost areas of the NH continents in early summer. In contrast to Kashmir seasonal mean maximum snow cover changes in the Arctic do not exceed 9 days (in the Ural region in spring and northern Alaska and northeastern Siberia in summer). Due to the strong feedback effect between temperature and snow cover, the prolongation of seasonal snow cover (Figure 5.1) occurs in those areas with a decreased surface air temperature (Figure 5.15) and vice versa. In contrast to the changes in sea ice cover and volume, the changes in the snow cover are explainable solely as a reaction to local changes in absorbed solar radiation. Due to the strong snow-temperature-albedo feedback effect and the rapidness of snow melt, just a few $\mathrm{W\,m^{-2}}$ difference in absorbed solar radiation may start a melting event. Once the snow has gone, bare soil with a much lower albedo is present, increasing the additional amount of absorbed solar radiation. This explanation is also strengthened by the results of the initial snow cover evolution after the albedo changes were applied (Figure 4.2). The ensemble mean NH mean changes in snow covered area in May and June (Figure 4.2) clearly indicate the dominant role of the absorbed radiation. Due to astronomical reasons, in May and June much solar radiation reaches the NH. In contrast to July and August, in May and June large areas are still covered with snow.

The impact of snow cover changes on temperature distribution and circulation is discussed in section 5.4.

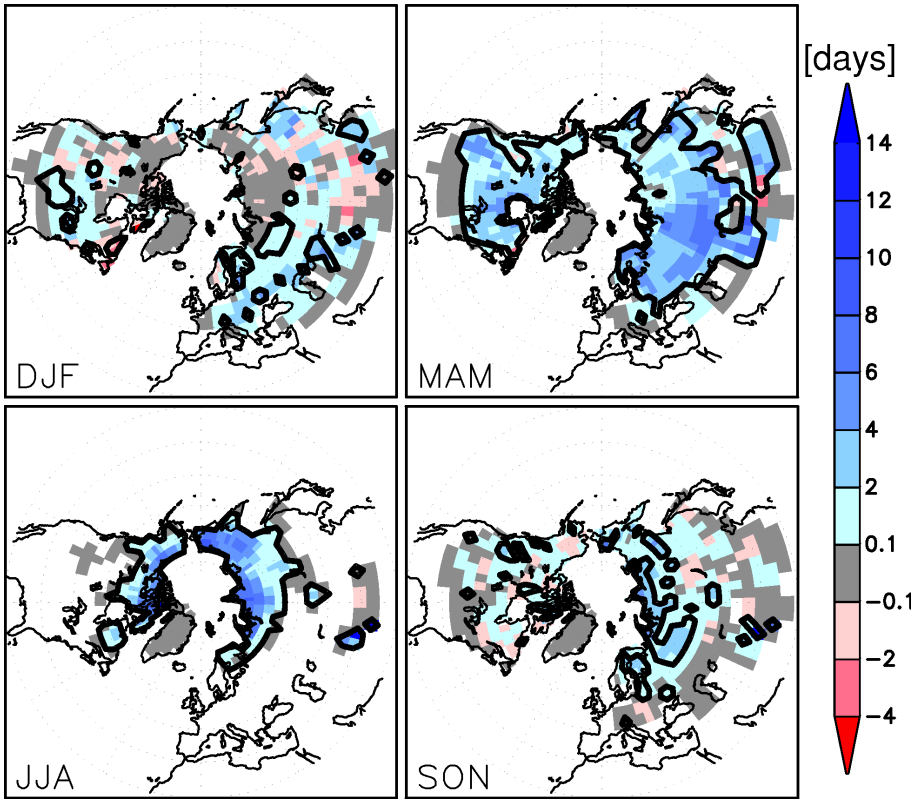

Figure 5.1: Seasonal mean differences of NH snow cover duration (CTRL_NA - CTRL_O). Thick black lines enclose areas with differences that are statistically different at the 5 % level of significance.

5.1.2 Sea ice

The long-term mean differences in the NH sea ice characteristics are distinct from those that arise in the initial state discussed in chapter 4, especially during winter and spring around Greenland.

The ensemble mean of short runs showed differences in sea ice cover (Figure 4.4) which are very similar to those patterns that are produced when satellite data derived sea ice concentrations are regressed on the NAO index (cf. Deser et al. 2000, Liu et al. 2004). The difference pattern between the CTRL_NA and the CTRL_O run does not show a dipole pattern in sea ice cover between the Davis Strait and Denmark Strait. Instead, in all seasons and all seas around Greenland south of approx. 75° N the sea ice cover is reduced (Figure 5.2). On the other hand, the pattern of Figure 5.2 is consistent with the regression pattern of Figure 5.3. This Figure shows that the negative phase of the AO accounts for a decrease of sea ice cover in all seas around Greenland south of approx. 75° N and in the Labrador Sea and an increase in the Hudson Bay and the Barents Sea ice coverage.

The differences in the long-term mean sea ice cover in winter and spring around southern Greenland reflect the occurrence of high sea ice cover events on a local scale as

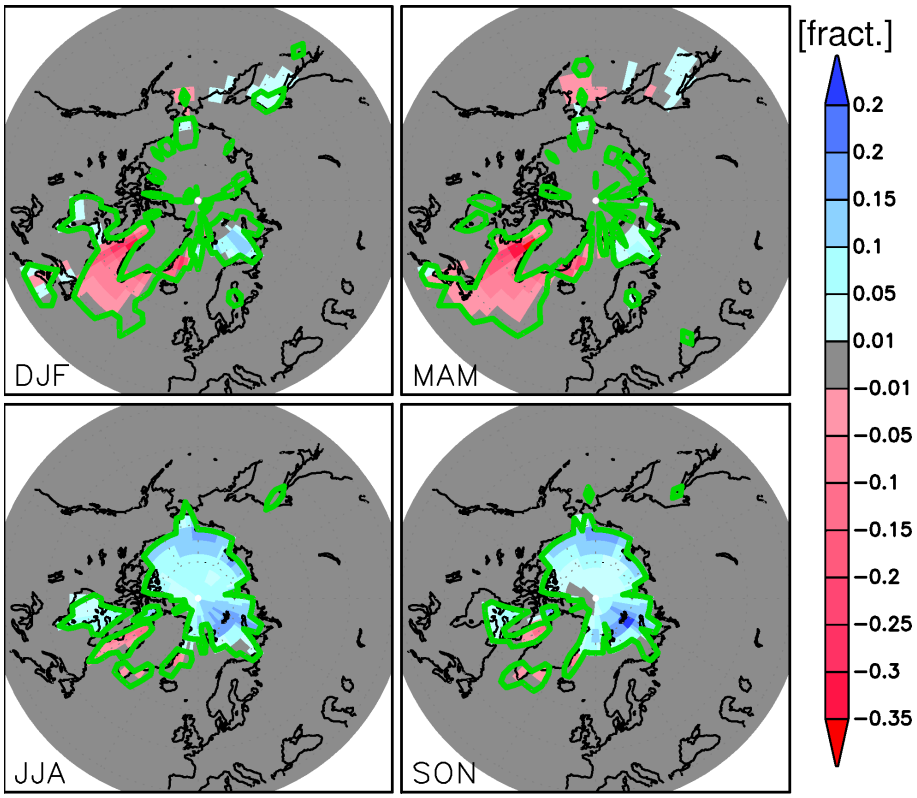

Figure 5.2: Seasonal mean differences of NH fractional sea ice cover (CTRL_NA - CTRL_O). Thick green lines enclose areas with differences that are statistically different at the 5 % level of significance.

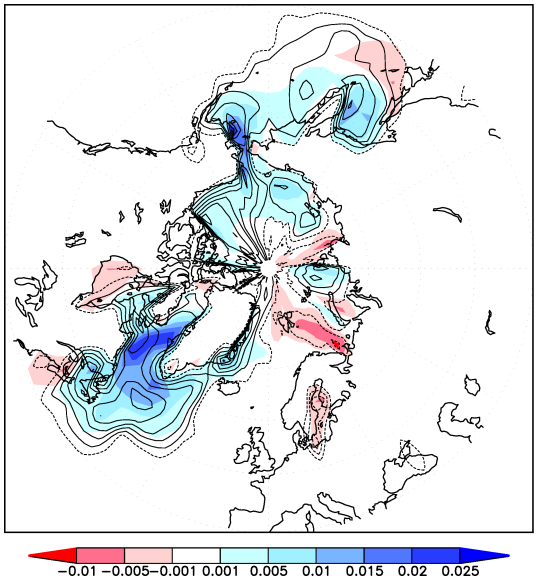

Figure 5.3: Regression and correlation map (sea ice concentration and AO indices of the CTRL_O run). Shaded areas denote monthly mean anomalies of fractional sea ice concentration regressed on the standardised monthly mean AO indices, contour lines denote the correlation between the standardised monthly mean AO indices and the monthly mean sea ice concentrations anomalies. Solid contour lines indicate a positive correlation, dashed contour lines a negative correlation. Contour line interval is 0.03.

demonstrated exemplarily for the fractional sea ice cover in the central Labrador Sea in March (Figure 5.4). In the CTRL_O run a high phase of sea ice cover around Greenland occurs much more frequently. For instance, in March the completely central Labrador Sea lies within the sea ice edge in 5 out of 10 cases in the CTRL_O run (not shown). In the CTRL_NA run this is reduced to 1 out of 10 cases (not shown). In spite of the slight warming trend (cf. Figure 3.3), no systematic reduction of the marginal sea ice area occurs during the maximum NH sea ice extent for each of the control integrations (Figure 5.4).

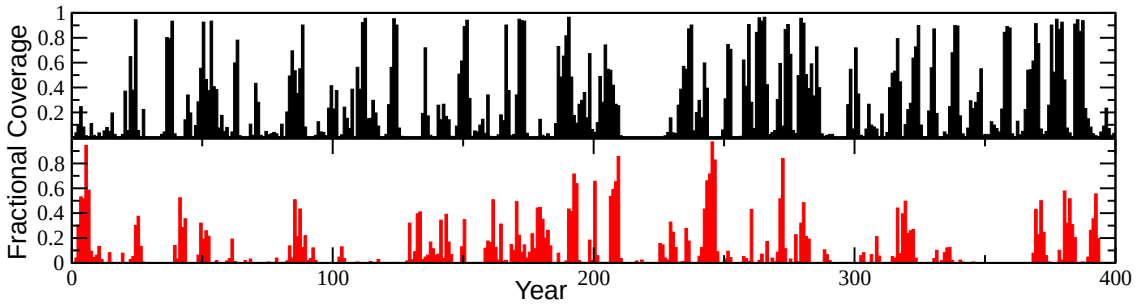

Figure 5.4: Central Labrador Sea ($56-48°$ W, $56-60°$ N) fractional sea ice coverage in March, black: CTRL_O run, red: CTRL_NA run.

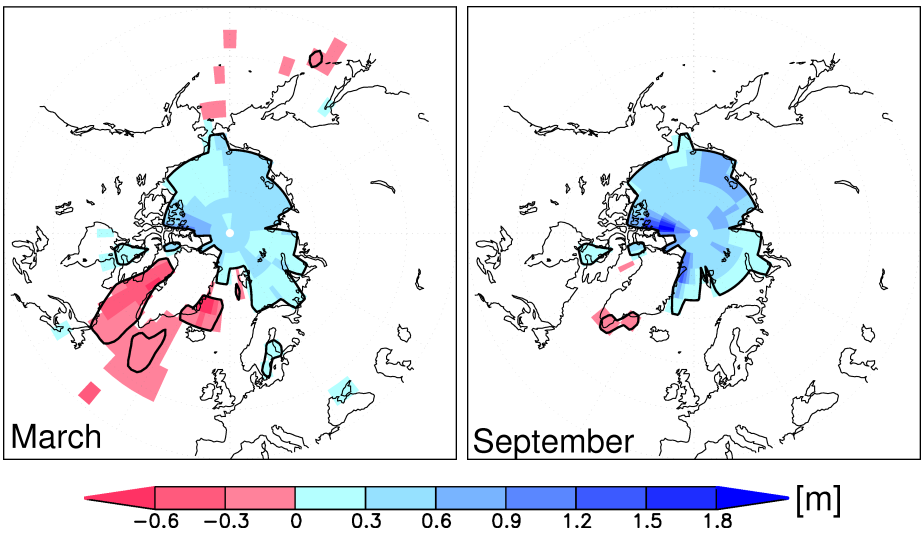

Figure 5.5: March and September mean differences of NH sea ice thickness (CTRL_NA - CTRL_O). Only differences that are statistically different at the 10 % significance level are shown. Thick black lines enclose areas with differences that are statistically different at the 1 % level of significance.

An explanation for the reduced sea ice cover around southern Greenland in the CTRL_NA run may be given by the reduced sea ice export through the Fram Strait. An increase in SLP over the Nordic Seas is accompanied by a smaller increase in SLP over the Chukchi Sea (Figure 5.20). As a result the transpolar drift of sea ice is reduced. Another contributing explanation may be given by the decreased AO and NAO indices in the

CTRL_NA run (cf. section 5.4). A shift towards a lower polarity of the AO leads to reduced advection of cold air masses from the high Arctic to the Davis Strait and Labrador Sea region, thus increasing the near surface air temperatures there. The reasons which may have caused this regime shift towards a lower polarity will be discussed in the subsequent sections 5.2 to 5.4 within this chapter.

A direct thermodynamic effect as a reason for the reduced sea ice is unlikely because the new scheme leads to a reduction of absorbed radiation, at least as long as no melt ponds occur. The increase in sea ice thickness at the northern boundary of the Canadian Archipelago (Figure 5.5) shows that as a response to perturbed radiative conditions the sea ice thickens most where it is initially thickest, which is in agreement with the findings of Bitz and Roe (2004). As demonstrated above, the effect of the different albedo parameterisations on the sea ice thickness (Figure 5.5), the albedo itself (Figure 5.8), and the absorbed solar radiation (Figure 5.10) is even larger than could be expected from the annual mean difference in absorbed radiation under constant SHEBA (Uttal et al. 2002) conditions (cf. Table 3.2). This happens because in spring the new scheme leads to a decrease in absorbed solar radiation, thus delaying the start of the melting season. Due to the strong feedback effect, more and thicker sea ice is present in summer and also survives the summer (Figure 5.5). Hence the differences in albedo are further increased, even if parameterised melt ponds occur. Sea ice – even with melt ponds – still has a much higher albedo than the open ocean water surface. Furthermore, the sea ice cover in the Sea of Okhotsk is increased in the CTRL_NA run. The Sea of Okhotsk is located in latitudes even lower than for the Greenland region. Thus the sea ice reduction in the Greenland region cannot be attributed as linear to a changed sea ice albedo.

In a model study Koenigk et al. (2006) showed that 2 years after a positive anomaly of sea ice export through the Fram Strait, the sea ice thickness in the Davis Strait and the Labrador Sea is increased. This also leads to an anomaly pattern in the T_{2m} in the Labrador Sea and Davis Strait region similar to Figure 5.15. The interannual variability of the Fram Strait sea ice export is dominated by the annual mean SLP gradient across the Fram Strait which explains more than 80 % of the variability (Vinje 2001b and Hilmer et al. 1998). Figure 5.20 indicates an increase in SLP from west to east across the Fram Strait in the CTRL_NA run that leads to a decrease of sea ice export. An explanation for the decreased sea ice coverage and thickness in the Davis Strait and Labrador could therefore be given by the increase in SLP over the Svalbard region, leading to a reduced amount of sea ice export through the Fram Strait. An objection to this suggestion may arise from the importance of the sea ice thickness for the ice export (Arfeuille et al. 2000). The sea ice thickness and volume is increased in the CTRL_NA run (Figure 5.5). Thus the sea ice volume in the Arctic is not the limiting factor for the reduced ice export in the CTRL_NA run, compared to the CTRL_O run. Nevertheless, the SLP gradient across the Fram Strait obviously dominates the ice export. In model simulations no correlation between ice export and NAO have been found (Koenigk et al. 2006 and

references therein). Koenigk et al. (2006) concluded from their findings that increased ice export leads to a cooling and freshening of the Labrador Sea, with the reduction of the deep oceanic convection as a consequence. The reduced convection preserves the salt and temperature anomaly of the Labrador Sea, thus leading to increased sea ice cover. Koenigk et al. (2006) showed further that low sea ice exports show symmetric results for the entire process described above. This may explain the low amount of sea ice in the Labrador Sea in the CTRL_NA run, as the differences in SLP between the CTRL_NA and the CTRL_O run favour a low amount of sea ice export. Having said that, a statistically significant difference in sea ice concentration and in sea water temperature and salinity in the top layer of the central Labrador Sea ($56 - 48°$ W, $56 - 60°$ N) should occur between the CTRL_NA run and the CTRL_O run, if the mechanism described above were also responsible for the differences between the CTRL_NA run and the CTRL_O run. Instead, despite the decrease in sea ice cover in the East Greenland Current and the warmer near surface ocean water around Greenland, the Labrador Sea near surface water does not show statistically significant differences in temperature and salinity between the CTRL_NA and the CTRL_O simulation (not shown).

An important difference to the study of Koenigk et al. (2006) has to be pointed out. Their results stem from periodically occurring sea ice export anomalies or – as done in a sensitivity experiment – prescribed export anomalies. Within a lag of 2–3 years after a positive export anomaly ($+\,3000$ km^3 sea ice added to the East Greenland Current) the Koenigk et al. (2006) study showed a positive anomaly in annual mean SLP for the North Atlantic and parts of Europe while there is a negative anomaly for the Nordic Seas. The situation in the present study is almost completely the opposite. In the long-term mean, both the reduced sea ice export and the negative SLP anomaly for the North Atlantic and parts of Europe occur. In terms of anomaly patterns of T_{2m} and SLP the long-term mean differences between the CTRL_NA and the CTRL_O run resemble the anomaly pattern that occur with a lag of approx. 2 years after the Fram Strait sea ice export anomalies, as described by Koenigk et al. (2006).

To draw a conclusion from the above, the NH sea ice does not show a linear response to the altered albedo conditions. Instead, the atmospheric circulation plays a dominant role in modifying the sea ice cover distribution.

As a hemispheric mean the annual cycle of sea ice area and extent is reduced (Figure 5.6). Due to the reduced sea ice cover around Greenland the maximum total area is reduced. As a result of the thicker ice in the Arctic Ocean more sea ice survives the summer, thus covering a larger area. The reduced amplitude of the annual cycle matches observation data much better. Cavalieri et al. (2003) reported as 1979 to 1999 mean values for the NH sea ice extent a minimum of $6.9 \cdot 10^6$ km^2 and a maximum of $15.3 \cdot 10^6$ km^2.

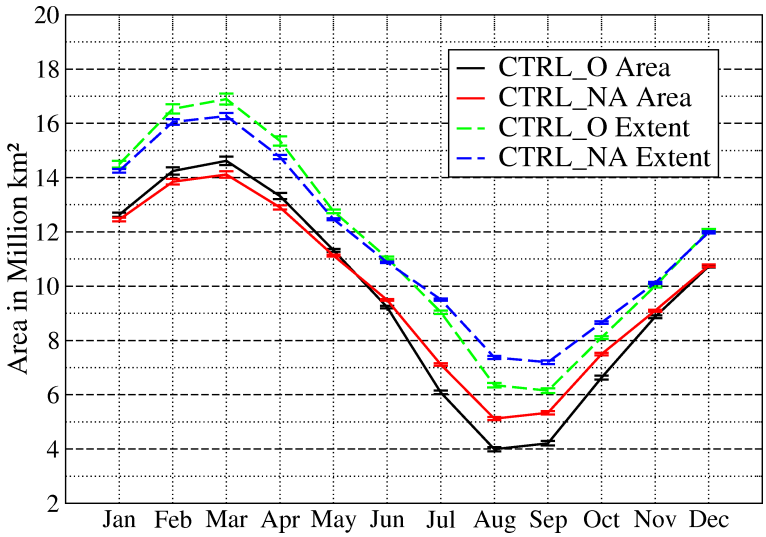

Figure 5.6: Annual cycle of NH sea ice extent (solid lines) and area (dashed lines). Original albedo scheme run black (area) and green (extent), new albedo scheme run red (area) and blue (extent). Error bars denote the 95 % confidence interval of the monthly mean values, taking into account the effective sample size.

Heat flux from the ocean to the atmosphere

Around Greenland an enormous difference between the CTRL_NA and the CTRL_O run in heat flux (sensible and latent) from the ocean to the atmosphere occurs. The heat flux differences are maximum in the Davis Strait, reaching monthly mean differences of up to 90 $\mathrm{W\,m^{-2}}$ (Figure 5.7). The increased heat flux from the ocean to the atmosphere in the Greenland region also impacts the atmospheric circulation and temperature distribution. This will be discussed in section 5.3 and section 5.4.

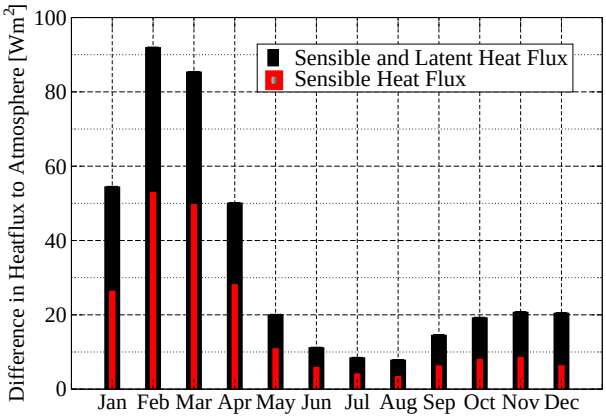

Figure 5.7: Annual cycle of the Davis Strait ($54-51°$ W, $60-64°$ N) heat flux difference (CTRL_NA - CTRL_O). Positive values indicate an increase in heat flux from the ocean surface to the atmosphere.

5.2 Radiation

Surface albedo

The effect of a changed snow and sea ice albedo parameterisation on the modelled surface albedo is self-evident. As described above, both snow and sea ice absorb less solar radiation if the new scheme is used, which generally results in an increase of snow cover duration and sea ice coverage (e.g. Figures 5.1, 5.2 and 5.6). Figure 5.8 shows in monthly resolution how regions of maximum differences in surface albedo move over the continents. In the transition from winter to summer they move within the extent of the snow covered area from the southern margin of the snow extent in winter to the margin of the remaining snow in July. Note that the largest differences occur over sparsely forested regions, either in the marginal zone of snow extent in winter and spring or – to an even larger extent – in the northernmost parts of Eurasia and North America in May and June. The continental surface albedo changes mainly reflect the prolonged occurrence of snow and also snow cover in regions that have a T_{2m} not always far below the freezing point. The differences in autumn are caused again by the snow cover.

The situation for the NH oceans is less uniform with respect to the sign of the difference. Throughout nearly the whole year the surface albedo over the sea areas around southern Greenland is decreased, reflecting the decreased mean sea ice cover in that region. Triggered by the SAF, the differences in surface albedo are predominantly a result of from the changed surface conditions, for instance thicker ice and a larger fractional coverage of sea ice in summer. The increased albedo from July to October actually stems from the increase in sea ice cover (Figure 5.2) and not from the albedo parameterisation itself. Instead, in summer the parameterised occurrence of melt ponds would actually lead to a lower surface reflectivity (cf. Table 3.2). Simply the increased coverage of sea ice increases the surface albedo of the Arctic Ocean in summer.

Statistically significant albedo changes around Antarctica occur although the surface temperature depending albedo of snow and sea ice has not been modified for the Southern Hemisphere (SH). These albedo differences reflect a changed sea ice cover in the SH Oceans arising from NH climate changes.

Planetary albedo and absorbed solar radiation

The shortwave surface albedo is nothing more than the ratio of reflected to incoming solar radiation reaching the surface. Without solar radiation reaching the earth's surface, an altered albedo does not have any effect on the surface energy budget. This explains why there is no effect on the absorbed solar radiation in boreal winter, whereas the effect is maximum from May to July (Figure 5.10).

Clouds are by far the most important part of the climate system to alter the amount of

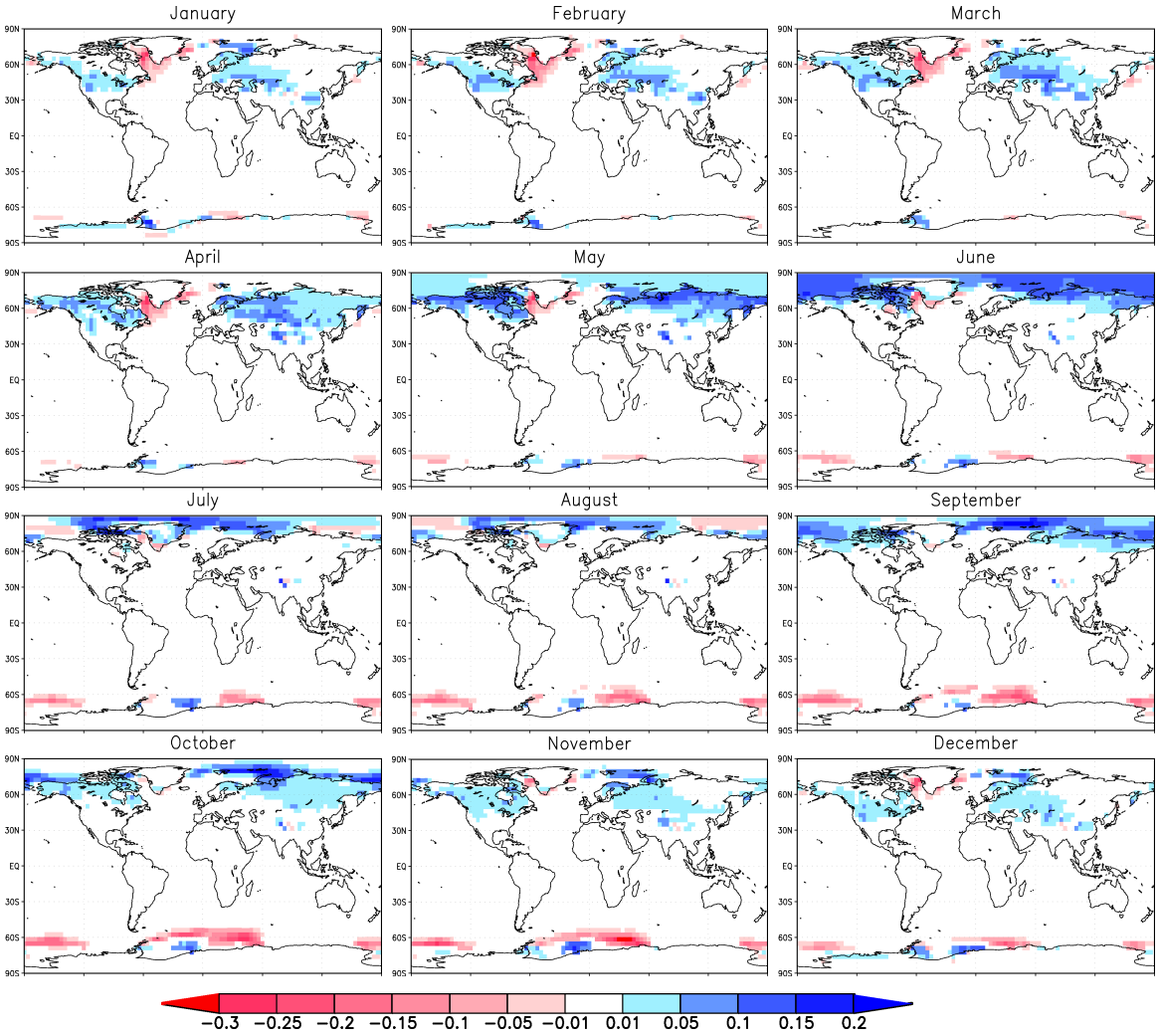

Figure 5.8: Differences in monthly mean surface albedo (CTRL_NA - CTRL_O). Only differences > 0.01 that are also statistically different at the 1 % level of significance are shown.

solar radiation reaching the ground and also to alter the planetary albedo. The patterns of planetary albedo changes (Figure 5.9), however, are similar to surface albedo changes (Figure 5.8). This indicates that surface albedo changes are transformed into planetary albedo changes regardless of the changes in cloud cover (Figure 5.14), which underpins the finding of Qu and Hall (2006). The sign of both planetary and surface albedo changes is identical for each region. Nevertheless, the planetary albedo changes are smaller compared to the changes in surface albedo. Due to decreased sea ice cover in the Davis Strait a large amount of latent heat is released into the atmosphere (Figure 5.7), leading to an increase in cloud cover in the Davis Strait from January to June (Figure 5.14). The surface albedo as well as the planetary albedo are decreased in that region. The opposite is the case for the central Arctic Ocean in June (Figures 5.8, 5.9 and 5.14). Here the increased sea ice cover (Figure 5.2) leads to a decrease in latent heat release and a decrease in T_{2m} (Figure 5.15) as well as an increase in SLP (Figure 5.20). All these changes favour a decrease in cloud cover, which consequently occurs (Figure 5.14).

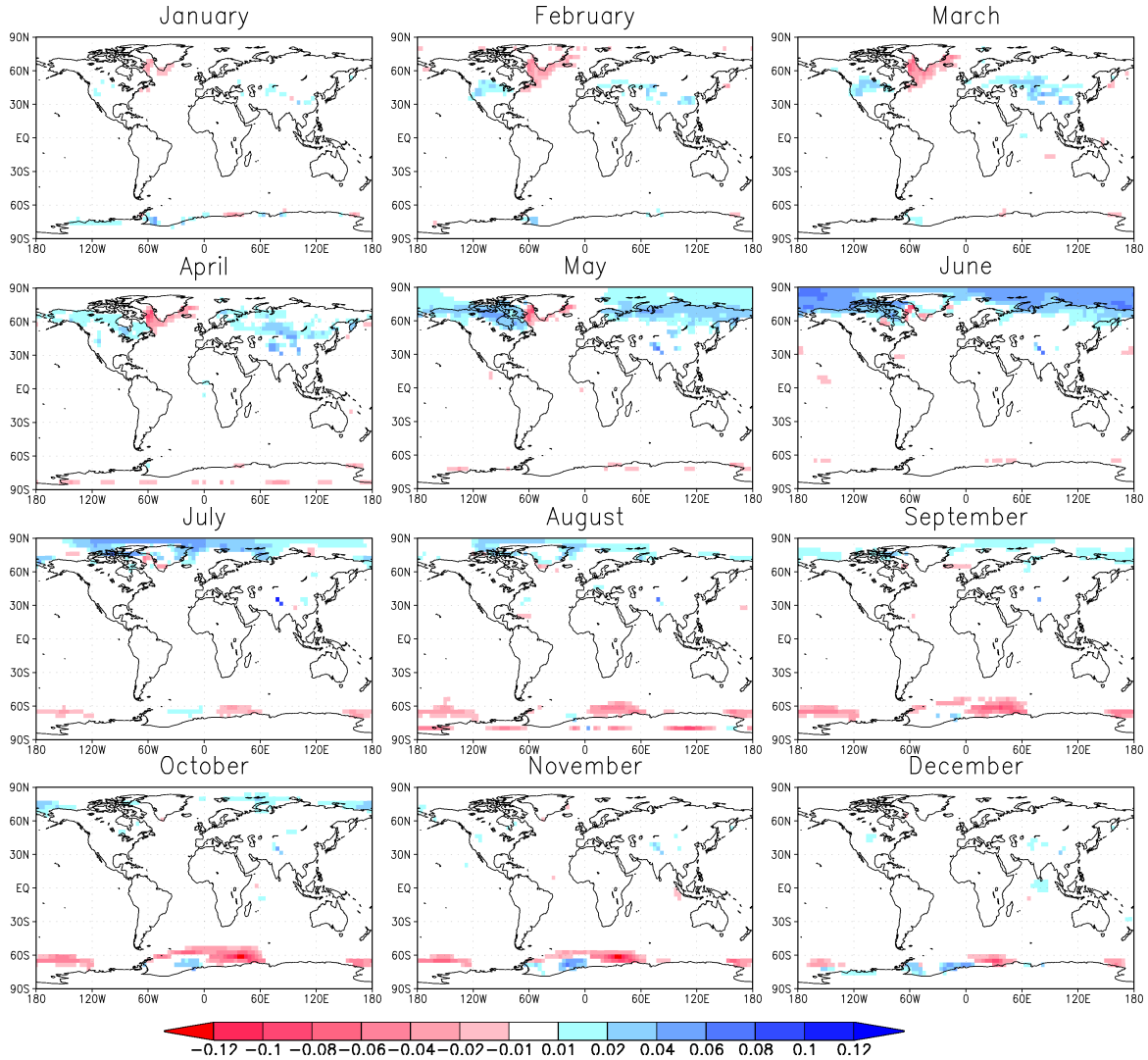

Figure 5.9: Differences in monthly mean planetary albedo (CTRL_NA - CTRL_O). Only differences > 0.01 that are also statistically different at the 1 % level of significance are shown.

The decreased surface and planetary albedo in the seas around southern Greenland lead to an increase in absorbed solar radiation (Figure 5.10) as well as in TOA net radiation budget (Figure 5.12). This means, that the energy lost in the uppermost ocean layer, which originates from the increased heat flux into the atmosphere due to decreased sea ice cover is partially compensated by the changes in the radiation budget. Thus not all of the extra amount of heat which is released in the Davis Strait and Labrador Sea from the ocean has to be transported by ocean currents or by the atmosphere into those regions.

Net TOA radiation

The already existing negative annual mean radiation budget at the top of the atmosphere (TOA) over the Arctic (Figure 5.11) becomes even more negative as a result of the increased planetary albedo over the Arctic. If less solar radiation is absorbed at the

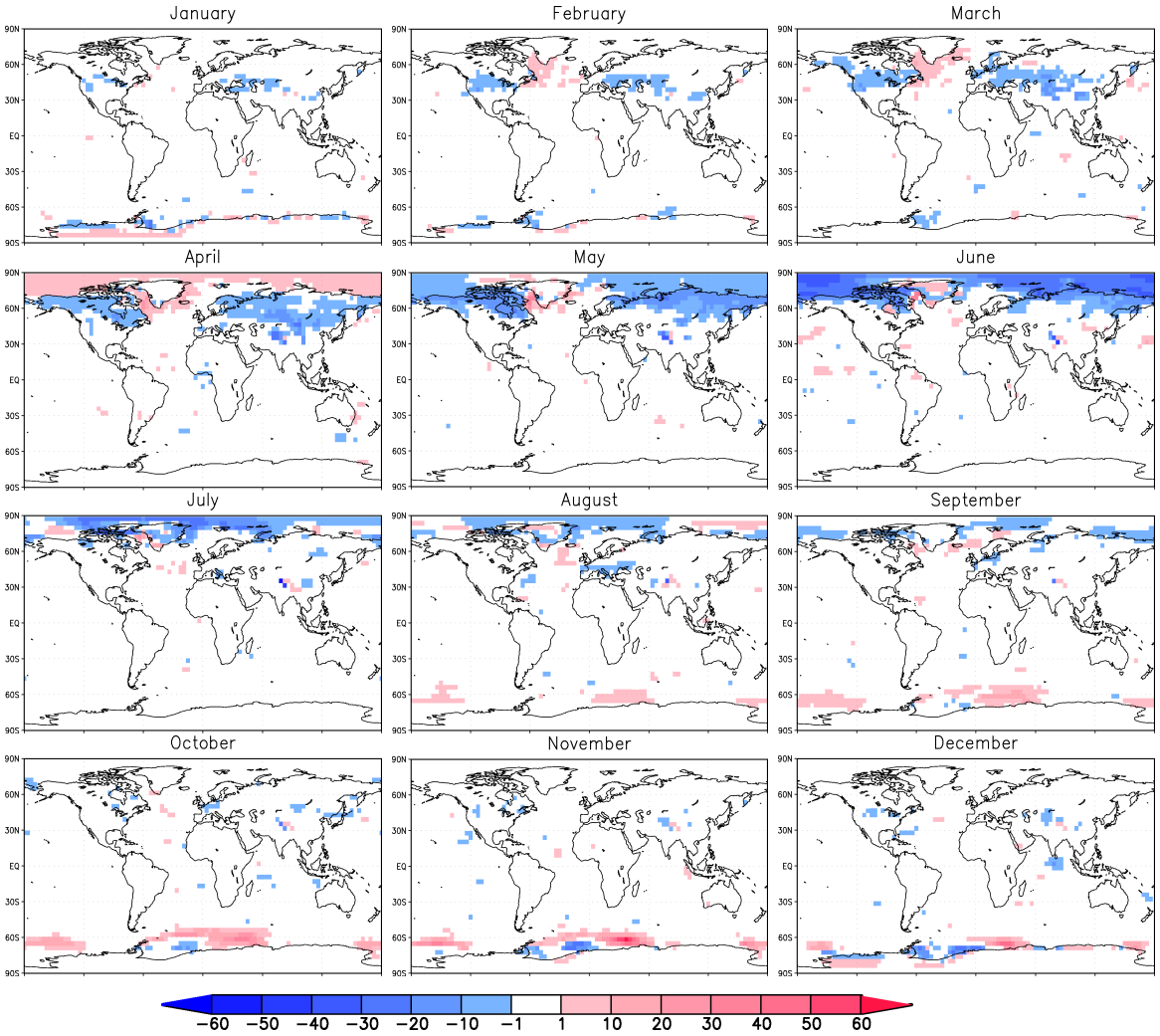

Figure 5.10: Differences in monthly mean absorbed surface solar radiation (CTRL_NA - CTRL_O), differences in $\mathrm{W\,m^{-2}}$. Only differences $> 1\ \mathrm{W\,m^{-2}}$ that are also statistically different at the 1 % level of significance are shown.

surface (cf. Figure 5.10), the surface heats less and thus emits less thermal radiation. This counteracts the increase in the radiative heat loss. Nevertheless, at TOA over the Arctic from February to August the net radiation is decreased (Figure 5.12). This shows that the effect of reflecting the incoming solar radiation is stronger than the effect of decreased thermal radiation emission. As the Arctic's surface temperature obviously does not drop as much as would be necessary to avoid an even larger radiative deficit, there must be an increase in net heat flux to the surface. For annual mean conditions this is shown in Figure 5.11. From the decreased heat flux from surface to the atmosphere it follows that even more energy has to be transported through the lateral boundaries into the Arctic atmosphere. As this transport includes an increase in net transport of sensible heat into the Arctic, the increased albedo induced deepened energy sink around the North Pole also cools those regions of the earth which are outside the NH energy sink region.

The situation from September to January is an exception and completely the opposite. During these months the already existing large TOA net radiation deficit over the Arctic is not increased any further. Instead, over the Arctic Ocean less TOA radiative heat loss occurs (Figure 5.12). In the CTRL_NA run in the Arctic Ocean more sea ice survived the summer. Therefore in autumn and winter more and thicker sea ice is present. Sea ice has a low heat conductivity. The higher fractional coverage and the increased thickness of sea ice lead to a reduced surface temperature, in particular compared to the open ocean surface but also compared to thinner sea ice. The surface temperature of the sea ice can become much lower than that of open water, which cannot drop below the freezing point of sea water. Generally, in autumn and winter the sea ice surface temperature is far below freezing point. According to the Stefan-Boltzmann-Law, emission of thermal radiation increases as T_s^4, with T_s being the surface temperature. For astronomical reasons no or only a small amount of shortwave radiation reaches the surface during boreal winter. Although the surface albedo is increased, there is for apparent reasons no change in surface absorption of solar radiation (Figure 5.10). Thus it is evident that an increased sea ice cover and thickness reduces TOA net radiation heat loss in winter.

In an annual mean sense, the overall effect of the slightly increased surface albedo of the NH sea ice and snow is an increase of the already existing radiative heat loss north of approx. 35° N (Figure 5.11). Towards the North Pole there is already an increase in radiative heat loss in the CTRL_O run. With the new albedo scheme the gradient of radiative heat loss between the North Pole and midlatitudes increases even more. The Arctic energy sink in the global climate system deepens. Although the increased radiative heat loss leads to decreased near surface air temperatures over the NH continents and the Arctic Ocean (Figure 5.15), the heat flux from the surface to the atmosphere is not increased in Arctic latitudes as described above. Despite the increased temperature difference between Arctic Ocean water and near surface atmosphere especially in autumn

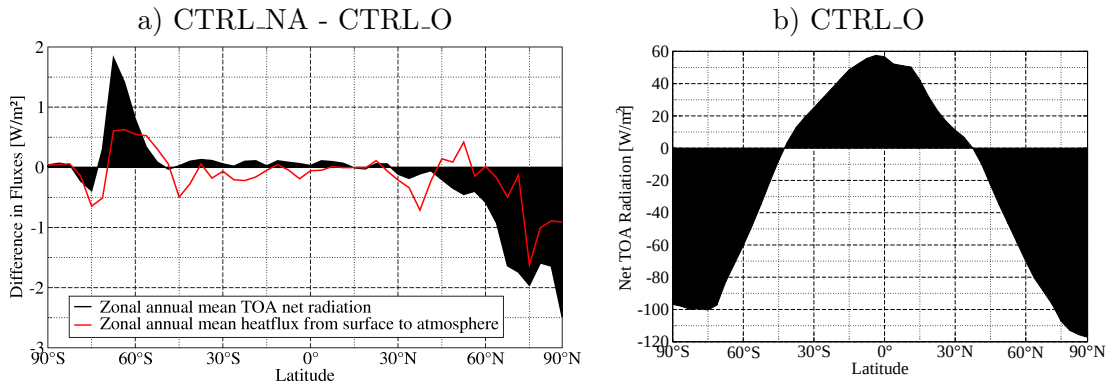

Figure 5.11: Difference in zonal annual mean TOA net radiation and zonal annual mean heat flux from the surface into the atmosphere (CTRL_NA - CTRL_O) (left) and zonal annual mean TOA net radiation from CTRL_O (right).

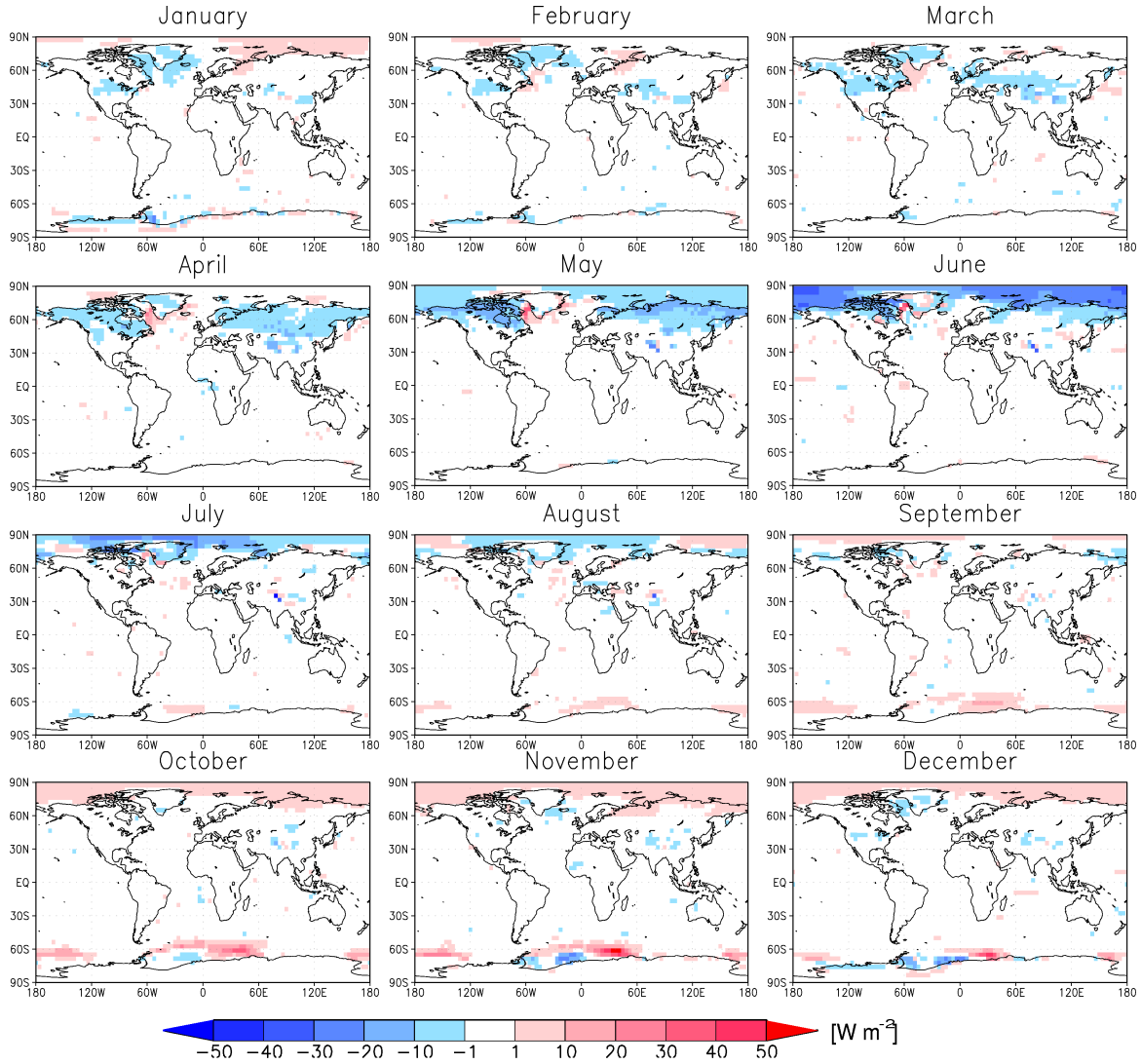

Figure 5.12: Differences in monthly mean net TOA (top of atmosphere) radiation (CTRL_NA - CTRL_O), differences in $\mathrm{W\,m^{-2}}$. Only differences $> 1\ \mathrm{W\,m^{-2}}$ that are also statistically different at the 1 % level of significance are shown.

(Figure 5.15), the heat flux from the surface to the atmosphere is even decreased (Figure 5.11). This result is caused by the higher sea ice coverage and the thicker sea ice, both reducing the heat flux from the relatively warm Arctic Ocean to the atmosphere. In addition, a reduced Fram Strait sea ice export reduces the net inflow of latent heat of melting into the polar cap oceans. Both decreased TOA net radiation balance and decreased surface heat flux to the atmosphere act additively in increasing the Arctic's energy deficit. Therefore the flux of moist static energy (MSE) (cf. Vavrus and Harrison 2003, Overland et al. 1996) into the Arctic has to increase to balance the energy deficit.

Cloud cover

As shown above, the surface albedo changes induced cloud cover changes do not much affect the transition of surface albedo differences into planetary albedo differences. Nevertheless, there are changes in the cloud cover. These changes occur predominantly in June during maximum insolation over the Arctic Ocean and the adjacent continental regions of Eurasia (Figure 5.14).

A comparison of the June and the annual mean cloud cover of the CTRL_O run against the D2 new cloud data set (Rossow et al. 1991) of the ISCCP (International Satellite Cloud Climatology Project) data (e.g. (Rossow and Schiffer 1991) and (Rossow and Schiffer 1999)) shows that ECHO-G simulates too much total cloud cover over the Arctic Ocean (Figure 5.13). Using the new albedo scheme, the overestimation over the Arctic Ocean as well as the underestimation over the northern boundary of the continents is reduced.

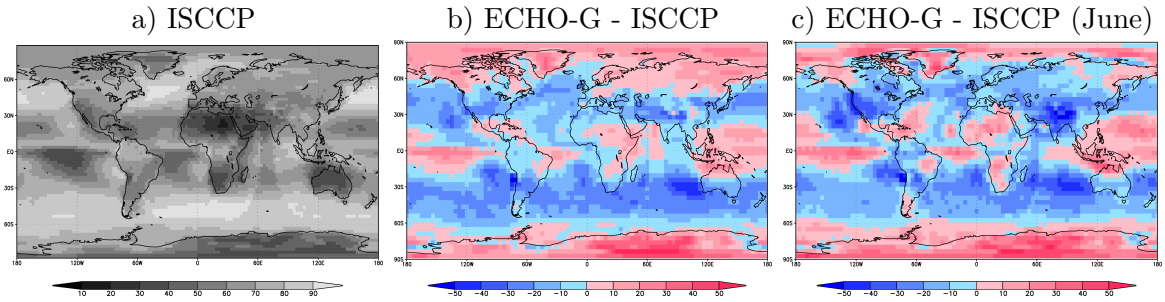

Figure 5.13: Total cloud cover. Annual mean cloud cover from ISCCP satellite observations in % (a). Differences of modelled total cloud cover to satellite measurements (ISCCP), differences in %, annual mean differences: (b), June mean differences: (c). ISCCP data cover the period from July 1983 to June 2005.

In the CTRL_NA simulation a reduction of cloud cover also occurs in the Arctic stratosphere in January (over Greenland) and February (over the Barents Sea) (not shown). This likely contributes to higher temperatures in the Arctic stratosphere in winter and spring in the CTRL_NA simulation because the heat loss by longwave emission in the stratosphere is reduced. The warmer Arctic stratosphere is discussed in the following section 5.3.

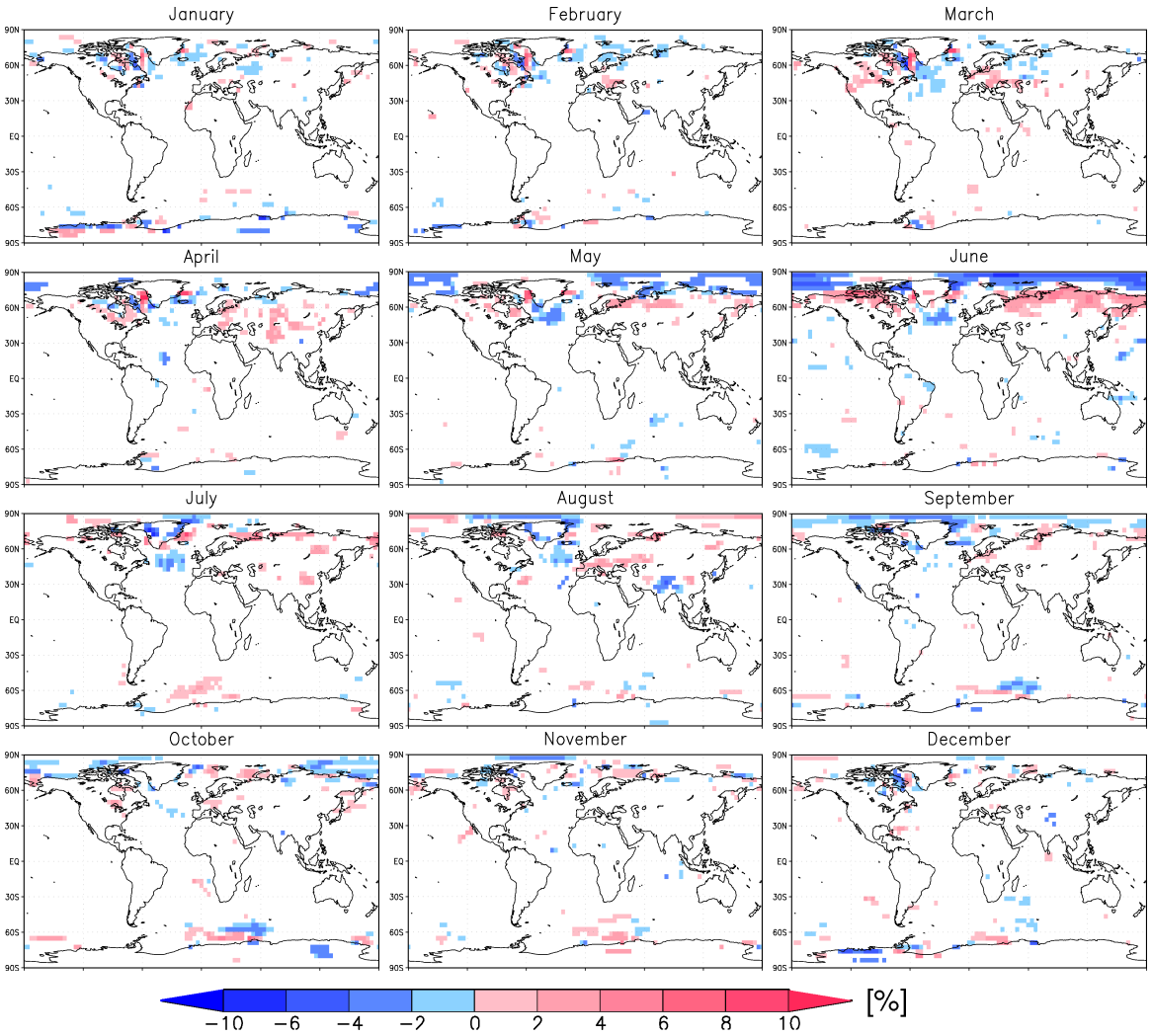

Figure 5.14: Differences in monthly mean total cloud cover (CTRL_NA - CTRL_O), differences in %. Only differences that are statistically different at the 1 % level of significance are shown.

5.3 Temperature

Near surface air temperatures

In agreement with the increased snow cover duration, the increased sea ice thickness in the Arctic Ocean, and the generally increased planetary albedo the T_{2m} is generally decreased in the CTRL_NA run. Statistically significant differences of the T_{2m} principally occur over all NH regions which are at least seasonally covered with sea ice or snow (Figure 5.15). The global annual mean T_{2m} is decreased by 0.066 K (Table 5.1).

Table 5.1: 95 % confidence intervals of annual mean T_{2m} differences (CTRL_NA - CTRL_O) over different regions.

Region	Difference in K	Region	Difference in K	Region	Difference in K
Global	$[-0.082, -0.050]$	30° S – 30° N	$[-0.047, -0.015]$	NH	$[-0.149, -0.097]$
		$\geq$ 66° N	$[-0.702, -0.556]$	SH	$[-0.029, +0.003]$

The most striking deviation from the generally decreased temperature in the NH is the increase in T_{2m} in the Greenland area during the whole year, in particular in late winter (Figure 5.15). Hence, with the application of an albedo scheme which increases the net radiation budget deficit in the Arctic, a pattern emerges which resembles the pattern of observational temperature trends in the Arctic. The observational trends for the winter mean temperature from 1958 to 2001 (Figure 2.3) around Greenland are negative despite a generally warming trend in the NH. During this time the AO / NAO was shifted towards its high polarity state (e.g. Hurrell 1995, Overland and Wang 2005). The situation in the CTRL_NA and CTRL_O runs is symmetrically contrary. In average, the CTRL_NA simulation has a lower NAO / AO polarity (Figure 5.26, Table 5.4) and thus a higher T_{2m} around Greenland in combination with a lower T_{2m} over northern Europe and the Barents Sea, especially in winter.

In spite of the less zonal circulation over Western Europe in winter, no statistically significant cooling occurs in Western Europe. An explanation may be given by the much warmer air masses over the northern North Atlantic. The decrease in frequency and / or duration of the advection of warm Atlantic air masses may be compensated in its effect on Western and Central Europe winter temperatures by the advection of even warmer Atlantic air masses.

The much higher temperatures around Greenland in the CTRL_NA simulation, especially in February and March, in the Davis Strait (up to 5 K difference in T_{2m}) are likely to arise from the large increase of heat flux from the ocean surface into the cold winter time atmosphere in that region (cf. section 5.1.2.) During that season the fractional coverage

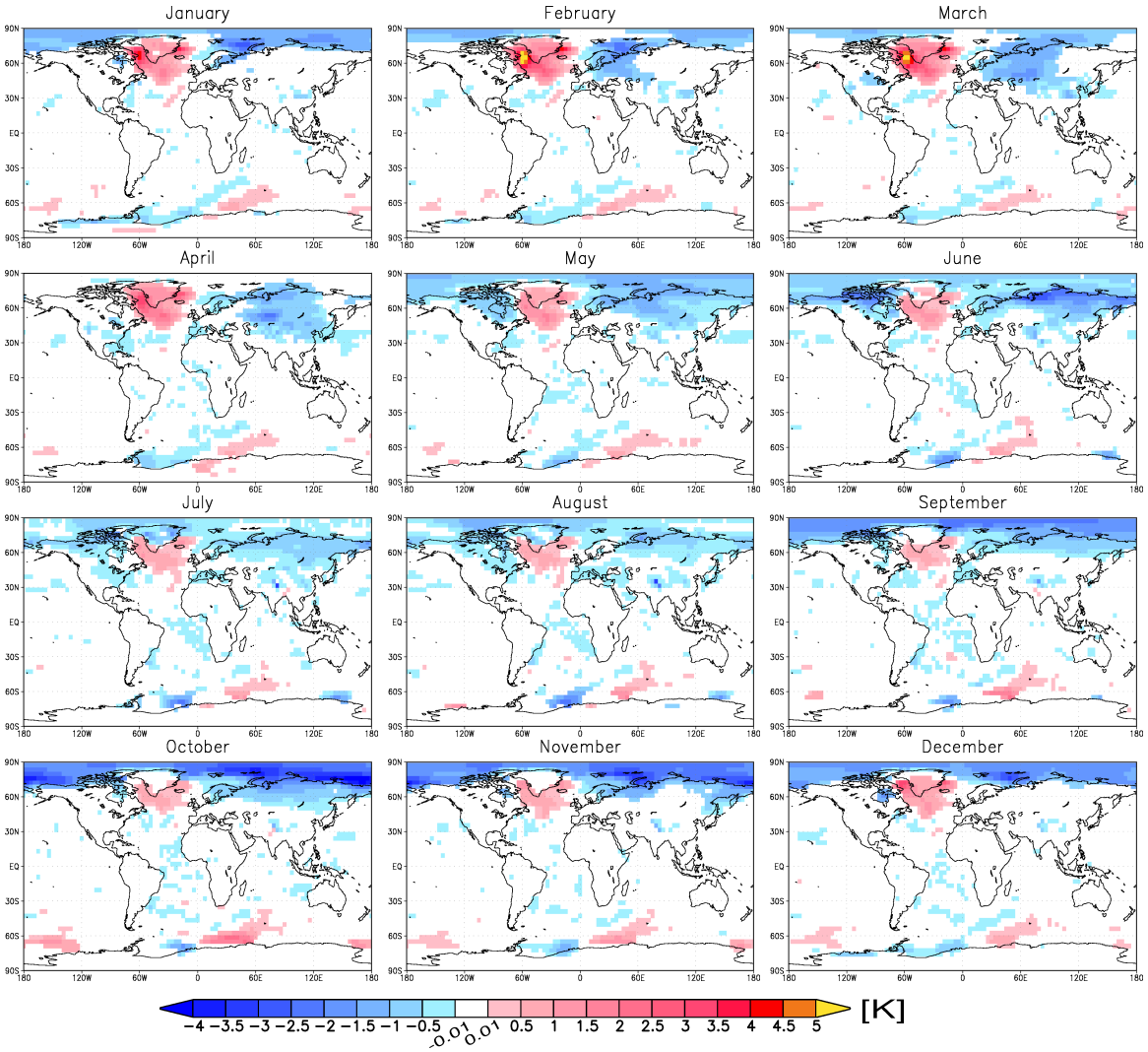

Figure 5.15: Differences in monthly mean T_{2m} (CTRL_NA - CTRL_O). Only differences > 0.01K that are also statistically different at the 1 % level of significance are shown.

in the Davis Strait in the CTRL_O run is maximum. Therefore a lower fractional cover in the CTRL_NA leads to maximum differences in heat release.

The changed heat flux over the Arctic Ocean explains the maximum decrease in T_{2m} over the Arctic Ocean in late autumn. The near surface air temperatures in the NH drop due to less insolation. In autumn the Arctic Ocean is covered with relatively thin sea ice which also does not completely cover the ocean surface, as the sea ice area and volume is minimal due to summer melting. Thus a large amount of latent and sensible heat can be released from the Arctic Ocean surface to the atmosphere above. As a result of the higher albedo in the CTRL_NA run, the sea ice in the Arctic Ocean is thicker and has a higher fractional coverage. The effects on coverage and thickness are maximum in late summer and autumn. In autumn the Arctic atmosphere cools whereas the sea surface temperature of the Arctic Ocean cannot drop. Therefore in autumn in the CTRL_NA

run the Arctic Ocean releases much less latent and sensible heat into the high-polar atmosphere leading to maximum impacts on the lower troposphere temperatures in that season (Figure 5.16).

As shown in the previous sections, maximum differences in TOA net radiation budget and in absorbed surface solar radiation occur in June whereas maximum differences in Arctic Ocean sea ice thickness and cover occur in autumn. Consequently, maximum increases in the lower troposphere and T_{2m} temperature gradient between polar and tropical latitudes are also found in June, as well as in October and November (shown in Figure 5.16 for lower troposphere temperatures). The decreased temperatures of the lower troposphere in June around 70° N emerge predominantly from the increase of snow remaining in the tundra.

The seasonal cycle (i.e. JJA mean minus DJF mean) of the Pan-Arctic T_{2m} is decreased by 0.074 $[-0.042, 0.190]$ K, where $[-0.042, 0.190]$ K denotes the 95 % confidence interval. The decrease is neither statistically nor physically significant. This is an interesting finding, because the seasonal cycle in absorbed solar radiation over the Pan-Arctic region (102.4 $\mathrm{W\,m^{-2}}$ in the CTRL_O simulation) is reduced by about 6.8 % ($[6.6, 7.4]$ $\mathrm{W\,m^{-2}}$).

Temperatures in the troposphere and stratosphere

The temperature changes in the Arctic atmosphere, which originate from a changed albedo of the seasonal varying NH cryosphere, show striking similarities to those changes arising in simulations with increasing GHG concentrations. In both cases, surface albedo changes (CTRL_O minus CTRL_NA) and GHG changes (21^{st} century minus 20^{th} century), the largest changes in the temperature composition of the Arctic atmosphere are a cooling of the stratosphere (maximum in March) and a warming in the troposphere (maximum near the surface in October and November) (Figure 5.16 and Figure 5.18 (b)). This is accompanied by either just small changes in the tropical troposphere (CTRL_O minus CTRL_NA, Figure 5.16) or GHG concentration changes induced temperature changes in the whole troposphere which are opposite in sign to those of the stratosphere (Figure 5.18 (a)). Because the tropopause is much lower in the Arctic than in the tropics, temperature changes along a pressure level intersecting the tropopause have opposite signs of change in the Arctic and in the tropics, as these pressure levels are part of the lower Arctic stratosphere as well as of the upper tropical troposphere. Not only the pattern but also the timing of temperature changes in the upper atmosphere indicate similarities between the simulations with GHG changes and surface albedo changes. Figure 5.16 as well as Figure 5.18 (b) clearly show that a profound temperature change in the Arctic stratosphere starts in December and ends abruptly in May.

Figure 5.17 shows the well-known behaviour of models when forced with increasing GHG concentrations. Under increasing GHG concentrations the maximum warming of the free troposphere takes place in the upper troposphere in tropical latitudes. This finding is consistent with climate change prediction runs as well as with theoretical considerations (e.g. U.S. Climate Change Science Program 2006). Similar to the results of the changed albedo runs, the largest changes in the meridional temperature gradient between equator and the Arctic occur between the 200 hPa and 100 hPa level. In late winter and early spring the changes in these pressure levels are maximum. As the Arctic lower stratosphere cools the most in March, the meridional temperature gradient shows at approx. 150 hPa the largest changes in particular in March (Figure 5.18). It is important to mention that ECHO-G used in this study does not have any chemical components included. Thus the stratospheric cooling (or warming, respectively) in the scenario or the changed cryospheric albedo simulation with ECHO-G cannot have its origin in ozone depletion. Ozone depletion was suggested to be one of the most important drivers for Arctic stratospheric cooling (e.g. Shindell et al. 1999, Overland and Wang 2005). In both cases (albedo and GHG changes) the effect on stratospheric temperatures is maximum in late winter and early spring, as it would also be expected as an effect of ozone depletion (cf. section 2.3).

Zorita et al. (2004) performed a model simulation with the same version of ECHO-G (lacking a realistic representation of the stratosphere) which is also used in the current study. One aspect of their work was the climate of the Late Maunder Minimum (LMM) which is characterised by a lower activity of the sun leading to a decreased insolation and therefore to lower global temperatures. In accordance to the results of Shindell et al. (2001) Zorita et al. (2004) found for the LMM a positive anomaly in temperature at 200 hPa in polar latitudes and a negative anomaly in low latitudes. In their model simulation, Shindell et al. (2001) also detected a shift of the LMM winter NAO towards its negative polarity. This finding supports their hypothesis that a change in the meridional temperature gradient along a pressure level intersecting the tropopause is responsible for shifts of the phase of the NAO and AO.

The warmer winter and early spring Arctic stratosphere in the CTRL_NA gives a hint that the polar vortex has also weakened. Weakening of the polar vortex and a warming of the Arctic stratosphere are self-amplifying processes as they interact with each other. If the polar vortex weakens, an increase in entrainment of warmer subpolar and midlatitude upper troposphere and lower stratosphere air masses into the Arctic stratosphere, which is very cold in winter, also occurs. Hence the Arctic stratosphere warms and the polar vortex weakens even more. In spring, this entrainment leads to a break-down of the polar vortex.

Langematz et al. (2003) analysed stratospheric changes from 1979 to 2000 using model simulations and reanalysis data. They suggested that radiative effects of O_3 and

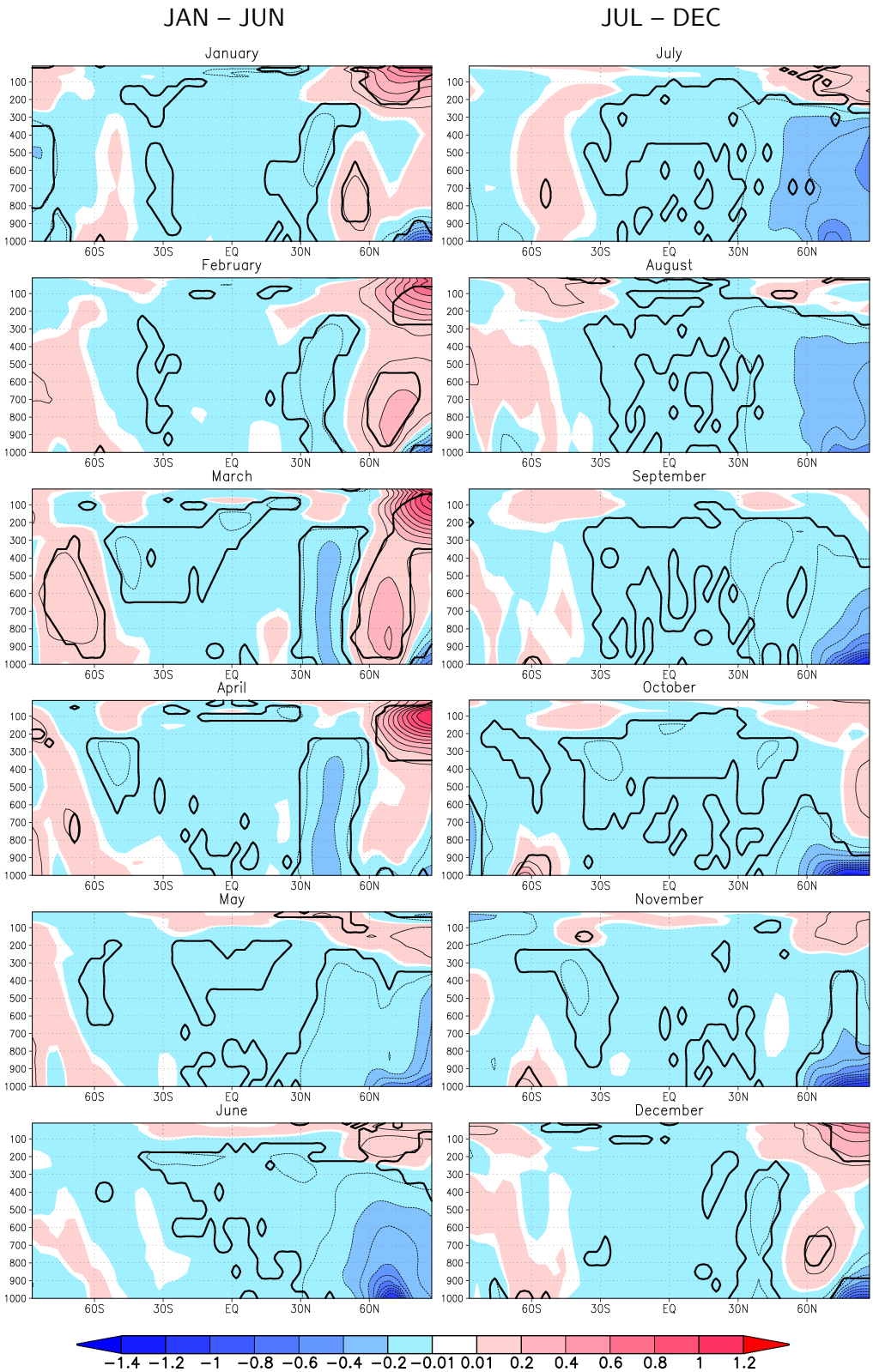

Figure 5.16: Differences in zonally averared monthly mean temperatures (CTRL_NA - CTRL_O) in K. x-axes indicate latitude, y-axes pressure level in hPa. Interval of contour lines 0.1 K. Thick black lines denote regions with differences that are statistically different at the 10 % level of significance.

CO_2 changes cause the observed cooling trend in the stratosphere in low to middle latitudes, while the cooling of the Arctic stratosphere in winter is enhanced due to decreased dynamical heating.

The findings in the current subsection dealing with Arctic stratospheric temperature changes – initially caused by NH albedo changes – underpin the suggestion of Langematz et al. (2003) that processes other than radiative effects of O_3 and CO_2 have to be considered to explain the changes in Arctic stratosphere in spring. Here it was also shown that these changes are maximum in spring. Radiative cooling may, nevertheless, also play a contributing role in generating the stratospheric temperature differences between the CTRL_NA and the CTRL_O simulation. For example, radiative cooling is also caused by emission of longwave radiation from water vapour or clouds. For March, Figure 5.19 shows exemplarily a drying of the stratosphere in the CTRL_NA run. Thus the radiative heat loss is reduced. This argument, however, is not valid if tropical latitudes are considered. For example, despite the decreased humidity in the stratosphere over Africa, the stratosphere over Africa is cooler in the CTRL_NA simulation.

Using NCEP reanalysis data for the period from 1979 to 2003, Hu et al. (2005) pointed out that the NH extra-tropics and polar regions show nearly opposite tendencies between early and late winter. In late winter there is a strong tendency towards a stronger and colder polar vortex, while trends in early winter point towards a low index state of the AO. A similar result was found in a more recent study by Langematz and Kunze (2006) when using NCEP and ERA40 reanalysis data and a model simulation for the period from 1979 to 1999. However, when they extended the analysis to the period from 1965 to 2005 Langematz and Kunze (2006) detected trends smaller in amplitude and partly opposite in sign since the 1980s. In the current study, nevertheless, the differences in the Arctic stratosphere between the CTRL_NA and the CTRL_O run are in accordance with the results of Hu et al. (2005) and Langematz et al. (2003), both in terms of the timing of the differences (March) and in terms of the coexistence of a positive AO phase in late winter and the cooler Arctic stratosphere in late winter. Hu et al. (2005) and Langematz et al. (2003) found the different trends of the Arctic stratosphere between early and late winter in analysis of reanalysis data of the 1980s and 1990s when there was a strong trend towards a positive AO phase (Overland and Wang 2005). In the current study, the situtation is quite similar. There is a higher polarity of the AO phase and also a cooler Arctic stratosphere in the CTRL_O run.

The changes in the polar vortex (including AO phases, zonally averaged zonal wind speed etc.) associated with Arctic stratosphere temperature differences between the CTRL_NA and the CTRL_O simulation will be analysed in the following section 5.4.

A maximum increase in the temperature gradient between the Arctic and the tropic lower troposphere (below approx. 900 hPa) occurs in autumn (in particular in October)

and early winter (Figure 5.16). Figure 5.22 shows clearly that the changed meridional near surface temperature gradient does not have a similar impact on the zonally averaged zonal wind speed as the changed temperatures in the Arctic stratosphere in late winter.

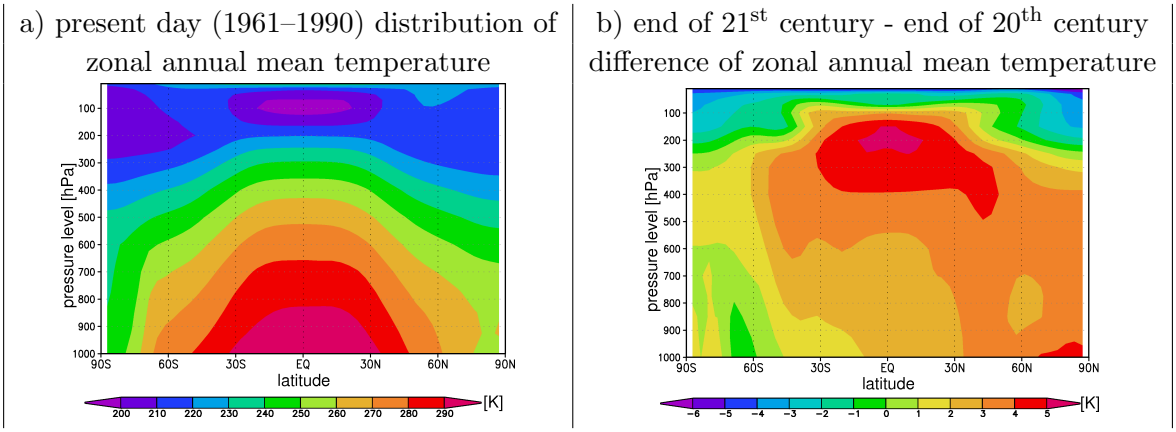

Figure 5.17: Cross-sections of present day atmospheric zonally averaged annual mean temperature of ECHO-G (a) and respective change under IPCC SRES B2 emission scenarios until the end of the 21st century (b). b): 2071–2100 mean minus 1961–1990 mean.

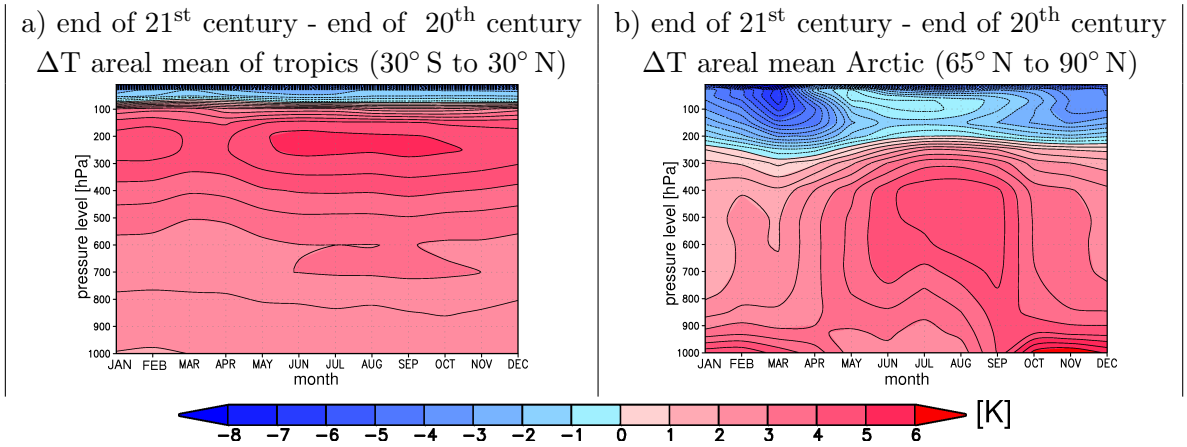

Figure 5.18: Atmospheric temperature development of ECHO-G under IPCC SRES B2 emission scenarios. Mean temperatures of 2071–2100 minus mean temperatures of 1961–1990 temperatures of the H_B2_NA run. a) differences of atmospheric temperatures within tropical latitudes, b) differences of atmospheric temperatures over the polar cap. Contour lines denote 0.5 K intervals. Note the increased temperature gradient between the polar cap and the tropics between 200 hPa and 100 hPa especially in March and April.

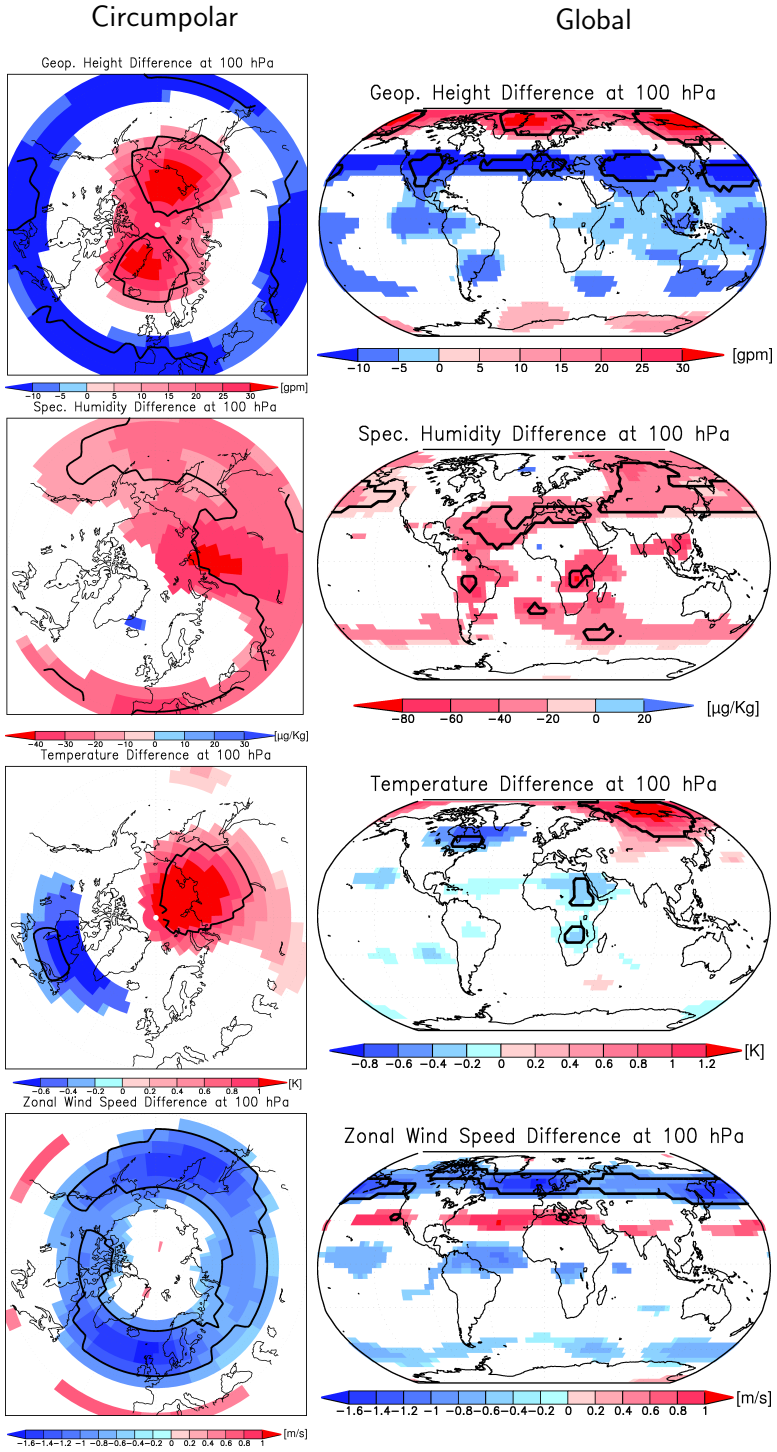

Figure 5.19: Differences in March mean properties at 100 hPa (CTRL_NA - CTRL_O). Only differences that are statistically different at the 10 % level of significance are shown. Thick black lines denote areas with differences statistically different at the 1 % level of significance. Displayed variables (top to bottom): Geopotential height, specific humidity, temperature, and zonal wind speed.

5.4 NAO / AO and global circulation response

Mean sea level pressure and geopotential height

In accordance to the near surface air cooling over Scandinavia (Figure 5.15) and the increased sea ice cover in the Barents Sea (Figure 5.2) in the CTRL_NA run, a shift of the SLP towards a cold high-pressure zone in that region emerged for winter, spring, and autumn (Figure 5.20). The most pronounced SLP increase is evident in the eastern Greenland Sea and over northern Scandinavia in winter which also explains the decreased sea ice export through the Fram Strait. During spring the most widespread differences are present. The zone of positive SLP differences encloses large areas of north-western Eurasia, the Barents Sea, the Greenland Sea, the Arctic Ocean, central Canada, and north-eastern Siberia.

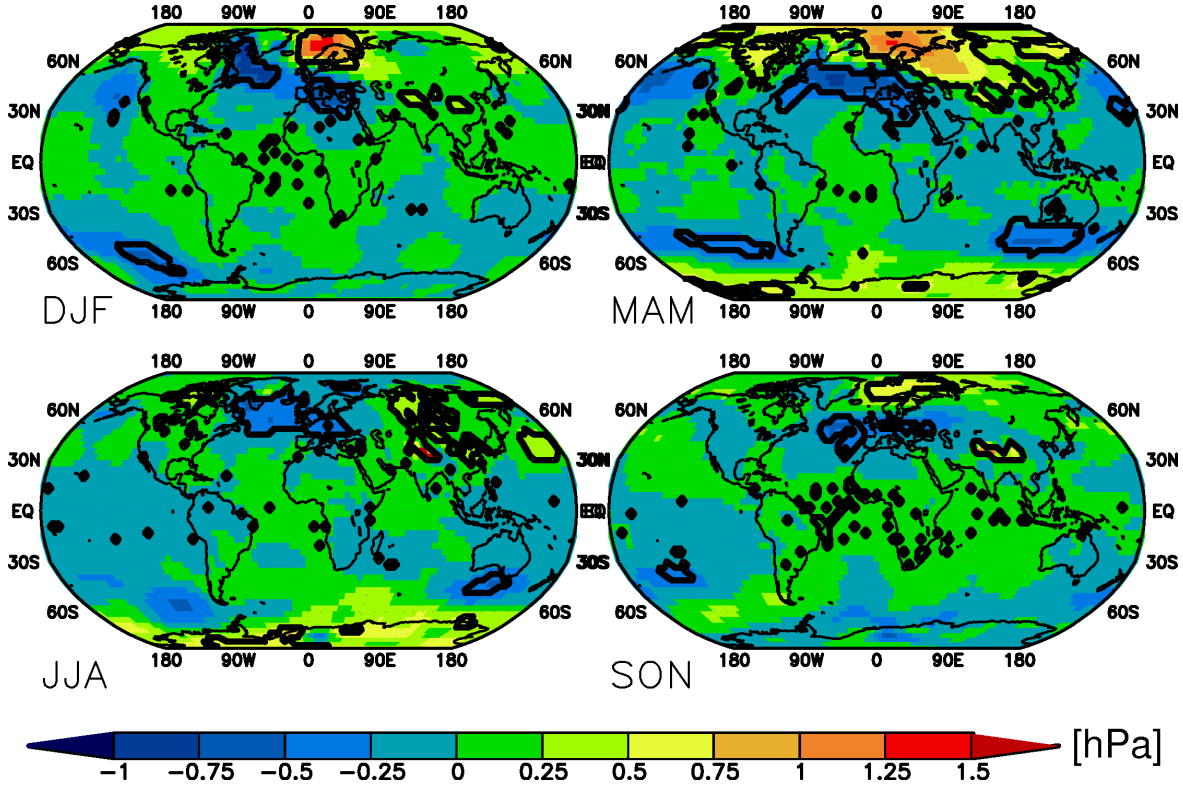

Figure 5.20: Seasonal mean differences in SLP (CTRL_NA - CTRL_O). Thick black lines enclose areas showing differences that are statistically different at the 5 % level of significance.

During boreal spring and summer Antarctica also shows an increase in SLP, although over large areas of Antarctica this increase is not statistically significant. Particularly in boreal spring the SLP increases over Antarctica are accompanied by statistically significant decreases of SLP in the southern South Pacific and the seas between Australia and Antarctica. This increases the zonal mean SLP gradient from Antarctica to the Southern Ocean.

Generally, over the snow covered parts of the NH continents and over the Arctic Ocean the SLP tends to increase in the CTRL_NA run. The largest rise in SLP is found between northern Scandinavia and Svalbard and in the Kashmir Mountain region which also has the largest rise in snow cover duration.

Over the northern North Atlantic the SLP is decreased in each season. The pattern of the SLP differences over the eastern North Atlantic region resembles the pattern of the NAO. Different from the NAO pattern the differences in SLP over the Davis Strait and the Labrador Sea have the same sign of change as the differences in the Mediterranean. The decrease in SLP accompanied by an increase in heat flux into the atmosphere over those sea areas with a reduced sea ice cover is in accordance with the findings of e.g. Alexander et al. (2004).

In DJF a maximum increase in the 500 hPa geopotential height occurs in the Denmark Strait region (Figure 5.21). This area is located downstream of the Davis Strait region. Thus the release of heat into the atmosphere in the seas around southern Greenland leads to an increase of the 1000 - 500 hPa thickness, as the air masses are warmer. This may explain why the maximum rise of the geopotential height and the maximum increase of SLP are not located in the same region.

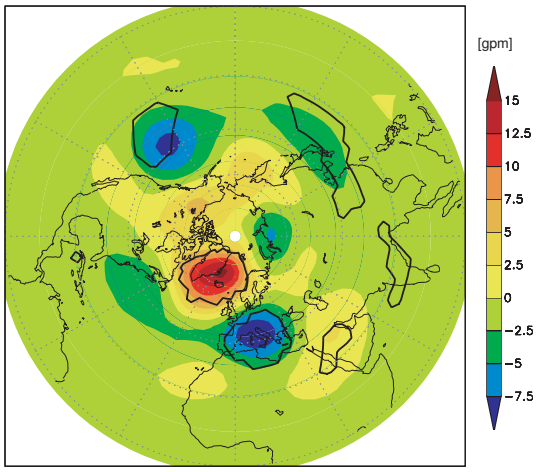

Figure 5.21: DJF mean differences in 500 hPa geopotential height (CTRL_NA - CTRL_O). Thick black lines enclose areas showing differences that are statistically different at the 5 % level of significance.

Zonal mean quantities: zonal wind speed, SLP and geopotential height

Due to changes in the meridional temperature gradient in the NH, changes in the zonal wind speed as well as in the geopotential height arise, as shown in Figures 5.22 and 5.24. The changes are neither maximum in NH autumn, when there are maximum changes in the near surface meridional temperature gradient, nor in NH winter, when circulation

changed could preferably project on atmospheric modes such as the AO, but in NH early spring (Figure 5.22).

Figure 5.22 shows the temporal evolution of differences in zonal mean zonal wind speed within the annual cycle. The zonal mean zonal wind changes are greatest in March and April. Hu et al. (2005) also found in NH reanalysis data a trend for late winter, not for early winter. Greatest meridional T_{2m} differences between the CTRL_O and the CTRTL_NA run occur in October. Obviously those near surface temperature changes – even if they extend throughout the complete boundary layer in the Arctic – have just a small impact on the zonal wind speed. The change in zonal mean wind speed starts when the stratosphere gets warmer in December in the CTRTL_NA run compared to the CTRL_O run. In winter and spring the temperature of the Arctic stratosphere is higher in the CTRL_NA run than in the CTRL_O run and therefore the meridional temperature gradient along approximately 200 hPa from the North Pole to the equator is decreased. Consequently, the zonally averaged zonal wind speed in the Sub-Arctic atmosphere is also decreased throughout all atmospheric levels (Figure 5.22). This strengthens the hypothesis that changes in meridional temperature gradients between the Arctic Stratosphere and the tropic upper troposphere lead to changes in the zonal wind strength, the polar vortex, and the phase of the AO (cf. Shindell et al. 1999). An interesting side aspect is the fact, that ECHO-G shows this behaviour without having a well resolved representation of the stratosphere which was stated by Shindell et al. (1999) to be necessary and also shows these circulation changes without any ozone depletion.

The differences in zonal mean zonal wind speed (Figure 5.22) start in December in the Sub-Arctic stratosphere at those latitudes where a maximum gradient in temperature differences at around 200 hPa occurs (Figure 5.16). In accordance with the increasing temperature differences in the Arctic stratosphere from November to April (Figure 5.16), the differences in zonal mean zonal wind speed throughout all latitudes and levels of the atmosphere increase from December to March (Figure 5.22). Greatest differences occur in March in terms of a reduced zonally averaged zonal mean wind speed at approximately 50° N in the troposphere and around 60° N in the upper stratosphere. In April the differences are still pronounced. Within the temporal evolution of the differences from December to April, the differences in zonal mean zonal wind speed start in the stratosphere and propagate downwards into the troposphere reaching the surface in February. The difference pattern is most pronounced in March and April. During these months, statistically significant differences in the SH are also found. In these months the difference pattern is nearly symmetric at the equator. However, the amplitude of the differences is smaller in the SH. In accordance to Lynch et al. (2003) an explanation for the differences in the SH might be a changed equator to pole heat transport in the NH which influences heat and momentum transport in the SH. However, this statement does not include any detailed description of the physical mechanism behind the simulated differences.

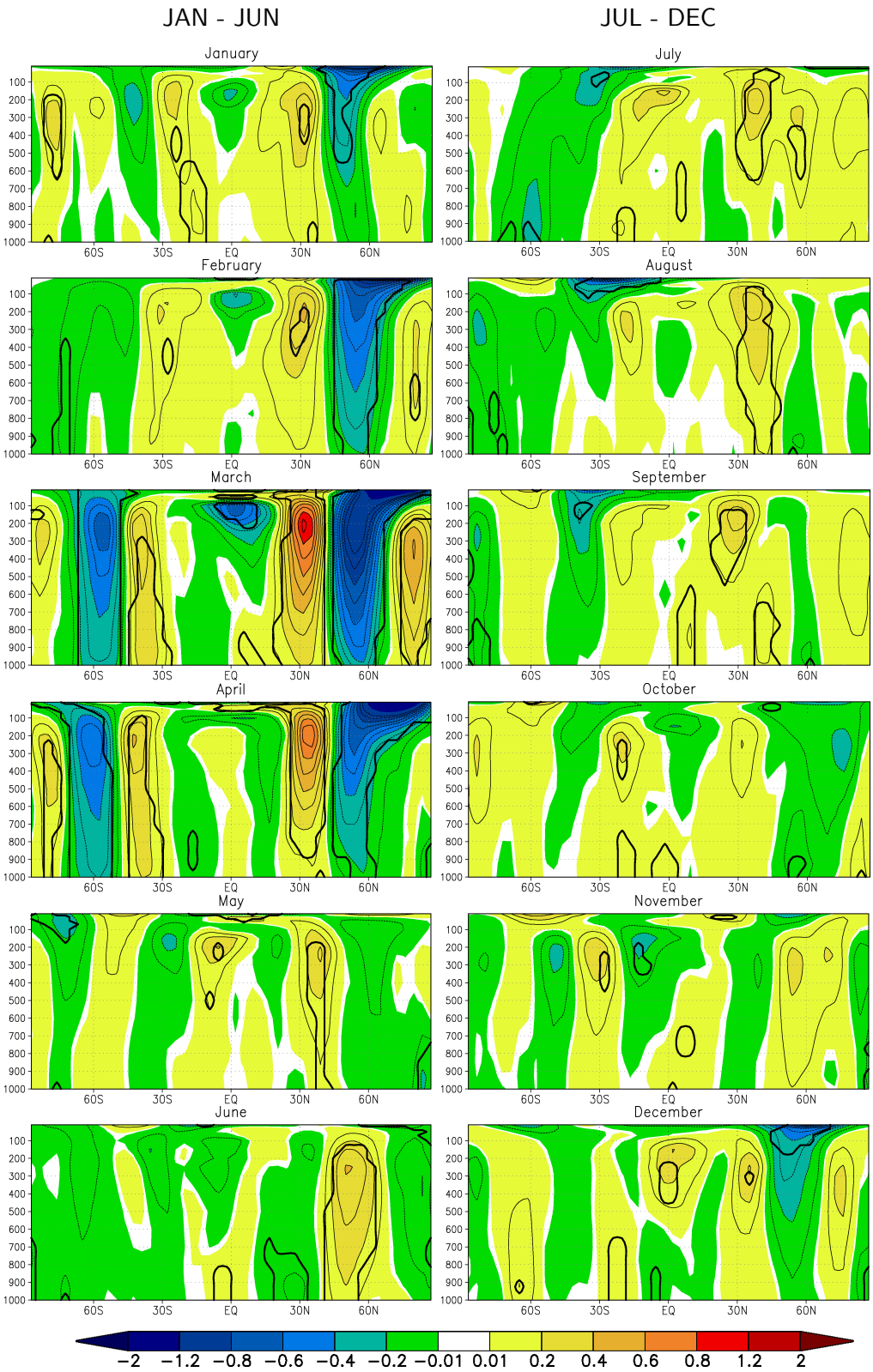

Figure 5.22: Differences in zonally averaged monthly mean zonal wind speed (CTRL_NA - CTRL_O) in $\mathrm{m\,s^{-1}}$. x-axes indicate latitude, y-axes pressure level in hPa. Interval of contour lines: 0.1 $\mathrm{m\,s^{-1}}$. Thick black lines denote areas with differences that are statistically different at the 10 % level of significance.

To clarify the question as to whether the SH differences in zonal mean zonal wind speed occur principally as a direct response to individual circulation anomalies in the NH, a correlation analysis was performed. The analysis was applied to each of the individual simulation runs. On several atmospheric levels, time series of zonal mean zonal wind speed at 57° N averaged from January to April were correlated to the respective time series at 57° S averaged from March to April. All correlations were small but positive. However, no correlation greater than 0.08 occurred. Thus in individual years a changed zonal flow in the NH does not change the zonal flow in the SH in the same direction. Also no correlation between the AO and the AAO exists (Table 5.5). Nevertheless, a change in the long-term mean state of the NH circulation is accompanied by a symmetric response in the mean state circulation of the SH when almost the whole NH shows statistically significant changes.

To address the question as to what may cause the differences shown in Figure 5.22 let us assume the changed albedo parameterisation favours – for whatever reason – a tendency of the Arctic stratosphere to slightly warmer temperatures in late autumn. Then it is more likely at the start of each individual polar vortex season that the polar vortex is weaker and therefore the probability of dynamic heating increases. This again raises the probability of a further weakening and dynamic heating and so on until the final breakdown of the polar vortex in boreal spring.

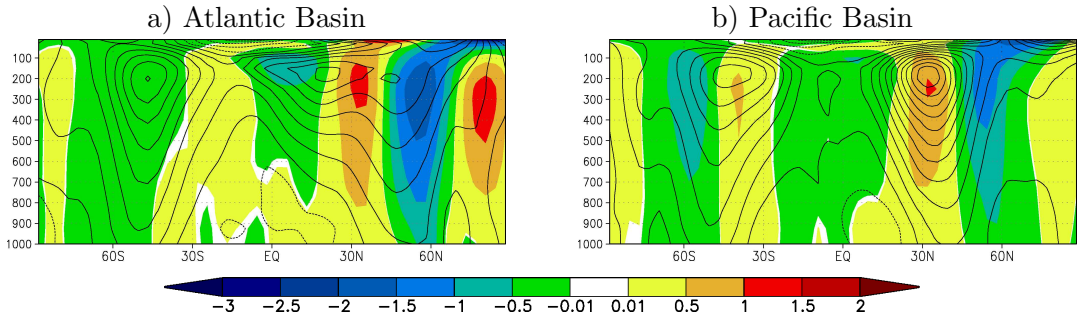

Figure 5.23: Differences in monthly mean zonal wind speed (CTRL_NA - CTRL_O) in $\mathrm{m\,s^{-1}}$. Interval of contour lines 5 $\mathrm{m\,s^{-1}}$. Contour lines denote March mean zonal wind speed of the CTRL_O run.

The climatological features for the Atlantic and the Pacific basin are at different latitudes (Ambaum et al. 2001). To account for this the differences in zonal mean wind speed are shown exemplarily for March for each basin separately (Figure 5.23). In principal, both basins show the same results. A common feature of both basins is the decrease in zonal wind speed north of the jet axis in the NH and a decrease of zonal wind at the sub-polar latitudes. Contrary to the Atlantic basin in the Pacific basin the maximum increase in the zonal wind speed occurs near the jet axis. Thus in the Pacific basin no shift of the jet towards north or south occurs. Figure 5.19 gives an impression of nearly polar-symmetric differences in zonal wind speed at 100 hPa with maximum differences over the North Pacific and the North Atlantic. Maximum differences over the North

Pacific are at latitudes about 5° lower than over the North Atlantic.

The circulation changes can also be seen in the zonal mean geopotential height. Figure 5.24 shows the weakened and warmed polar vortex in March (q.v. Figures 5.16, 5.19, and 5.22) by an increase of the 100 hPa geopotential height. Qualitatively all levels show the same behaviour. There is an increase in geopotential height north of approx. 55° N and south of approx. 55° S accompanied by a decrease at the midlatitudes of each hemisphere. However, the amplitude in the SH decreases as time goes by (Figure 5.24). In DJF almost no differences in the SH occur (Figure 5.25 a)).

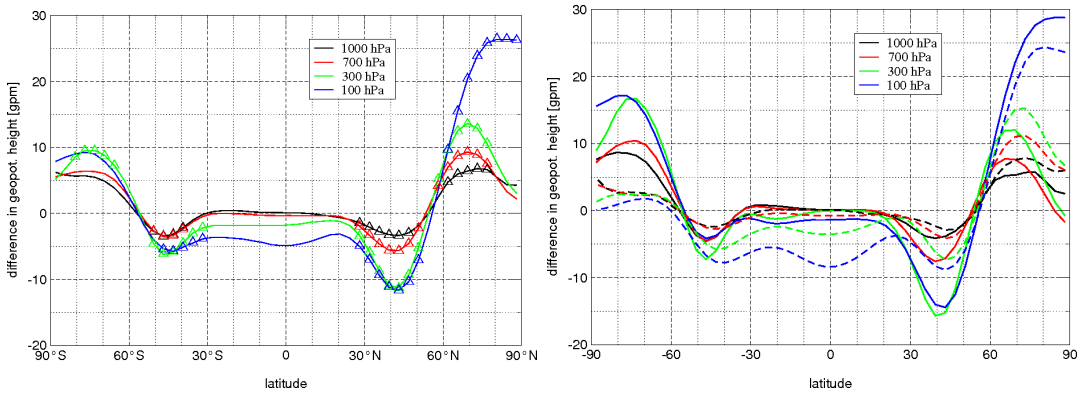

Figure 5.24: Difference in March zonal mean geopotential height (CTRL_NA - CTRL_O). Left: 400 year period, triangles indicate latitudes at which differences occur that are statistically different at the 5 % level of significance. Right: Two 200 year sub-periods, solid lines indicate first sub-period, dashed lines indicate second sub-period. No test of significance applied on the right Figure.

The increase in the 100 hPa geopotential height around the North Pole and the decrease at about $40 - 45°$ N arise from an annular structure of the geopotential height difference in the NH at 100 hPa which is nearly perfectly symmetric to the North Pole (Figure 5.19). However, there are slight deviations from an idealised annular structure as the region of maximum increase of the geopotential height splits into two – nonetheless conjunct – sub-regions. One sub-region is shifted away from the Pole towards the Pacific Basin, the other towards the Atlantic Basin (Figure 5.19).

The late winter and early spring albedo induced changes in circulation are qualitatively very similar to those occurring in global climate warming experiments. The NH albedo change induced circulation changes as well as the GHG induced circulation changes – both indicated by the change of geopotential height and SLP (Figures 5.24 and 5.25) – are symmetric on the equator. Moreover, both albedo and GHG induced changes in SLP and geopotential height have opposed signs in the Arctic and in midlatitudes. However, in the albedo induced changes the amplitude is smaller by approximately one magnitude. Yin (2005) describes a poleward shift of storm tracks in simulations of the 21st century that is accompanied by a shift towards the high index state of the AO and AAO. Different storm track related variables (such as eddy kinetic energy) show a shift

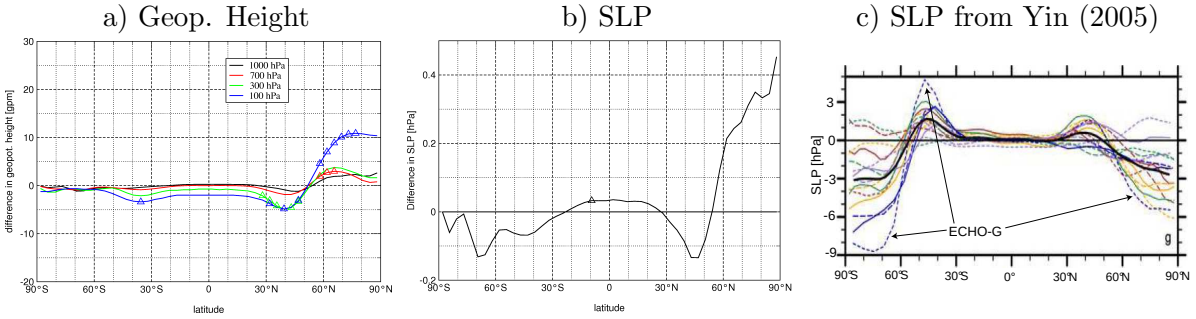

Figure 5.25: Differences in DJF zonal mean geopotential height (a) and SLP ((b and (c)), triangles indicate latitudes at which zonal mean differences occur that are statistically significant at the 5 % level of significance ((a) and (b)). (a) and (b): CTRL_NA - CTRL_O, (c) from Yin (2005): 2081–2100 minus 1981–2000 zonal mean DJF SLP for 15 coupled models. Thick black line indicates ensemble mean.

in zonal mean values that are to a large degree symmetric on the equator in DJF. Figure 5.25 c) shows this exemplarily for the SLP. No comparably pronounced symmetry on the equator occurs in DJF in the SH in the albedo runs (Figure 5.25 a) and b)). Hu et al. (2005) observed a different behaviour of NH circulation changes between 1979 and 2003 in early and late boreal winter using NCEP reanalysis data. Whereas in late winter the AO shows a strong trend towards a positive phase there is a negative trend in early winter. Similar effects as described by Yin (2005) and Hu et al. (2005) are also detectable in the different sea ice albedo parameterisation control runs. Zonal mean differences of zonal wind speed are much smaller in DJF than in March. Also the frequency distribution of the AO / NAO phase differs much more in March than for the DJF mean (Figure 5.26 and Table 5.2).

NAO, AO and AAO

For reasons of comparison, the time series of the NAOI (as well as the AOI and AAOI) of both the CTRL_NA and the CTRL_O run are based on the first EOF of the CTRL_O run and on the mean SLP of the CTRL_O run. The anomaly patterns of the CTRL_NA and the CTRL_O run were defined as the differences of the SLP patterns to the respective mean SLP pattern of the CTRL_O run. Then the anomaly patterns of the CTRL_NA and the CTRL_O run were projected onto the related first EOF pattern of the CTRL_O run resulting in the time coefficients of the NAO (or AO or AAO). These time coefficients were normalised by the standard deviation of the respective time coefficients of the first EOF of the CTRL_O.

As expected from the changed mean state in SLP in the CTRL_NA run the NAO, AO, and AAO changed towards a lower polarity. The changes are small in DJF leading to differences in the time coefficients which are not statistically significant (Table 5.4). In fact, in case of the mean AAOI in DJF there are almost virtually not any differences between the CTRL_NA and the CTRL_O simulation. In March the situation is different.

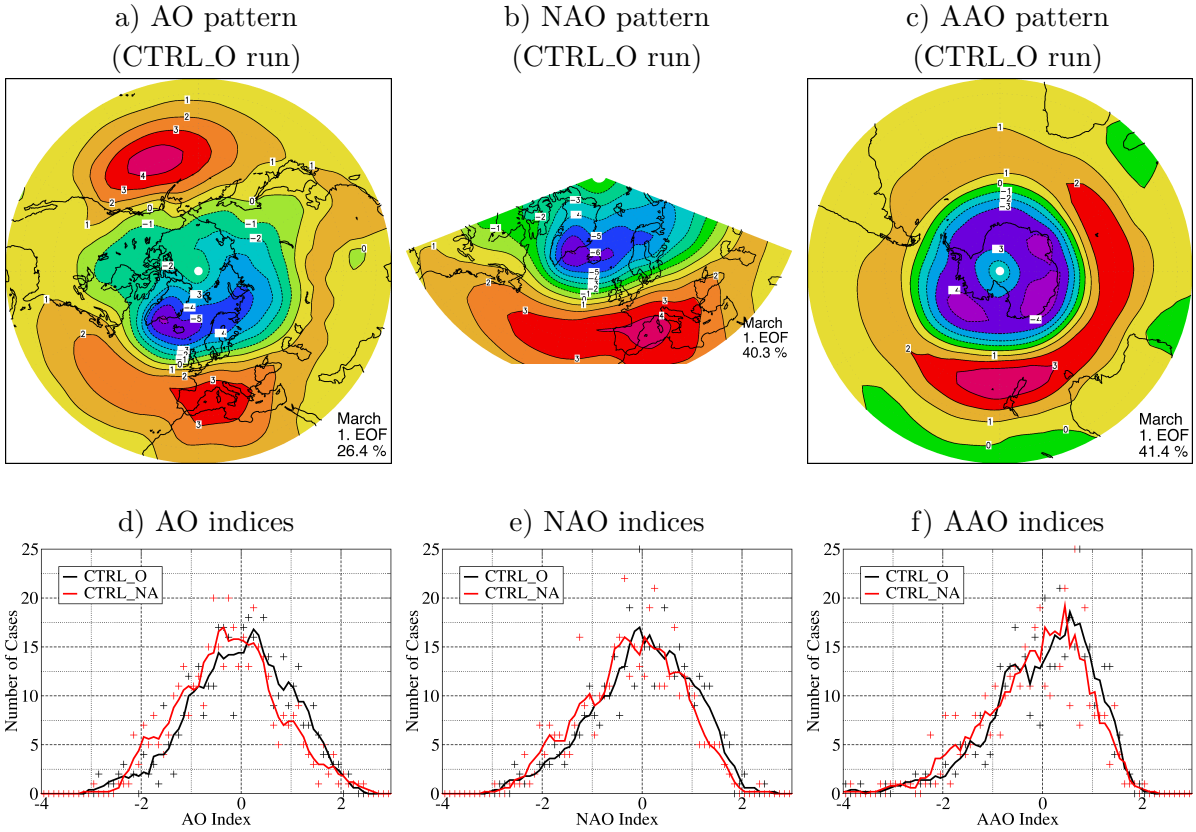

Figure 5.26: First EOFs of March SLP anomalies. From left to right AO, NAO, and AAO. First row: EOF pattern of the CTRL_O run. Second row: Distribution of respective principal component. Crosses indicate distribution under a class width of 0.1. Curves denote running means over 5 classes.

The NAO, AO, and AAO show a shift towards their low polarity if the new albedo scheme is applied (Figure 5.26) which is in accordance with the findings concerning the zonal mean zonal wind speed differences and the changes in the zonal mean geopotential height. The mean NAOI, AOI, and AAOI from the CTRL_NA run have statistically significant lower values than from the CTRL_O run (Table 5.4). Also the cumulative distribution functions of the NAOI, AOI, and AAOI are different (Table 5.2). From Table 5.2 it follows that differences as large as seen between the cumulative distribution function of the March AAOI of the CTRL_NA simulation and the CTRL_O simulation would occur less often than 5 % if the distribution function of the March AAOI of the CTRL_NA run tended to larger values than the respective distribution function of the CTRL_O run. Thus a change of the NH albedo description and the consequently occurring feedbacks on sea ice and snow cover cause a change of the SH circulation. Nevertheless, this change does not seem to be stationary, as shown in Table 5.3 and Figure 5.24.

Table 5.2: Differences in winter (DJF) and March NAO, AO, and AAO. Kolmogorov-Smirnov distribution test statistics for the respective time coefficients. $\hat{F}(x)$ ($\hat{G}(x)$) represent the cumulative distribution function of the NAO, AO, or AAO index of the CTRL_O (CTRL_NA) run. For an explanation of D, Z, and P refer to section 3.3.

Atmospheric mode	season or month	Kolmogorov-Smirnov test statistic D	Z	P	Test of null hypothesis against alternative hypotheses
NAO	DJF	0.0702	0.0050	0.2530	$H_1 : \hat{F}(x) \neq \hat{G}(x)$
		0.0702	0.0050	0.1265	$H_3 : \hat{F}(x) < \hat{G}(x)$
	Mar	0.1053	0.0075	0.0207	$H_1 : \hat{F}(x) \neq \hat{G}(x)$
		0.1053	0.0075	0.0103	$H_3 : \hat{F}(x) < \hat{G}(x)$
AO	DJF	0.0627	0.0044	0.3790	$H_1 : \hat{F}(x) \neq \hat{G}(x)$
		0.0627	0.0044	0.1895	$H_3 : \hat{F}(x) < \hat{G}(x)$
	Mar	0.1303	0.0092	0.0019	$H_1 : \hat{F}(x) \neq \hat{G}(x)$
		0.1303	0.0092	0.0009	$H_3 : \hat{F}(x) < \hat{G}(x)$
AAO	DJF	0.0677	0.0048	0.2911	$H_1 : \hat{F}(x) \neq \hat{G}(x)$
		0.0677	0.0048	0.1456	$H_2 : \hat{F}(x) > \hat{G}(x)$
		0.0451	0.0032	0.3864	$H_3 : \hat{F}(x) < \hat{G}(x)$
	Mar	0.0852	0.0060	0.0977	$H_1 : \hat{F}(x) \neq \hat{G}(x)$
		0.0852	0.0060	0.0488	$H_3 : \hat{F}(x) < \hat{G}(x)$

Table 5.3: Differences in March AO and AAO for two sub-periods. Period I: year 1 to 200, period II: year 201 to 400. $\hat{F}(x)$ ($\hat{G}(x)$) represent the cumulative distribution function of the NAO, AO, or AAO index of the CTRL_O (CTRL_NA) run. For an explanation of D, Z, and P refer to section 3.3.

Atmospheric mode	Period	Kolmogorov-Smirnov test statistic D	Z	P	Test of null hypothesis against alternative hypotheses
AO	I	0.1550	0.0155	0.0131	$H_1 : \hat{F}(x) \neq \hat{G}(x)$
	II	0.1608	0.0161	0.0091	$H_1 : \hat{F}(x) \neq \hat{G}(x)$
AAO	I	0.125	0.0125	0.0734	$H_1 : \hat{F}(x) \neq \hat{G}(x)$
	II	0.085	0.0085	0.4101	$H_1 : \hat{F}(x) \neq \hat{G}(x)$

Table 5.4: Differences in DJF and March NAO, AO, and AAO principal components time series (asterisk denotes 10 % / 5 % / 1 % level of significance after applying a two sided t-test accounting for serial correlation). The time series were standardised with the standard deviation of the respective run from the original ECHAM4 albedo scheme.

Season or month	Difference: new - old albedo scheme		
	NAO	AO	AAO
DJF	-0.144^{*}	-0.113	-0.000
March	-0.205^{***}	-0.223^{***}	-0.137^{*}

Table 5.5: Correlation between DJF and March NAO, AO, and AAO time coefficients.

Season or month	Correlation of the indices of CRTL_O (CTRL_NA) between		
	AO and NAO	AO and AAO	NAO and AAO
DJF	0.850 (0.887)	0.036 (0.124)	-0.027 (0.138)
March	0.932 (0.937)	0.044 (-0.065)	0.025 (-0.085)

Concluding remarks

The increased meridional near surface air temperature (SAT) gradient causes circulation changes that project onto the negative phases of the AO/NAO. This is similar to the shift towards a positive AO phase in scenario experiments with increasing GHG concentrations leading to global warming with a polar amplification and hence to a decreased equator to pole SAT gradient. This goes along with decreased zonal flow in high latitudes.

5.5 Wind storm events

In the previous section 5.4 it was shown that differences in surface albedo parameterisations lead to changed mean states of the global circulation. The current section addresses the question as to whether besides the mean state circulation changes the probability of wind storm events on a regional scale is also changed.

Similar to the analysis of Fischer-Bruns et al. (2005) the direct model output of the wind speed maximum at 10 m height is used to calculate wind storm events instead of using any proxies for storm events. ECHO-G calculates the maximum wind speed at 10 m height for each grid cell within the integration time step of 30 minutes. For the use in this study the maximum of all 30 minute maximum wind speed events occurring within a 24 hour model day is used as a daily maximum value. In a simple peak-over-threshold count at each grid cell all wind storm events were summed up when they reached a threshold of 8 Bft. (gale) or 10 Bft. (storm), respectively.

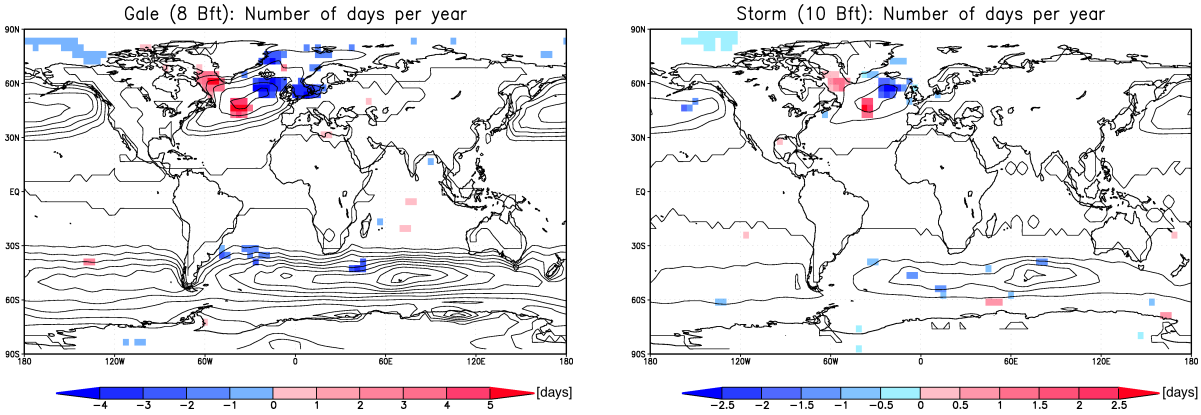

Figure 5.27: Occurence of wind storm events in number of days. Contour lines denote annual mean number of days exceeding a wind speed of 17.2 $\mathrm{m\,s^{-1}}$ (8 Bft., left) or 24.5 $\mathrm{m\,s^{-1}}$ (10 Bft., right) in the control run with unchanged albedo. Contour line interval is 20 days (left) and 10 days (right). Shaded areas denote the difference between the CTRL_NA and the CTRL_O run at the 1 % level of significance.

Figure 5.27 shows that the number of both gales and storms is increased in the Davis Strait and in the northern North Atlantic and reduced in the northern North Atlantic south of Iceland and in the North Sea (North Sea: gales only) when the new albedo scheme is applied. The changes in the North Atlantic region form a dipole pattern at the south-western and north-eastern boundary of that region with maximum wind storm events. This indicates a shift of the storm tracks over the North Atlantic towards south-west under colder Arctic climate conditions, a reduced sea ice cover around southern Greenland, and during a corresponding shift of the NAO towards its negative polarity. Whereas the increase in gale and storm days stems mainly from an increase in DJF (not shown), the decrease is distributed more equally over DJF and MAM, with a slightly stronger decrease in spring (not shown).

The rise of the 500 hPa geopotential height in DJF over the Icelandic region of the North Atlantic may explain the south-westwards deflection of storm tracks in the North Atlantic. The increase of wind storm events in the Davis Strait is accompanied by a decreased sea ice coverage, a large difference in heat release (up to 90 $\mathrm{W\,m^{-2}}$), and a decrease in SLP.

The dipole pattern of a reduced wind storm frequency in a region reaching from Iceland to the North Sea and an increased wind storm frequency in the North Atlantic agrees with the findings of Fischer-Bruns et al. (2005). Both the albedo runs and the results of Fischer-Bruns et al. (2005) indicate that a warmer climate in interaction with an increased T_{2m} gradient between the North Pole and the equator lead to a north-eastwards shift of the North Atlantic region of maximum wind storm frequency.

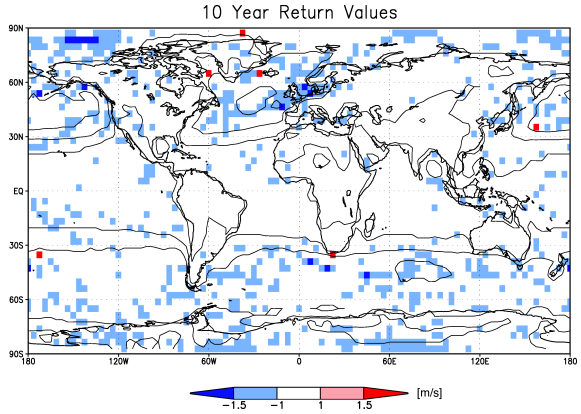

Figure 5.28: Differences in 10 year return values of 10 m wind speed (CTRL_NA minus CTRL_O). Contour lines denote the long-term mean maximum wind speed that occurs once in ten years within the CTRL_O run. Contour line interval 10 $\mathrm{m\,s^{-1}}$. Maximum values ($> 40\ \mathrm{m\,s^{-1}}$) can be seen in the North Atlantic, in the North Pacific, and in the Southern Ocean between South Africa and Australia. Shaded areas denote the difference between the CTRL_NA and the CTRL_O. No test of statistical significance was applied.

The effect of the changed surface albedo (and also the effect of all subsequent consequences (e.g. Arctic near surface air mass cooling, shift of the AO etc.)) on 10-year return values of maximum 10 m wind speeds of wind storm events is shown in Figure 5.28. Almost no increase in the wind speed which wind storm events exceed once in ten years can be seen. Instead, there is a tendency towards lower return values. Areas in which a decrease of 10-year return values by at least 1 $\mathrm{m\,s^{-1}}$ is evident are the North Sea and the western Arctic Ocean. This means, for example, that whereas in the CTRL_O simulation in the North Sea a grid cell mean 10-year return value of – say – 35 $\mathrm{m\,s^{-1}}$ occurs, this value is decreased to approx. 34 $\mathrm{m\,s^{-1}}$ in the CTRL_NA run.

Chapter 6

Paleoclimate and scenario simulations with the new albedo scheme

In chapter 5 it was shown that snow and sea ice parameterisation changes have great impacts on the atmospheric circulation and on the planetary scale energy distribution. The current chapter aims to address the question as to whether a changed albedo of the NH cryosphere affects the temporal evolution of selected climate key components when there is a climate change due to varying external forcings. A large amount of the inter-model spread of polar amplification strength is assumed to stem from different parameterisation of Arctic key processes (ACIA 2005). This includes, for example, the treatment of all relevant processes involved in the SAF, such as the sea ice and snow albedo.

The inclusion of melt ponds in an albedo parameterisation scheme strengthens the ice albedo feedback (Curry et al. 1995). In a climate change simulation an inclusion of melt ponds should therefore lead to a larger retreat of sea ice under global warming conditions. This should also increase the polar amplification of global warming due to the increase in SAF strength. Does the simulation with the improved sea ice albedo scheme show a higher rate of thinning and retreat of Arctic sea ice?

This chapter discusses briefly the following items with respect to the impact of a changed albedo scheme for the NH:

- Sea ice area evolution from 1500 to 2100.
- Polar amplification of global warming.
- Freshwater input into the polar cap oceans.

Addressing these issues gives a hint as to whether there is an impact of surface albedo conditions on the climate's sensitivity to climate change.

Another matter of discussion in this chapter is how the improved albedo scheme performs within ECHO-G in reproducing the present day sea ice coverage.

6.1 Comparison of simulated sea ice concentrations with NSIDC satellite data

The satellite data from the NSIDC (Cavalieri et al. 2005) used for comparison cover the period from January 1979 to December 2004. The complete data set starts from October 1978. The satellite data are available on an equidistant grid of 25 km grid size. The satellite-derived sea ice concentration used in this study is based on the NASA team algorithm to calculate the sea ice concentration from the measured microwave radiation. Prior to further analysis the satellite sea ice concentration was interpolated to the regular T30 (approx. 3.75° x 3.75°) grid of ECHO-G. A period of 26 years of satellite data includes at least two complete cycles of the sea ice concentration variability (10-year cycle as suggested and explained by physical reasons by Mysak and Venegas (1998)) and also covers twice the 10–12-year cycle of sea ice volume variability (Hilmer and Lemke 2000). To compare the modelled sea ice cover with the satellite measurements the modelled data of the transient runs are used because in terms of comparability the forced runs come closest to the real world as they include all relevant forcing and reproduce the observed thinning and retreating Arctic sea ice. Furthermore, due to the slightly warming trend of the control runs (CTRL_O and CTRL_NA) the use of the whole period of the control runs would include large periods that are warmer than the period of the forced runs (1978–2004). Hence in the control runs a systematic underestimation of NH sea ice cover would likely occur.

The new albedo scheme does not reduce the systematic overestimation of fractional sea ice cover in March in the Sea of Okhotsk and the Barents Sea. Additionally, its application in ECHO-G leads to a systematic underestimation of sea ice cover in March in the Davis Strait and Labrador Sea (Figure 6.1) with consequences for the atmospheric circulation in winter as described in chapter 5. However, from chapter 5 also discovers that the annual cycle in NH total sea ice extent and area matches observations better, both in minimum extent in late summer and maximum extent in late winter.

The simulation of the minimum fractional cover of sea ice in ECHO-G becomes much more realistic if the new albedo scheme is applied (Figure 6.1).

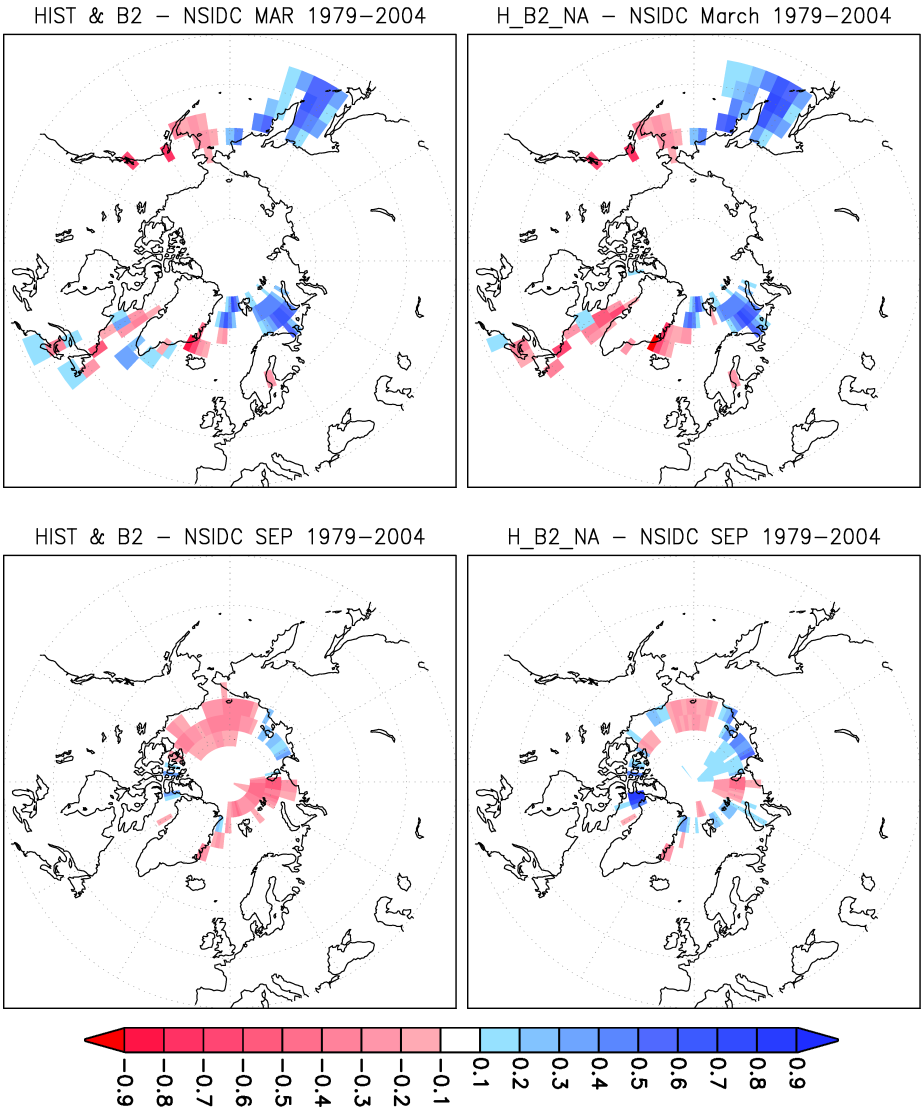

Figure 6.1: Difference in fractional sea ice cover: Simulated NH sea ice cover minus NSIDC data (1979–2004) for March (top) and September (bottom). Old albedo run left, new albedo run right.

6.2 Effects of the new albedo scheme under changing climate conditions

6.2.1 Arctic and global near surface air temperature evolution

Figure 3.3 shows amongst others the temporal evolution of the global annual mean temperature from 1500 to 2100 as simulated with ECHO-G using the original ECHAM4 and the new Køltzow et al. (2003) albedo scheme. There are two pronounced minima in the curves of the global annual mean T_{2m}: The Late Maunder Minimum (LMM) (approx. 1675–1705) and the Dalton Minimum (DM) (approx. 1790–1830). The LMM and the DM differ slightly in their origins. During both LMM and DM the solar irradiance was reduced (e.g. Lean et al. 1995). During the DM also strong volcanic eruptions occurred

which are largely responsible for the global temperature drop in this period (Wagner and Zorita 2005). However, in the external forcing data set for ECHO-G both colder climate periods are represented by nothing more than the so-called effective solar constant (Figure 3.4). For these simulation runs (HIST & B2 and H_B2_NA) ECHO-G was forced with forcing data from reconstructions and from the IPCC SRES B2 future scenario. For a detailed description of the forcing data refer to section 3.2.1.

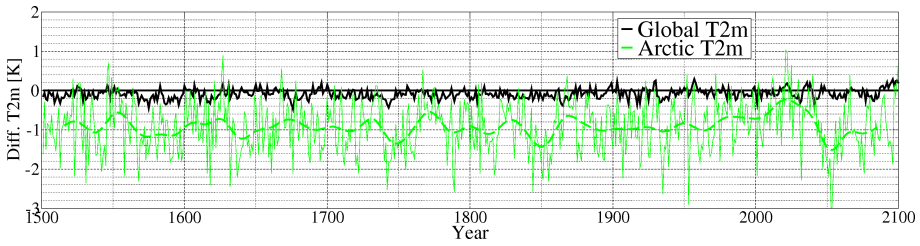

Figure 6.2: Difference in global and Arctic annual mean T_{2m} (H_B2_NA - (HIST & B2)). Hatched line denotes 30 year low pass filtered Arctic T_{2m} differences.

The impact of the albedo scheme on the global and Arctic annual mean T_{2m} is shown in Figure 6.2. Apart from the large interannual and decadal scale climate variability in the Arctic no systematic increase or decrease in the cooling effect of the new albedo scheme on the Arctic climate under warmer or colder Arctic and global climate conditions is evident.

6.2.2 Polar amplification of global warming

Figure 6.3 a) might even give the impression that the polar amplification of global warming in ECHO-G with the new scheme is reduced. This would be contrary to the assumption of Curry et al. (1995) that the inclusion of melt ponds in an sea ice albedo scheme strengthens the ice albedo feedback. A strengthened SAF in polar regions would increase the amount of polar amplification of global warming as it enhances the climate sensitivity of a model. However, the result of the same analysis for the polar amplification applied to a period that is shifted back 20 years shows no change in polar amplification of global warming with respect to the albedo scheme or the IPCC SRES emission scenario (Figure 6.3 b)). The differences between Figure 6.3 a) and b) in Arctic latitudes are primarily caused by the very large decadal scale variability of the Arctic climate.

To draw a conclusion from Figure 6.3, neither the chosen GHG emission scenario nor the choice of the sea ice and snow albedo parameterisation specified in the present study and the resulting mean sea ice thickness have an influence on the simulated polar amplification. This is even more true if the results from Figure 6.3 are compared with the inter-model spread of polar amplification of 17 models participating in the forthcoming AR4 of IPCC (Figure 1.1). The magnitude of the polar warming of those 17 models was 1.5 to 4 times that of their global warming. The unaffected climate sensitivity of ECHO-G by the chosen cryosphere albedo scheme is in accordance with the findings of Knutti et al. (2006)

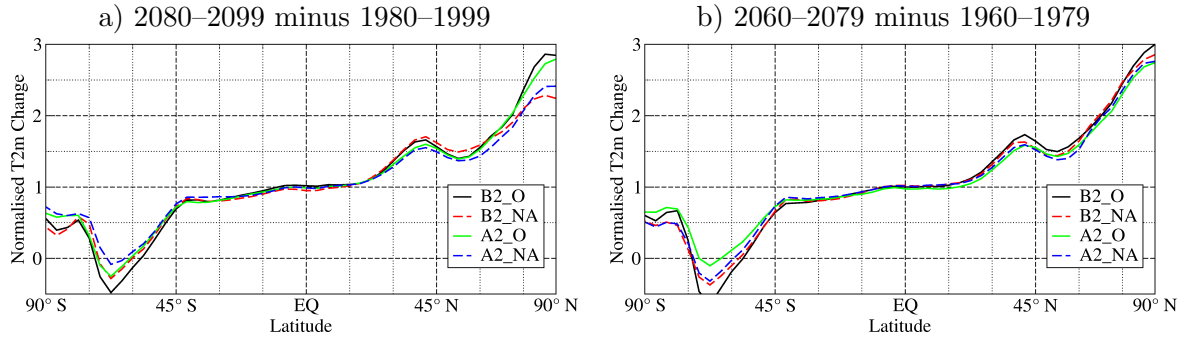

Figure 6.3: Polar amplification of global warming. y-axis denotes the ratio between the change in zonal mean temperature and the increase in global mean temperature. The temperature change is computed a) as the 2080–2099 average minus the 1980–1999 average, b) as the 2060–2079 average minus the 1960–1979 average. Solid lines denote the computed change of the runs with the original ECHO-G parameterisations (B2_O and A2_O), hatched lines the change of the new albedo scheme runs (B2_NA and A2_NA). "A2" or "B2" denote the respective IPCC emission scenario, "O" or "NA" original or new albedo run, respectively.

who attributed regional climate sensitivity of a model to its regional seasonal cycle in T_{2m}. As shown in section 5.3 there is no statistically significant difference between the seasonal cycle of the Pan-Arctic T_{2m} in the CTRL_NA and the CTRL_O run. Thus no changed regional (i.e. Arctic) climate sensitivity could be expected. Therefore the polar amplification of global warming remained unchanged.

6.2.3 Sea ice

As already shown in Figure 5.6 the greatest differences between the runs with new and old albedo scheme in the NH sea ice coverage occur in September. Figure 6.4 shows the evolution of the minimum and the maximum NH sea ice coverage from 1500 to 2100. In spite of the evident differences in the fractional sea ice coverage pattern between the new and old albedo scheme simulations (Figure 5.2), the temporal evolution of the NH sea ice covered area in March is almost identical under all combinations of forcings and the albedo scheme (Figure 6.4).

In September both new and old scheme simulation show a rapid decrease of the total NH sea ice covered area under warming climate conditions, especially under the IPCC SRES A2 GHG emission scenario. The A2 simulation, using the original albedo scheme, loses almost all Arctic sea ice in summer by the end of the 21st century. Although in the context of a shrinking Arctic sea ice cover in summer the integrated effect of the changed albedo scheme is evanescent (if no sea ice is left, even a different sea ice albedo scheme cannot lead to a different albedo), even in the A2 scenario runs at the end of the 21st century the respective albedo scheme runs can be clearly separated from each other (Figure 6.4).

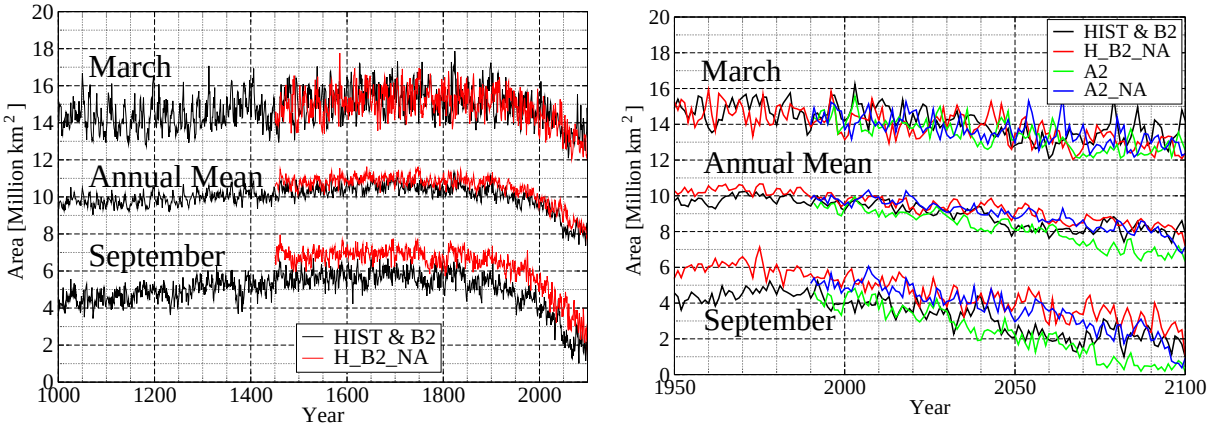

Figure 6.4: Temporal evolution of NH sea ice covered area from 1000 to 2100 under paleoclimate forcing conditions according to section 3.2.1 and IPCC SRES B2 GHG emission scenarios, right figure: additionally IPCC SRES A2 GHG emission scenarios.

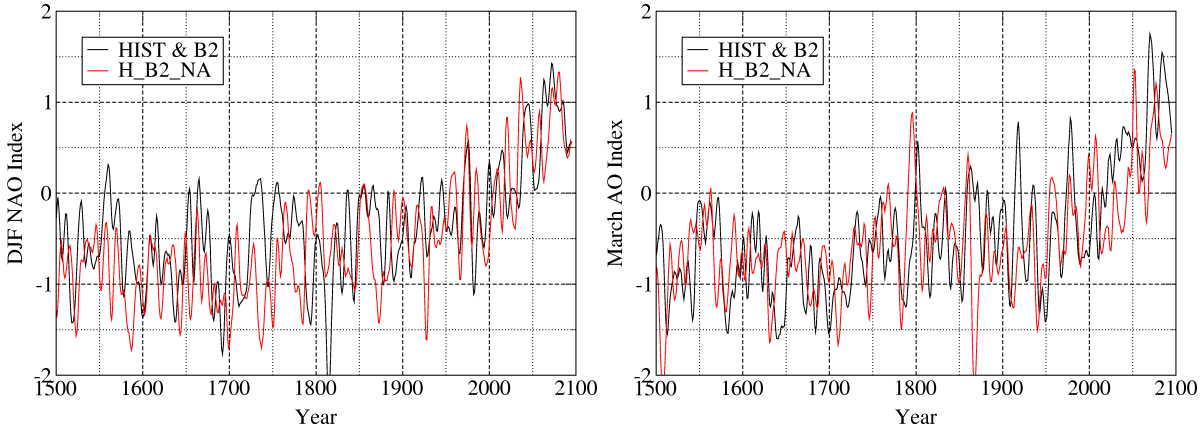

Figure 6.5: Temporal evolution of DJF NAO index and March AO index (30 years low pass filtered) from 1500 to 2100 under paleoclimate forcing conditions according to section 3.2.1 and IPCC SRES B2 GHG emission scenarios. The time coefficients of the AO and NAO were obtained by projecting the SLP anomaly patterns onto the respective leading EOF pattern of the CTRL_O run. Here, "SLP anomaly" means the SLP difference from the respective mean SLP of the CTRL_O run.

6.2.4 NAO and AO

In the simulations with ECHO-G the polarity of the AO and the NAO increase as GHG concentrations increase (Figure 6.5). Also the majority of currently used coupled climate models show a trend towards a positive phase of the AO under increasing GHG concentrations (Stephenson et al. 2006). The temporal evolutions of the respective time coefficients are indistinguishable between the new and old albedo simulation runs. This is shown exemplarily for the DJF NAO and the March AO under paleoclimate and IPCC SRES B2 forcing conditions in Figure 6.5. The effect of changing external forcing conditions, in particular, increasing GHG concentrations, clearly dominate the small effect of the different snow and sea ice albedo on the atmospheric modes.

6.2.5 Freshwater input into the polar cap oceans

Under global climate warming conditions an increasing freshwater input into the polar cap seas is expected. Both new and old albedo scheme forced simulations reproduce the observed (Peterson et al. 2002) positive trend of river discharge into the Arctic Ocean throughout the last 65 years of the 20th century (Figure 6.6). Wu et al. (2005) attributed the observed increase in Arctic river discharge to human influence.

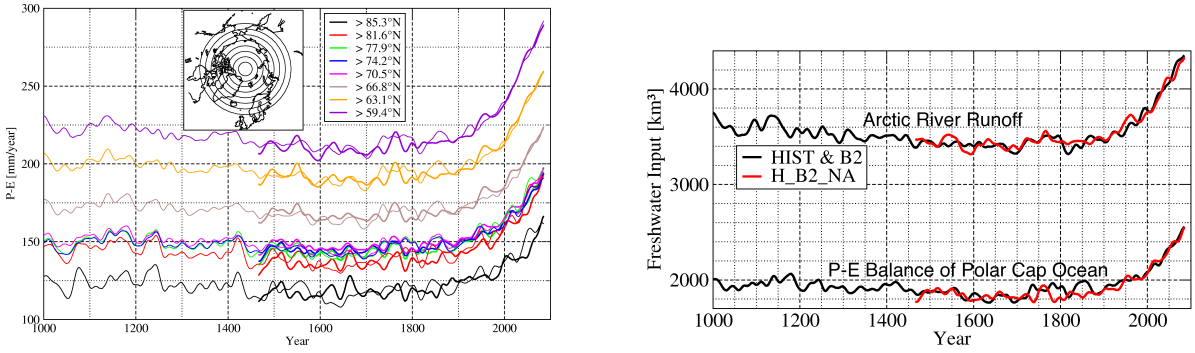

Figure 6.6: Temporal evolution of circumpolar annual mean P-E (left) and freshwater input into polar cap seas (right). Historical forcing and IPCC SRES B2 scenarios runs with ECHO-G. Left: thick lines denote the run with the new albedo scheme, thin lines denote the run with the original ECHAM4 scheme, right: red lines denote the run with the new albedo scheme, black lines denote the run with the original ECHAM4 scheme.

Figure 6.6 shows that the temporal evolution of the freshwater input into the polar cap seas simulated with the new scheme is indistinguishable from the evolution of simulated fresh water input using the original scheme. This statement is also valid for the precipitation minus evaporation (P-E) balance as well as for the river discharge into the polar cap seas.

The temporal evolution of the difference of the runoff into oceans north of 66.8° N within the annual cycle is shown in Figure 6.7. In agreement with the trend towards higher near surface air temperatures under increasing GHG concentrations by the end of the 21st century, a threshold of, for example, 40000 $m^3\,s^{-1}$ runoff is reached earlier and undercut later within the annual cycle. This occurs as the melt season of snow is prolonged.

The influence of the new snow albedo scheme on the snow melt (cf. Figure 5.1) is also visible in Figure 6.7 as a shift towards a retarded runoff within the annual cycle compared with the simulation runs with the original snow albedo scheme. Under global warming conditions the runoff peak is shifted towards spring. Therefore, also the maximum negative and positive differences between the runs with the new and the old scheme occur earlier within the calendar year.

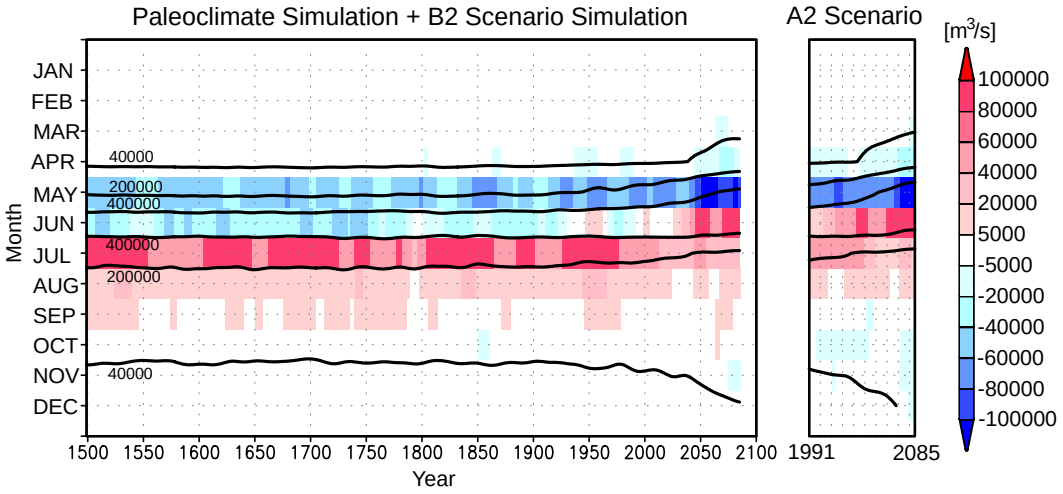

Figure 6.7: Hovmöller diagram of the monthly mean runoff into polar cap oceans (oceans north of 66.8° N), filtered by a 30-year low pass filter. Thick black contour lines denote runoff in $m^3\,s^{-1}$ of the HIST & B2 and the A2_O run, respectively. Shaded areas denote the difference H_B2_NA minus HIST & B2 and A2_NA minus A2_O, respectively.

Chapter 7

Conclusions

By performing experiments with the AOGCM ECHO-G a link between slightly changed physical parameterisations and local Arctic climate changes as well as remote atmospheric circulation changes could be established.

As an example for changed physical parameterisations the description of the sea ice and snow albedo in the Northern Hemisphere (NH) was chosen. The original sea ice and snow albedo scheme of ECHO-G was replaced by an improved scheme. In simulations with constant present day climate conditions the reaction of the climate system to changed NH cryospheric albedo conditions was studied. Simulations using varying external forcings such as GHG concentration changes provided further insight into the influence of NH sea ice and snow albedo schemes under global climate change situations.

Under prescribed identical surface temperature conditions the new sea ice and snow albedo scheme leads to a lower annual mean amount of absorbed solar radiation than the original scheme. Implemented in an AOGCM a changed cryosphere albedo itself alters the mean state of surface temperature conditions and the probability of snow and ice presence. This happens as an effect of the surface albedo feedback (SAF). Consequently, in all simulations under each climate condition the new albedo scheme results in a prolongated snow cover, thicker sea ice, colder Arctic and global temperatures, and a greater minimum extent of NH sea ice cover within the annual cycle. Moreover, the decreased annual cycle of NH sea ice extent compares better to the observational record.

The surface albedo changes are transformed into planetary albedo changes without being substantially influenced by cloud cover effects. As the existing radiation deficit in high latitudes increases, the role of the Arctic as a sink in the global energy budget is increased. The thickened Arctic sea ice prevents an increase of heat flux from the surface to the atmosphere in high Arctic latitudes. Thus the increase in Arctic radiation deficit is balanced by an increase of energy transport through the lateral boundaries of the Arctic atmosphere.

In accordance with the increased radiation budget deficit in the Arctic, the global T_{2m} decrease is amplified in NH high latitudes and maximum near the North Pole. Thus it leads to an increased meridional gradient in T_{2m} (especially in autumn). The effect of the NH albedo change on the absorbed solar radiation is maximum in summer. Hence the seasonal cycle in absorbed solar radiation is decreased in the Arctic. Because the thicker sea ice also reduces the heat flux from the Arctic Ocean to the atmosphere in autumn and winter, the seasonal cycle in T_{2m} is not changed. According to Knutti et al. (2006) it follows that regional climate sensitivity in the Arctic is not changed.

As a further result of the changed NH cryospheric albedo, a generally cooler tropical upper troposphere and a warmer Arctic stratosphere (in winter and especially in early spring) occur. The warming of the Arctic stratosphere generates a reduced meridional temperature gradient between Arctic and tropical latitudes along each pressure level intersecting the tropopause. In accordance with a mechanism proposed by Shindell et al. (1999) this decreased meridional gradient along these pressure levels causes a shift of the polar vortex and the AO phase towards their negative polarity. Consequently, the zonal mean zonal wind speed in midlatitudes is decreased throughout all atmospheric levels.

Atmospheric circulation changes may also explain the decrease in sea ice cover in the seas around southern Greenland in winter and spring which cannot be explained alone as a locally direct thermodynamic response to the changed (and generally increased) sea ice albedo. An increased sea level pressure (SLP) gradient from northern Greenland to the Nordic Seas decreases the Fram Strait sea ice export. In combination with a shift of the NAO towards its negative phase this leads to higher mean temperatures around southern Greenland. Thus the southern Greenland sea ice cover is highly sensitive to large scale and regional atmospheric circulation changes.

Circulation changes initially caused by NH sea ice and snow albedo changes and the consequently occurring changes in sea ice and snow coverage are greatest in boreal late winter and early spring. Therefore, an analysis on a monthly time scale is necessary to identify large circulation changes. In the typical approach of using seasonal means these effects would have been smeared out as there are only small changes in early winter. The finding that changes in the free atmosphere are larger in the late winter circulation of the NH than in early winter is in accordance with the reanalysis data derived findings of Hu et al. (2005), even if the causes of the processes that drive theses changes (probably GHG increase or also internal variability in the observations and NH cryosphere albedo changes in the simulations) differ.

The polar vortex plays a dominant role in generating the circulation changes described above. In autumn when the changes in zonal mean near surface air temperature are maximum, almost no significant circulation changes occur. The changing of the mean

state of stratospheric temperatures starts as soon as the polar vortex is established in the winter season.

Even slight changes in Arctic process parameterisation have impacts on the extra-tropical circulation in the atmosphere of the Southern Hemisphere (SH). The largest changes in the SH circulation occur in March and April. During these months atmospheric circulation changes are maximum in both hemispheres, including zonally averaged zonal wind speed changes occurring in a pattern that is symmetric to the equator. This statement is valid for the changed mean state of the circulation. For individual events within the same climate realisation (i.e. within the same simulation run), however, no correlation between NH and SH circulation anomalies could be identified.

Using results from scenario simulations with increasing GHG concentrations it was shown that NH cryospheric albedo changes and GHG changes create similar difference patterns in the Arctic troposphere and stratosphere in various variables. The timing of the differences within the annual cycle is also almost identical and thus similar to the findings of Hu et al. (2005) who found strongest trends in late winter. In a practical sense this may hamper the attribution of circulation changes to direct radiative effects of the increasing concentrations of well-mixed GHGs on the one hand, and to secondary effects of GHG induced warming changes like sea ice and snow cover reduction on the other.

The same argument is valid concerning the strength of the polar vortex. It was shown that ozone depletion is not necessary to increase the boreal winter cooling and therefore the strength of the polar vortex. Instead, dynamical heating is sufficient to alter the strength. Both GHG changes and surface albedo changes cause a changed meridional temperature gradient between the Arctic stratosphere and the tropical upper troposphere along fixed pressure levels. In both cases a reduced NH albedo is accompanied by a warmer Arctic stratosphere and the differences in the Arctic stratosphere temperature are maximum in boreal early spring. Thus surface albedo and GHG changes may alter the polarity of the AO for the same dynamical reason.

The changes in the phase of the AO and the temperature of the Arctic stratosphere which are caused by a different sea ice and snow albedo scheme are approximately one order of magnitude smaller than those arising from the increase in GHG concentrations until the end of the 21st century. The NH surface albedo and sea ice concentration and thickness changes under increasing GHG concentrations are also much greater than those stemming from surface albedo changes of the NH cryosphere under unchanged GHG concentrations. Thus their individual and absolute influence on the atmospheric circulation can also be assumed to be increased. Therefore, secondary effects of GHG concentration increase, such as albedo and sea ice decrease, may play a contributing role in evoking the pronounced cooling of the Arctic stratosphere in March. Nevertheless, for all seasons other than winter or early spring and for all regions other than the Arctic,

sea ice and surface albedo changes probably do not enhance the radiative cooling effect of well-mixed GHGs on stratospheric temperature.

As mentioned above, a changed NH cryosphere albedo results in a changed mean state of NH sea ice cover and thickness. Neither the changed mean state of the sea ice nor the changed parameterisation of the surface albedo relevant processes changed the rate of sea ice cover reduction or the polar amplification of global warming in the scenario runs with ECHO-G which is in contradiction to the results of Holland and Bitz (2003) and Hall and Qu (2006). This is an important finding because a large amount of the inter-model spread in simulating polar amplification of global warming is assumed to stem from a different SAF strength. The difference in the SAF strength itself is caused, to a large extent, by the different snow and sea ice albedo parameterisation schemes in different climate models.

The findings of this study suggest that further work on the field of the study would be fruitful. Simulations with either a changed sea ice or snow albedo would allow separation of the relative influence of sea ice or snow, respectively, on the discussed circulation changes. A more detailed view into the physical processes which drive the change in the polarity of the AO and the zonal mean flow as a direct response to changes in the surface energy budget would be desirable. Moreover, a detailed analysis on the physical causes of atmospheric circulation changes should also include a closer look into the causes of the SH circulation changes which occur as a response to the NH energy budget and circulation changes. In addition, the choice of a more pronounced difference between the original and a changed NH cryosphere albedo is assumed to change the regional climate sensitivity. This would allow the question to be addressed as to what extent the choice of a certain sea ice and snow albedo scheme would affect the polar amplification of global warming.

An interesting issue remains the question as to whether a simulation with an aqua-planet set-up under GHG concentration changes would also show greatest changes in the temperature of the Arctic stratosphere in March. Addressing this issue would clarify the role of the NH cryosphere in circulation changes and stratospheric temperature changes under increasing GHG concentrations.

List of Figures

List of Tables

List of Abbreviations

Abbreviation	Explanation
A05	Identifier of a 1000-year control run of ECHO-G (present day forcing conditions), run performed by S. Legutke from MPIM
A2_NA	A2 scenario run with ECHO-G using the new albedo scheme
A2_O	A2 scenario run with ECHO-G using the original ECHAM4 albedo scheme, performed by F. González-Rouco
AAO	Antarctic Oscillation
AO	Arctic Oscillation
AOGCM	Atmosphere-Ocean General Circulation Model
AR4	IPCC Forth Assessment Report
AVHRR	Advanced Very High Resolution Radiometer (Satellite Data)
CTRL_NA	ECHO-G control run with present day forcing conditions and a new snow and ice albedo scheme
CTRL_O	ECHO-G control run with present day forcing conditions and original ECHAM4 snow and ice albedo scheme
DJF	December January February (meteor. winter)
DKRZ	Deutsches Klimarechenzentrum (The German High Performance Computing Centre for Climate- and Earth System Research)
DM	Dalton Minimum
ECHAM4	Atmosphere Model: 4^{th} generation of the ECHAM model family from MPIM, Hamburg, Germany
ECHO-G	AOGCM consisting of ECHAM4 (Atmosphere Model) and HOPE-G (Ocean Model)
ECMWF	European Centre for Medium-Range Weather Forecasts
ENSO	El Niño – Southern Oscillation
EOF	Empirical Orthogonal Function
GHG	Greenhouse Gas
GISS	NASA Goddard Institute for Space Studies

GLIMPSE	Global Implications of Arctic Climate Processes and Feedbacks (5^{th} EU framework project)
H_B2_NA	Historical and B2 scenario run with ECHO-G (new albedo)
HIRHAM	A regional climate model that uses the physical parameterisation packages of ECHAM4
HIST & B2	Historical and B2 scenario run with ECHO-G using the original ECHAM4 albedo scheme, performed by F. González-Rouco
HR	Data set of historically reconstructed forcings
iid	independent and identically distributed
IPCC	Intergovernmental Panel on Climate Change
ISCCP	International Satellite Cloud Climatology Project
JJA	June July August (meteor. summer)
LGM	Last Glacial Maximum
LLM	Late Maunder Minimum
MAM	March April May (meteor. spring)
MPIM	Max-Planck-Institut für Meteorologie, Hamburg
MOC	Meridional Overturning Circulation
MSE	Moist Static Energy
NAM	Northern Annular Mode (Synonym to AO)
NAO	North Atlantic Oscillation
NAOI	North Atlantic Oscillation Index
NASA	National Aeronautics and Space Administration
NCEP	National Centers for Environmental Prediction
NH	Northern Hemisphere / Northern Hemispheric
NSIDC	National Snow and Ice Data Center, Boulder, Colorado, USA
SAF	Surface Albedo Feedback
SAT	Surface Air Temperature
SH	Southern Hemisphere / Southern Hemispheric
SHEBA	Surface Heat Budget of the Arctic Ocean
SLP	Mean Sea Level Air Pressure
SON	September October November (meteor. autumn)
SRES	IPCC Special Report on Emission Scenarios
T_{2m}	Near Surface Air Temperature (in 2 m height)
TAR	IPCC Third Assessment Report
THC	Thermohaline Circulation
TOA	Top Of Atmosphere

References

ACIA (2005). Arctic climate impact assessment. *Cambridge University Press*, 1042 p.

Alexander, M. A., U. S. Bhatt, J. E. Walsh, M. S. Timlin, J. S. Miller, and J. D. Scott (2004). The Atmospheric Response to Realistic Arctic Sea Ice Anomalies in an AGCM During Winter. *J. Climate 17*, 890–905.

Ambaum, M. H. P., B. J. Hoskins, and D. B. Stephenson (2001). Arctic Oscillation or North Atlantic Oscillation? *J. Climate 14*, 3495–3507.

Arfeuille, G., L. A. Mysak, and L. B. Tremblay (2000). Simulation of the interannual variability of the wind-driven Arctic sea-ice cover during 1958-1998. *Clim. Dyn. 16*, 107–121, doi:10.1007/PL00013732.

Baldwin, M. P. and T. J. Dunkerton (1998). Quasi-biennial modulation of the southern hemisphere stratospheric polar vortex. *Geophys. Res. Lett. 25*, 3343–3346, doi:10.1029/98GL02445.

Baldwin, M. P. and T. J. Dunkerton (1999). Propagation of the Arctic Oscillation from the stratosphere to the troposphere. *J. Geophys. Res. 104*(D24), 30937–30946.

Bard, E., G. Raisbeck, F. Yiou, and J. Jouzel (2000). Solar irradiance during the last 1200 years based on cosmogenic nuclides. *Tellus 52B*, 985–992, doi:10.1034/j.1600–0889.2000.d01–7.x.

Bengtsson, L., V. A. Semenov, and O. M. Johannessen (2004). The Early Twentieth-Century Warming in the Arctic: A Possible Mechanism. *J. Climate 17*, 4045–4057.

Bitz, C. M. and G. H. Roe (2004). A Mechanism for the High Rate of Sea Ice Thinning in the Arctic Ocean. *J. Climate 17*, 3623–3632.

Blunier, T., J. Chappellaz, J. Schwander, B. Stauffer, and D. Raynaud (1995). Variations in atmospheric methane concentration during the holocene epoch. *Nature 374*, 46–49, doi:10.1038/374046a0.

Bony, S., et al. (2006). How Well do we Understand and Evaluate Climate Change Feedback Processes? *J. Climate 19*, 3445–3482, doi:10.1175/JCLI3819.1.

Brown, R. D. (2000). Northern Hemisphere Snow Cover Variability and Change, 1915-97. *J. Climate 13*, 2339–2355.

Bryden, H. L., H. R. Longworth, and S. A. Cunningham (2005). Slowing of the Atlantic meridional overturning circulation at 25 degrees N. *Nature 438*, 655–657, doi:10.1038/nature04385.

Cai, M. (2006). Dynamical greenhouse-plus feedback and polar warming amplification. Part I: A dry radiative-transportive climate model. *Clim. Dyn. 26*, 661–675, doi:10.1007/s00382–005–0104–6.

Camp, C. D. and K.-K. Tung (2007). Stratospheric polar warming by ENSO in winter: A statistical study. *Geophys. Res. Lett. 34*, L04809, doi:10.1029/2006GL028521.

Cavalieri, D., C. Parkinson, G. P., and H. J. Zwally (1996, updated 2005). *Sea ice concentrations from Nimbus-7 SMMR and DMSP SSM/I passive microwave data*, January 1979 to December 2004. Boulder, CO, USA: National Snow and Ice Data Center. Digital media.

Cavalieri, D. J., C. L. Parkinson, and K. Y. Vinnikov (2003). 30-year satellite record reveals contrasting Arctic and Antarctic decadal sea ice variability. *Geophys. Res. Lett. 30*, 1970, doi:10.1029/2003/GL018031.

Corti, S., F. Molteni, and T. N. Palmer (1999). Signature of recent climate change in frequencies of natural atmospheric circulation regimes. *Nature 398*, 799–802, doi:10.1038/19745.

Crowley, T. J. (2000). Causes of climate change over the past 1000 years. *Science 289*, 270–277, doi:10.1126/science.289.5477.270.

Curry, J. A., W. B. Rossow, D. Randall, and J. L. Schramm (1996). Overview of Arctic Cloud and Radiation Characteristics. *J. Climate 9*, 1731–1764.

Curry, J. A., J. L. Schramm, and E. E. Ebert (1995). Sea Ice-Albedo Climate Feedback Mechanism. *J. Climate 8*, 240–247.

Curry, J. A., J. L. Schramm, D. K. Perovich, and J. O. Pinto (2001). Applications of SHEBA/FIRE data to evaluation of snow/ice albedo parameterizations. *J. Geophys. Res. 106*(D14), 15345–15356, doi:10.1029/2000JD900311.

Curry, J. A., J. L. Schramm, and M. C. Serreze (1995). Water-vapor feedback over the Arctic Ocean. *J. Geophys. Res. 100*(D7), 14223–14229, doi:10.1029/95JD00824.

Delworth, T. L. and T. R. Knutson (2000). Simulation of early 20th century global warming. *Science 287*, 2246–2250, doi: 10.1126/science.287.5461.2246.

Deser, C., J. E. Walsh, and M. S. Timlin (2000). Arctic Sea Ice Variability in the Context of Recent Atmospheric Circulation Trends. *J. Climate 13*, 617–633.

Dethloff, K., et al. (2006). A dynamical link between the Arctic and the global climate system. *Geophys. Res. Lett. 33*, L03703, doi:10.1029/2005GL025245.

ECMWF/DWD/DKRZ (2006). ECMWF Re-Analysis ERA-40 data. January 1958 to December 2001, Deutsches Klimarechenzentrum Hamburg, Germany.

Etheridge, D. M., L. P. Steele, R. L. Langenfelds, R. J. Francey, J. M. Barnola, and V. I. Morgan (1996). Natural and anthropogenic changes in atmospheric CO2 over the last 1000 years from air in Antarctic ice and firn. *J. Geophys. Res. 101*(D2), 4115–4128, doi:10.1029/95JD03410.

Fischer-Bruns, I., H. von Storch, J. F. Gonzalez-Rouco, and E. Zorita (2005). Modelling the variability of midlatitude storm activity on decadal to century time scales. *Clim. Dyn. 25*, 461–476, doi:10.1007/s00382–005–0036–1.

González-Rouco, F., H. von Storch, and E. Zorita (2003). Deep soil temperature as proxy for surface air-temperature in a coupled model simulation of the last thousand years. *Geophys. Res. Lett. 30*, 2116, doi:10.1029/2002GL016635.

Grenfell, T. C. and D. K. Perovich (1984). Spectral albedos of sea ice and incident solar irradiance in the southern Beaufort Sea. *J. Geophys. Res. 89*(NC3), 3573–3580.

Grenfell, T. C., S. G. Warren, and M. P. C. (1994). Reflection of solar radiation by the Antarctic snow surface at ultraviolet, visible, and near-infrared wavelenghts. *J. Geophys. Res. 99*(D9), 18669–18684, doi:10.1029/94JD01484.

Grötzner, A., R. Sausen, and M. Clausen (1996). The impact of sub-grid scale sea-ice inhogenities on the performance of the atmospheric general circulation model ECHAM3. *Clim. Dyn. 12*, 477–496, doi:10.1007/s003820050122.

Hall, A. (2004). The Role of Surface Albedo Feedback in Climate. *J. Climate 17*, 1550–1568.

Hall, A., A. Clement, D. W. J. Thompson, A. Broccoli, and C. Jackson (2005). The Importance of Atmospheric Dynamics in the Northern Hemisphere Wintertime Climate Response to Changes in the Earth's Orbit. *J. Climate 18*, 1315–1325, doi:10.1175/JCLI3327.1.

Hall, A. and X. Qu (2006). Using the current seasonal cycle to constrain snow albedo feedback in future climate change. *Geophys. Res. Lett. 33*, L03502, doi:10.1029/2005GL025244.

Hansen, J. and L. Nazarenko (2004). Soot climate forcing via snow and ice albedos. *Proc. Natl. Acad. Sci. 101*, 423–428, doi:10.1073/pnas.2237157100.

Hansen, J., et al. (2005). Efficacy of climate forcings. *J. Geophys. Res. 110*(D18), D18104, doi:10.1029/2005JD005776.

Hibler, W. D. (1979). Dynamic thermodynamic sea ice model. *J. Phys. Ocean. 9*, 815–846.

Hilmer, M. and P. Lemke (2000). On the decrease of Arctic sea ice volume. *Geophys. Res. Lett. 27*, 3751–3754, doi:10.1029/2000GL011403.

Hilmer, R., M. Harder, and P. Lemke (1998). Sea ice transport: A highly variable link between Arctic and North Atlantic. *Geophys. Res. Lett. 25*, 3359–3362, doi:10.1029/98GL52360.

Holland, M. M. and C. M. Bitz (2003). Polar amplification of climate change in coupled models. *Clim. Dyn. 21*, 221–232, doi:10.1007/s00382–003–0332–6.

Holland, M. M., C. M. Bitz, and B. Tremblay (2006). Future abrupt reductions in the summer Arctic sea ice. *Geophys. Res. Lett. 33*, L23503, doi:10.1029/2006GL028024.

Hu, Y. Y., K. K. Tung, and J. P. Liu (2005). A Closer Comparison of Early and Late-Winter Atmospheric Trends in the Northern Hemisphere. *J. Climate 18*, 3204–3216, doi:10.1175/JCLI3468.1.

Hurrell, J. W. (1995). Decadal trends in the North Atlantic Oscillation: Regional temperatures and precipitation. *Science 269*, 676–679, doi:10.1126/science.269.5224.676.

IPCC (2000). Special Report on Emissions Scenarios: A Special Report of Working Group III of the Intergovernmental Panel on Climate Change [Nakicenovic, N. and Swart, R. (eds.)]. *Cambridge University Press*, Cambridge, United Kingdom and New York, NY, USA, 612 pp.

IPCC (2001). Climate Change 2001: The Scientific Basis. Contribution of working group I to the Third Assessment Report of the Intergovernmental Panel on Climate Change [Houghton, J. T., Y. Ding, D. J. Griggs, M. Noguer, P. J. van der Linden, X. Dai, K. Maskell, and C. A. Johnson (eds.)]. *Cambridge University Press*, Cambridge, United Kingdom and New York, NY, USA, 881 pp.

Johannessen, O. M., E. V. Shalina, and M. W. Miles (1999). Satellite evidence for an Arctic sea ice cover in transformation. *Science 286*, 1937–1939, doi:10.1126/science.286.5446.1937.

Johannessen, O. M., et al. (2004). Arctic climate change: Observed and modelled temperature and sea-ice variability. *Tellus 56A*, 328–341, doi:10.1111/j.1600–0870.2004.00060.x.

Kim, P. J. and R. I. Jennrich (1973). Tables of the exact sampling distribution of the two sample Kolmogorov-Smirnov criterion. in:. *Selected Tables in Mathematical Statistics, Vol. 1.*, H. L. Harter and D. B. Owen, eds. Providence, Rhode Island: American Mathematical Society. 80–129.

Knutti, R., G. A. Meehl, M. R. Allen, and D. A. Stainforth (2006). Constraining Climate Sensitivity from the Seasonal Cycle in Surface Temperature. *J. Climate 19*, 4224–4233, doi:10.1175/JCLI3865.1.

Koenigk, T., U. Mikolajewicz, H. Haak, and J. Jungclaus (2006). Variability of Fram Strait sea ice export: Causes, impacts and feedbacks in a coupled climate model. *Clim. Dyn. 26*, 17–34, doi:10.1007/s00382–005–0060–1.

Kokhanovsky, A. A. and E. P. Zege (2004). Scattering optics of snow. *Appl. Opt. 43*, 1589–1602.

Køltzow, M., S. Eastwood, and J. E. Haugen (2003). Parameterization of snow and sea ice albedo in climate models. *Research Report no. 149*, Norwegian Meteorological Institute.

Krinner, G., O. Boucher, and Y. Balkanski (2006). Ice-free glacial northern asia due to dust deposition on snow. *Clim. Dyn. 27*, 613–625, doi:10.1007/s00382–006–0159–z.

Kwok, R. and D. A. Rothrock (1999). Variability of Fram Strait ice flux and North Atlantic Oscillation. *J. Geophys. Res. 104*(C3), 5177–5189, doi:10.1029/1998JC900103.

Langematz, U. and M. Kunze (2006). An uptdate on dynamical changes in the Arctic and Antarctic stratospheric polar vortices. *Clim. Dyn. 27*, doi:10.1007/s00382–006–0156–2.

Langematz, U., M. Kunze, K. Kruger, K. Labitzke, and G. L. Roff (2003). Thermal and dynamical changes of the stratosphere since 1979 and their link to ozone and CO2 changes. *J. Geophys. Res. 108*(D1), 4027, doi:10.1029/2002JD002069.

Langleben, M. P. (1969). Albedo and degree of puddling of a melting cover of sea ice. *J. Glaciology 8*, 407–412.

Lean, J., J. Beer, and R. Bradley (1995). Reconstruction of solar irradiance since 1610: Implications for climate change. *Geophys. Res. Lett. 22*, 3195–3198, doi:10.1029/95GL03093.

Legutke, S. and E. Maier-Reimer (1999). Climatology of the HOPE-G global ocean general circulation model. *Technical Report No. 21*, German Climate Computer Center (DKRZ), Hamburg, Germany, 90pp.

Legutke, S. and R. Voss (1999). The Hamburg atmosphere-ocean coupled model ECHO-G. *Technical Report No. 18*, German Climate Computer Center (DKRZ), Hamburg, Germany, 62pp.

Lemke, P., M. Harder, and M. Hilmer (2000). The response of Arctic sea ice to global change. *Clim. Change 46*, 277–287, doi:10.1023/A:1005695109752.

Lindsay, R. W. and D. A. Rothrock (1994). Arctic Sea Ice Albedo from AVHRR. *J. Climate 7*, 1737–1749.

Liu, J. P., J. A. Curry, and Y. Y. Hu (2004). Recent Arctic Sea Ice Variability: Connections to the Arctic Oscillation and the ENSO. *Geophys. Res. Lett. 31*, L09211, doi:10.1029/2004GL019858.

Lynch, A. H., A. R. Rivers, and P. J. Bartlein (2003). An assessment of the influence of land cover uncertainties on the simulation of global climate in the early Holocene. *Clim. Dyn. 21*, 243–256, doi:10.1007/s00382–003–0331–7.

Manabe, S. and R. J. Stouffer (1994). Multiple-Century Response of a Coupled Ocean-Atmosphere Model to an Increase of Atmospheric Carbon-Dioxide. *J. Climate 7*, 5–25.

Mann, M. E., R. S. Bradley, and M. K. Hughes (1998). Global-scale temperature patterns and climate forcing over the past six centuries. *Nature 392*, 779–787, doi:10.1038/33859.

Marshall, J. and F. Schott (1999). Open-ocean convection: Observations, theory, and models. *Rev. Geophys. 37*, 1–64, doi:10.1029/98RG02739.

Marsland, S. J., H. Haak, J. H. Jungclaus, M. Latif, and F. Roske (2003). The Max-Planck-Institute global ocean/sea ice model with orthogonal curvilinear coordinates. *Ocean Modelling 5*, 91–127, doi:10.1016/S1463–5003(02)00015–X.

Maslanik, J., S. Drobot, C. Fowler, W. Emery, and R. Barry (2007). On the Arctic climate pardox and the continuing role of atmospheric circulation in affecting sea ice conditions. *Geophys. Res. Lett. 34*, L03711, doi:10.1029/2006GL028269.

Maykut, G. A. and N. Untersteiner (1971). Some results from a time-dependent thermodynamic model of sea ice. *J. Geophys. Res. 76*, 1550–1570.

Min, S. K., S. Legutke, A. Hense, U. Cubasch, W. T. Kwon, J. H. Oh, and U. Schlese (2006). East Asian climate change in the 21st century as simulated by the coupled climate model ECHO-G under IPCC SRES scenarios. *J. Meteorol. Soc. Jpn. 84*, 1–26.

Min, S. K., S. Legutke, A. Hense, and W. T. Kwon (2005). Internal variability in a 1000-yr control simulation with the coupled climate model ECHO-G. - I. Near-surface temperature, precipitation and mean sea level pressure. *Tellus 57A*, 605–621, doi:10.1111/j.1600–0870.2005.00133.x.

Müller, B. (2003). *Eine regionale Klimasimulation für Europa zur Zeit des späten Maunderminimums 1675-1705.* Ph. D. thesis, University of Hamburg.

Mysak, L. A. and S. A. Venegas (1998). Decadal climate oscillations in the Arctic: A new feedback loop for atmosphere-ice-ocean interactions. *Geophys. Res. Lett. 25*, 3607–3610, doi:10.1029/98GL02782.

Overland, J. E., P. Turet, and A. H. Oort (1996). Regional Variations of Moist Static Energy Flux into the Arctic. *J. Climate 9*, 54–65.

Overland, J. E. and M. Wang (2005). The Arctic climate paradox: The recent decrease of the Arctic Oscillation. *Geophys. Res. Lett. 32*, L06701, doi:10.1029/2004GL021752.

Parkinson, C. L. and D. J. Cavalieri (2002). A 21 year record of Arctic sea-ice extents and their regional, seasonal and monthly variability and trends. *Ann. Glac. 34*, 441–446.

Peixoto, J. P. and A. H. Oort (1992). *Physics of Climate*. Springer-Verlag New York.

Perovich, D. K., T. C. Grenfell, B. Light, and P. V. Hobbs (2002). Seasonal evolution of the albedo of multiyear Arctic sea ice. *J. Geophys. Res. 107*(C10), 8044, doi:10.1029/2000JC000438.

Peterson, B. J., R. M. Holmes, J. W. McClelland, C. J. Vorosmarty, R. B. Lammers, A. I. Shiklomanov, I. A. Shiklomanov, and S. Rahmstorf (2002). Increasing river discharge to the Arctic Ocean. *Science 298*, 2171–2173, doi:10.1126/science.1077445.

Qu, X. and A. Hall (2006). Assessing Snow Albedo Feedback in Simulated Climate Change. *J. Climate 19*, 2617–2630, doi:10.1175/JCLI3750.1.

Rahmstorf, S., et al. (2005). Thermohaline circulation hysteresis: A model intercomparison. *Geophys. Res. Lett. 32*, L23605, doi:10.1029/2005GL023655.

Rennermalm, A. K., E. F. Wood, S. J. Dery, A. J. Weaver, and M. Eby (2006). Sensitivity of the thermohaline circulation to Arctic Ocean runoff. *Geophys. Res. Lett. 33*, L12703, doi:10.1029/2006GL026124.

Rigor, I. G., J. M. Wallace, and R. L. Colony (2002). Response of Sea Ice to the Arctic Oscillation. *J. Climate 15*, 2648–2663.

Rind, D., M. Chandler, J. Lerner, D. G. Martinson, and X. Yuan (2001). Climate response to basin-specific changes in latitudinal temperature gradients and implications for sea ice variability. *J. Geophys. Res. 106*(D17), 20161–20173.

Roeckner, E., K. Arpe, L. Bengstson, M. Christoph, K. Claussen, L. Dümelil, M. Esch M., Giorgetta, U. Schlese, and U. Schulzweida (1996). The atmospheric general circulation model ECHAM4: Model description and simulation of present-day climate. *Rep. 218*, Max–Planck–Institut für Meteorologie, Hamburg, Germany.

Roeckner, E., L. Bengtsson, J. Feichter, J. Lelieveld, and H. Rodhe (1999). Transient Climate Change Simulations with a Coupled Atmosphere-Ocean GCM including the Tropospheric Sulfur Cycle. *J. Climate 12*, 3004–3032.

Roesch, A., M. Wild, R. Pinker, and A. Ohmura (2002). Comparison of spectral surface albedos and their impact on the general circulation model simulated surface climate. *J. Geophys. Res. 107*(D14), doi:10.1029/2001JD000809.

Roesch, C. A. (2000). Assessment of land surface schemes in climate models with focus on surface albedo and snow cover. *Zürcher Klimaschriften 78*, ETH Geographisches Institut, Zürich.

Rossow, W., L. C. Garder, P. J. Lu, and A. W. Walker (1991). International Satellite Cloud Climatology Project (ISCCP). Documentation of cloud data. Technical report, WMO/TD-No. 266, World Meteorological Organization, 76 pp. plus appendices.

Rossow, W. B. and R. A. Schiffer (1991). ISCCP cloud data products. *Bull. Amer. Meteor. Soc 72*, 2–20.

Rossow, W. B. and R. A. Schiffer (1999). Advances in understanding clouds from ISCCP. *Bull. Amer. Meteor. Soc 80*, 2261–2287.

Rothrock, D. A., Y. Yu, and G. A. Maykut (1999). Thinning of the Arctic sea-ice cover. *Geophys. Res. Lett. 26*, 3469–3472, doi:10.1029/1999GL010863.

Saenko, O. A., M. Eby, and A. J. Weaver (2004). The effect of sea-ice extent in the North Atlantic on the stability of the thermohaline circulation in global warming experiments. *Clim. Dyn. 22*, 689–699, doi:10.1007/s00382–004–0414–0.

Sausen, R., S. Schubert, and L. Dümelil (1994). A model of river runoff for use in coupled atmosphere ocean models. *J. Hydrology 155*, 337–352.

Serreze, M. C., J. E. Walsh, F. S. Chapin, T. Osterkamp, M. Dyurgerov, V. Romanovsky, W. C. Oechel, J. Morison, T. Zhang, and R. G. Barry (2000). Observational evidence of recent change in the northern high-latitude environment. *Clim. Change 46*, 159–207, doi:10.1023/A:1005504031923.

Shindell, D. T., R. L. Miller, G. A. Schmidt, and L. Pandolfo (1999). Simulation of recent northern winter climate trends by greenhouse-gas forcing. *Nature 399*, 452–455.

Shindell, D. T., G. A. Schmidt, M. E. Mann, D. Rind, and A. Waple (2001). Solar forcing of regional climate change during the Maunder Minimum. *Science 294*, 2149–2152, doi:10.1126/science.1064363.

Stendel, M. and E. Roeckner (1998). Impacts of horizontal resolution on simulated climate statistics in ECHAM4. *Technical Report 253*, Max–Planck–Institut für Meteorologie, Hamburg.

Stephenson, D. B., V. Pavan, M. Collins, M. M. Junge, and R. Quadrelli (2006). North Atlantic Oscillation response to transient greenhouse gas forcing and the impact on European winter climate: A CMIP2 multi-model assessment. *Clim. Dyn. 27*, 401–420, doi:10.1007/s00382–006–0140–x.

Stroeve, J. C., M. C. Serreze, F. Fetterer, T. Arbetter, W. Meier, J. Maslanik, and K. Knowles (2005). Tracking the Arctic's shrinking ice cover: Another extreme September minimum in 2004. *Geophys. Res. Lett. 32*, L04501, doi:10.1029/2004GL021810.

Terray, L., S. Valcke, and A. Piacentini (1998). The OASIS coupler software, version 2.2. *Tech. Rep. TR/CMGC/98-05*, CERFACS.

Thompson, D. W. J. and J. M. Wallace (1998). The Arctic Oscillation signature in the wintertime geopotential height and temperature fields. *Geophys. Res. Lett. 25*, 1297–1300, doi:10.1029/98GL00950.

Tschudi, M., J. A. Curry, and J. M. Maslanik (2001). Airborne observations of summertime surface features and their effect on surface albedo during FIRE/SHEBA. *J. Geophys. Res. 106*(D14), 15335–115344.

Tuenter, E., S. L. Weber, F. J. Hilgen, and L. J. Lourens (2005). Sea-ice feedbacks on the climatic response to precession and obliquity forcing. *Geophys. Res. Lett. 32*, L24704, doi:10.1029/2005GL024122.

UNEP/GRID-Arendal (2006). Arctic, topography and bathymetry. *UNEP/GRID-Arendal Maps and Graphics Library http://maps.grida.no/go/graphic/arctic_topography_and_bathymetry3*, (Accessed 18 December 2006).

Uppala, S.M., et al. (2005). The ERA-40 re-analysis. *Quart. J. Roy. Meteor. Soc. 131*, 2961–3012, doi:10.1256/qj.04.176.

U.S. Climate Change Science Program (2006). Temperature Trends in the Lower Atmosphere: Steps for Understanding and Reconciling Differences. [Karl, T.R., S.J. Hassol, C.D. Miller, and W.L. Murray (eds.)]. *A Report by the Climate Change Science Program and the Subcommittee on Global Change Research*, U.S. Climate Change Science Program, Washington D.C., USA, 180pp.

Uttal, T., et al. (2002). Surface Heat Budget of the Arctic Ocean. *Bull. Amer. Meteor. Soc. 83*, 255–275.

Vavrus, S. and S. P. Harrison (2003). The impact of sea-ice dynamics on the Arctic climate system. *Clim. Dyn. 20*, 741–757, doi:10.1007/s00382–003–0309–5.

Vellinga, M. and R. A. Wood (2002). Global climatic impacts of a collapse of the Atlantic thermohaline circulation. *Clim. Change 54*, 251–267, doi:10.1023/A:1016168827653.

Venegas, S. A. and L. A. Mysak (2000). Is There a Dominant Timescale of Natural Climate Variability in the Arctic? *J. Climate 13*, 3412–3434.

Vinje, T. (2001a). Anomalies and Trends of Sea-Ice Extent and Atmospheric Circulation in the Nordic Seas during the Period 1864-1998. *J. Climate 14*, 255–267.

Vinje, T. (2001b). Fram Strait Ice Fluxes and Atmospheric Circulation: 1950-2000. *J. Climate 14*, 3508–3517.

Vinnikov, K. Y. and A. Robock (1998). The role of natural variability in observed global and regional trend. *Preprints, Ninth Symposium on Global Change, Phoenix, Arizona*, American Meteorological Society, Boston, MA, pp. 211–214.

Vinnikov, K. Y., A. Robock, D. J. Cavalieri, and C. L. Parkinson (2002). Analysis of seasonal cycles in climatic trends with application to satellite observations of sea ice extent. *Geophys. Res. Lett. 29*, 1310, doi:10.1029/2001GL014481.

Viterbo, P. and A. K. Betts (1999). Impact on ECMWF forecasts of changes to the albedo of the boreal forests in the presence of snow. *J. Geophys. Res. 104*(D22), 27803–27810, doi:10.1029/1998JD200076.

von Storch, H. and C. Frankignoul (1998). Empirical modal decomposition in coastal oceanography. In K. H. Brink and A. R. Robinson (Eds.), *The Global Coastal Ocean. Processes and Methods. The Sea Vol. 10*. John Wiley & Sons Inc, New York. 419-455.

von Storch, H. and F. W. Zwiers (1988). Recurrence Analysis of Climate Sensitivity Experiments. *J. Climate 1*, 157–171.

von Storch, H. and F. W. Zwiers (1999). *Statistical Analysis in Climate Research*, Cambridge University Press, 484 pp.

Wagner, S. and E. Zorita (2005). The influence of volcanic, solar and CO2 forcing on the temperatures in the Dalton Minimum (1790-1830): a model study. *Clim. Dyn. 25*, 205–218, doi:10.1007/s00382–005–0029–0.

Wanner, H., S. Bronnimann, C. Casty, D. Gyalistras, J. Luterbacher, C. Schmutz, D. B. Stephenson, and E. Xoplaki (2001). North Atlantic Oscillation: Concepts and studies. *Surv. Geophys. 22*, 321–382, doi:10.1023/A:1014217317898.

Warren, S. G. (1984). Optical constants of ice from the ultraviolet to the microwave. *Appl. Opt. 23*, 1206–1225.

Willmott, C. J. and M. A. Rawlins (1999). Arctic land-surface air temperature: Gridded monthly and annual climatologies (version 1.01), Cent. for Clim. Res., dep. of Geogr., Univ. of Del., Newark.

Winton, M. (2006). Amplified Arctic climate change: What does surface albedo feedback have to do with it? *Geophys. Res. Lett. 33*, L03701, doi: 10.1029/2005GL025244.

Wolff, J., E. Maier-Reimer, and S. Legutke (1997). The Hamburg primitive equation model HOPE. *Technical Report 18*, German Climate Computer Center (DKRZ), Hamburg, Germany.

Wu, P. L., R. Wood, and P. Stott (2005). Human influence on increasing Arctic river discharges. *Geophys. Res. Lett. 32*, L02703, doi:10:1029/2004GL021570.

Xiong, X., K. Stamnes, and D. Lubin (2002). Surface albedo over the Arctic Ocean derived from AVHRR and its validation with SHEBA data. *J. Appl. Met. 41*, 413–425.

Yin, J. H. (2005). A consistent poleward shift of the storm tracks in simulations of 21st century climate. *Geophys. Res. Lett. 32*, L18701, doi:10.1029/2005GL023684.

Zorita, E. and F. González-Rouco (2000). Disagreement between predictions of the future behavior of the Arctic Oscillation as simulated in two different climate models: Implications for global warming. *Geophys. Res. Lett. 27*, 1755–1758.

Zorita, E., H. von Storch, F. J. González-Rouco, U. Cubasch, J. Luterbacher, S. Legutke, I. Fischer-Bruns, and U. Schlese (2004). Climate evolution in the last five centuries simulated by an atmosphere-ocean model: Global temperatures, the North Atlantic Oscillation and the Late Maunder Minimum. *Met. Zeitschr. 13*, 271–289, doi:10.1127/0941–2948/2004/0013–0271.

Acknowledgments

First of all I would like to thank Prof. Dr. Hans von Storch. He gave me the opportunity to write this thesis on a very interesting subject at the GKSS Research Centre in Geesthacht. His supervision include fruitful discussions which helped me greatly in improving my scientific thinking in the process of this thesis.

I also would like to express my gratitude to Prof. Dr. Klaus Dethloff. His ideas and suggestions became part of the essential core of this thesis. I thank him and Prof. Dr. Hans von Storch for their appraisal of the thesis.

Dr. Burkhardt Rockel was the tutor with whom I worked the closest. I am grateful for his support and advice, and the pleasant working atmosphere with all the valuable discussions in his working group.

Special thanks go to Dr. Sebastian Wagner and Dr. Eduardo Zorita, who always had an open door for a discussion and who helped me with any technical or scientific request I had.

I thank Dr. J. Fidel González-Rouco and Dr. Frank Kaspar for their assistance in solving problems concerning the running of the ECHO-G model. I also thank Dr. Elena Sokolova, Dr. Martin Stendel, and Dr. Morten O. Køltzow and all the other participants of the GLIMPSE group for their close cooperation during the project work.

The DKRZ, NSIDC, ISCCP, and ECMWF are appreciated for providing the computing facility, satellite sea ice and cloud data and re-analysis data, respectively. The work on this thesis was partly funded by the EU project GLIMPSE.

Finally I would like to thank Claudia and my family for the moral support which includes special thanks for my sister-in-law Frances. As a native speaker she helped me improve the English on the manuscript.